NOVEL SOLUTIONS TO CLASSICAL SIGNAL PROCESSING PROBLEMS IN OPTIMIZATION FRAMEWORK

A DISSERTATION SUBMITTED TO
THE DEPARTMENT OF ELECTRICAL AND ELECTRONICS
ENGINEERING
AND THE GRADUATE SCHOOL OF ENGINEERING AND SCIENCE
OF BILKENT UNIVERSITY
IN PARTIAL FULFILLMENT OF THE REQUIREMENTS
FOR THE DEGREE OF
DOCTOR OF PHILOSOPHY

By
Yaşar Kemal Alp
June, 2014

I certify that I have read this thesis and that in my opinion it is fully adequate, in scope and in quality, as a dissertation for the degree of Doctor of Philosophy.

Prof. Dr. Orhan Arıkan(Advisor)

I certify that I have read this thesis and that in my opinion it is fully adequate, in scope and in quality, as a dissertation for the degree of Doctor of Philosophy.

Prof. Dr. Mustafa Ç. Pınar

I certify that I have read this thesis and that in my opinion it is fully adequate, in scope and in quality, as a dissertation for the degree of Doctor of Philosophy.

Prof. Dr. A. Enis Çetin

I certify that I have read this thesis and that in my opinion it is fully adequate, in scope and in quality, as a dissertation for the degree of Doctor of Philosophy.

Assoc. Prof. Dr. Sinan Gezici

I certify that I have read this thesis and that in my opinion it is fully adequate, in scope and in quality, as a dissertation for the degree of Doctor of Philosophy.

Assoc. Prof. Dr. Ali Cafer Gürbüz

Approved for the Graduate School of Engineering and Science:

Prof. Dr. Levent Onural
Director of the Graduate School

ABSTRACT

NOVEL SOLUTIONS TO CLASSICAL SIGNAL PROCESSING PROBLEMS IN OPTIMIZATION FRAMEWORK

Yaşar Kemal Alp
Ph.D. in Electrical and Electronics Engineering
Supervisor: Prof. Dr. Orhan Arıkan
June, 2014

Novel approaches for three classical signal processing problems in optimization framework are proposed to provide further flexibility and performance improvement. In the first part, a new technique, which uses Hermite-Gaussian (HG) functions, is developed for analysis of signals, whose components have non-overlapping compact time-frequency supports. Once the support of each signal component is properly transformed, HG functions provide optimal representations. Conducted experiments show that proposed method provides reliable identification and extraction of signal components even under severe noise cases. In the second part, three different approaches are proposed for designing a set of orthogonal pulse shapes for ultra-wideband communication systems with wideband antennas. Each pulse shape is modelled as a linear combination of time shifted and scaled HG functions. By solving the constructed optimization problems, high energy pulse shapes, which maintain orthogonality at the receiver with desired time-frequency characteristics are obtained. Moreover, by showing that, derivatives of HG functions can be represented as a linear combination of HGs, a simple optimal correlating receiver structure is proposed. In the third part, two different methods for phase-only control of array antennas based on semidefinite modelling are proposed. First, antenna pattern design problem is formulated as a non-convex quadratically constraint quadratic problem (QCQP). Then, by relaxing the QCQP formulation, a convex semidefinite problem (SDP) is obtained. For moderate size arrays, a novel iterative rank refinement algorithm is proposed to achieve a rank-1 solution for the obtained SDP, which is the solution to the original QCQP formulation. For large arrays an alternating direction method of multipliers (ADMM) based solution is developed. Conducted experiments show that both methods provide effective phase settings, which generate beam patterns under highly flexible constraints.

Keywords: Hermite-Gaussian function, time-frequency support, time-frequency analysis, ultra-wideband communications, optimization problem, correlating receiver, phased array antennas, semidefinite problem, quadratically constrained quadratic problem, convex relaxation, rank, alternating direction method of multipliers, beam pattern.

ÖZET

BİLİNEN SİNYAL İŞLEME PROBLEMLERİNE ENİYİLEME ÇERÇEVESİNDE YENİ ÇÖZÜMLER

Yaşar Kemal Alp
Elektrik-Elektronik Mühendisliği, Doktora
Tez Yöneticisi: Prof. Dr. Orhan Arıkan
Haziran, 2014

Bilinen üç sinyal işleme problemine, daha esnek ve daha başarılı çözümler elde etmek için eniyileme çerçevesinde yeni çözüm yöntemleri önerilmiştir. İlk kısımda, zaman-frekans destek bölgeleri örtüşmeyen bileşenlerden oluşan sinyallerin analizi için Hermit-Gauss (HG) fonksiyonlarını kullanan yeni bir yöntem geliştirilmiştir. HG fonksiyonları, uygun zaman-frekans dönüşümleri uygulanan sinyal bileşenlerini eniyi şekilde temsil edebilmektedir. Yapılan deneylerde, önerilen yöntemin çok yüksek gürültü seviyelerinde dahi sinyal bileşenlerinin tespitinin ve kestiriminin yüksek başarım ile yapabildiği gözlemlenmiştir. İkinci kısımda, geniş bantlı antenlere sahip çok geniş bantlı iletişim sistemleri için birbirine dik elemanlardan oluşan darbe kümesi tasarımı için üç farklı yaklaşım önerilmiştir. Herbir darbe zamanda kaydırılmış ve ölçeklendirilmiş HG fonksiyonlarının doğrusal kombinasyonu olarak modellenmiştir. Oluşturulan eniyileme problemlerini çözerek almaç tarafında diklik koşulunu sağlayan ve istenilen zaman-frekans niteliklerine sahip yüksek enerjili darbe şekilleri elde edilmiştir. Ayrıca, HG fonksyionlarının türevlerinin yine HG fonksiyonlarının doğrusal kombinasyonu olarak ifade edilebildiği gösterilerek, çok basit yapıda olan optimum bağdaştırmalı almaç yapısı önerilmiştir. Üçüncü kısımda ise faz dizili antenlerin optimum kontrolü için yarıkesin modelleme tabanlı iki farklı yöntem önerilmiştir. İlk olarak, anten örüntüsü tasarlama problemi dışbükey olmayan karesel kısıtlamalı karesel problem (KKKP) olarak modellenmiştir. Daha sonra, oluşturulan KKKP gevşetilerek dışbükey olan yarıkesin problem (YKP) elde edilmiştir. Orta büyüklükteki dizi antenler için, elde edilen YKP'ye kerte-1 olan bir çözüm bulmak için döngüsel kerte arıtım yöntemi geliştirilmiştir. Daha büyük dizi antenler içinse yön değiştirmeli çarpanlar tabanlı yeni bir yöntem önerilmiştir. Yapılan deneylerde, önerilen her iki yöntem ile istenilen özelliklere sahip hüzme örüntülerini oluşturan faz değerlerinin kestirilebildiği gözlemlenmiştir.

Anahtar sözcükler: Hermit-Gauss fonksiyonları, zaman-frekans destek bölgesi, zaman-frekans analizi, çok geniş bantlı iletişim, eniyileme problemi, bağdaştırmalı almaç, faz dizili anten, yarıkesin problem, karesel kısıtlamalı karesel problem, kerte, dışbükey gevşetme, yön değiştirmeli çarpanlar yöntemi, hüzme örüntüsü.

Acknowledgement

I am grateful to my advisor Prof. Orhan Arıkan for his guidance and support during the whole period of this work. He was not only a teacher but also a father to me. His intuition for solving problems was amazing and it was an honour for me to be his Ph.D. student. I have learned huge amount of technical knowledge from him. However, my greatest attainment from Prof. Arıkan is realizing that research is not something that is required to full fill your Ph.D., but a process, that you enjoy to do throughout your whole life.

I am heartily thankful to the other four members of my dissertation committee Dr. Mustafa Pınar, Dr. Sinan Gezici, Dr. Enis Çetin and Dr. Ali Cafer Gürbüz for their careful reading of the dissertation draft and numerous helpful suggestions.I wish to thank to Dr. Mustafa Pınar once more, since the Convex Analysis lecture that I took from him introduced the convex modelling concept to me.

I would like to thank to all my former colleagues Hamza Soğancı, Mehmet Emin Tutay and Osman Gürlevik. I would in particular thank to Dr. Burak Güldoğan for his valuable advises during the whole period of this thesis.

I would also like to thank all my current colleagues in Radar Electronic Support and Electronic Attack Systems Engineering Department in ASELSAN Inc. I would in particular like to express my gratitude to Gökhan Gök, Sedat Çamlıca and Dr. Fatih Altıparmak for numerous technical and non-technical discussions.

Finally, I would like to express my gratitude to my parents, Şerife Alp and Bayram Alp, for always believing in me and encouraging me to achieve my goals. My deepest gratitude goes to my wife, Meryem, for her support, patience and sincere love, which have been invaluable in helping me to focus on my academic pursuits.

Contents

List of Figures

List of Tables

Dedicated to my wonderful wife Meryem, who knew I should and always said I could...

Chapter 1

Introduction

Many signal processing problems can be cast as an optimization problem of the form

$$\begin{aligned} &\min_{\mathbf{x}} \ f_0(\mathbf{x}) \\ &\text{s.t. } f_k(\mathbf{x}) \leq b_k \ k = 1, .., K, \end{aligned} \tag{1.1}$$

where $\mathbf{x} \in \mathbb{R}^n$ is the vector of variables, $f_0 : \mathbb{R}^n \rightarrow \mathbb{R}$ is the objective function and $f_k : \mathbb{R}^n \rightarrow \mathbb{R}, \ k = 1, .., K$, are the constraint functions. Typically, constructed problems are non-convex and extremely difficult to solve. For such cases, there are algorithms, which provide locally optimum solutions. When the objective function and constraints are convex with appropriate forms, the optimization problem can be solved to obtain its global optimizer efficiently by deploying available convex solvers. With the development of the high precision, fast convex solvers, modelling the physical problem in a convex optimization framework has become an active research area. In this thesis, optimization based novel approaches are utilized for solving signal processing problems from different areas.

In the first part of the thesis, decomposition of a signal into its components, which have compact time-frequency supports (TFS), is discussed. In radar, sonar, seismic, acoustic, speech and biomedical signal processing applications, the acquired data contains single or multiple components with compact TFSs [1, 2, 3, 4, 5, 6]. Estimation of each component from the noisy measurement is an important application of time-frequency analysis [7]. Although there are wavelet and chirplet based techniques for decomposition of signals into its components having generalized time-bandwidth products of around 1, they are not well suited for analysis of signals, whose components have larger TFSs. For analysis of such signals, we are proposing a new technique based on adaptive Hermite-Gaussian (HG) expansion [8, 9, 10].

The proposed technique makes use of adaptive HG basis expansion to estimate individual signal components. HG functions share many desired properties. They form an orthonormal basis for the space of finite energy signals, which are piecewise smooth in every finite interval [11]. They also provide the highest energy concentration inside the circular TFS around the origin in the time-frequency plane. Hence, HG basis provides the optimal representation for the signal components, which have circular TFSs around the origin. However, this representation is no longer optimal for signals having non-circular TFSs positioned away from the origin. For such signal components, we propose an adaptive pre-processing stage, where TFS of the signal component is transformed to a circular one centred around the origin so that it can be efficiently represented by HGs. The expansion order is estimated by a noise penalized cost function. Then, the desired signal component estimate is obtained by back transforming the identified signal component. For signals with multiple components that do not have overlapping TFSs, an EM based iterative procedure is proposed for joint analysis and expansion of individual signal components in HG basis.

In the second part of the thesis, design of orthogonal pulse shapes for ultra-wideband (UWB) communications is investigated. Ultra-wideband (UWB) technology has attracted great attention for designing systems for short range, high data rate communications [12, 13, 14, 15]. Since these systems use extremely short pulse durations, they occupy a very broad spectrum and interfere with existing systems in the same area. To impose restrictions on the spectrum of these systems, U.S. Federal Commission of Communications (FCC) has released the spectral mask [16]. Although the spectral mask constraints the transmission power of the UWB system, to maximize the received power at the receiver side, high energy pulse shapes, which fully utilize the spectral mask, should be used.

Also by using multiple pulse shapes, which are orthogonal to each other, channel utilization can be improved.

Many methods have been reported for designing multiple orthogonal waveforms for UWB communications [17, 18, 19, 20, 21]. These methods use the designed pulse shapes as correlators at the receiver. However, high-efficiency antennas are typically resistive-capacitive devices which often behave as differentiators [22, 23]. Hence the received signals are not orthogonal. In [24], a pulse shape design method, which preserves the orthogonality of the pulse shapes at the receiver in case of differentiating antennas, is proposed. However, in this method no spectral mask constraints are utilized. In [25], a simplified suboptimal structure for non-matched correlation detection is proposed, where the received pulses are correlated with the locally generated signals, which are different than the received pulse shapes. Although the generated pulses are adapted the spectral mask, the receiver structure is not optimal.

To design high energy pulse shapes, which preserve orthogonality at the receiver, while satisfying the spectral mask constraints during the propagation, we propose three different approaches within the optimization framework [26, 27]. We model each pulse shape as a linear combination of time-shifted and scaled HG functions. The transmitting and receiving antennas are modelled as differentiators with a certain gain. Although three different optimization problems are constructed, all of them use the following design criteria: 1) Energy of the received pulse shapes in their effective passband should be maximized to improve the detection performance at the receiver side; 2) Designed pulse shapes should satisfy the spectral mask constraints during the propagation; 3) Duration of the pulse shapes should be smaller than the given pulse duration at the transmitter; 4) All the pulse shapes should be orthogonal at the receiver. By showing that any HG function can be represented as a superposition of the HGs, an optimal correlating receiver structure with a simple form is proposed.

In the final part of the thesis, phase-only control of array antennas is discussed. Array antennas are used in many applications such as radar [28], sonar [29], communications [30], radio astronomy [31], seismology and tomography [32]. By controlling the amplitude level and phase of the signal at each element, the beam pattern of the array can be steered to different directions, sidelobe levels can be suppressed, mainlobe beam width can be reduced [33]. However, due to cost constraints and hardware limitations, many systems do not have an individual amplitude controller for each element. Hence, optimal control of array beam pattern by varying only the element phases is desired.

Phase-only control of antenna arrays is a widely investigated area in array signal processing. Adaptive sidelobe nulling based on the autocorrelation function of the received signal is proposed in [34, 35]. However, proposed method can not be used for the transmit antenna case. A phase perturbation based method, where the non-linear phase-only nulling problem is linearised by assuming that the phase perturbations are small, is proposed in [36]. Since the phase perturbations are assumed to be small, there would be severe problems in hardware implementations. In [37, 38, 39], particle swarm optimization and genetic algorithm are used to minimize a certain cost function of element phases. However, since the cost function is non-convex, the optimality of the provided solution is not guaranteed.

For phase-only control of array pattern, we define two specific problems: 1) Phase-only beam synthesis for moderate size arrays; 2) Phase-only sidelobe suppression for large arrays. In the first problem, element phases, which satisfy the given constraints limiting the sidelobe and mainlobe power, are to be estimated. In the second problem, element phases, which minimize the total radiation power at given radiation directions while satisfying the desired mainlobe power level, are to be estimated. Unlike the previously proposed approaches in the literature, a convex programming based method is proposed for both of the problems. First a non-convex, quadratically constrained quadratic problem (QCQP) is constructed to model the physical problem. Then, by relaxing the constructed QCQP, a convex semidefinite problem (SDP) is obtained, for which the global optimum solution can be obtained efficiently. Although the resulting SDP is convex, its optimal solution is almost never a rank-1 matrix. For the first problem, to achieve a rank-1 solution, we propose a novel iterative rank refinement algorithm, where in each step an SDP with additional convex constraints are solved [40]. We show that, after a few iterations, the optimal solution of the constructed SDP has very fast decaying singular values, converging to a rank-1 solution. This algorithm is also used for the FIR filter design problem in [41, 42]. Although the proposed method can be utilized for solving the later problem for moderate size arrays, it is not appropriate for large arrays. Hence, we propose an alternating direction method of multipliers (ADMM) based solution for this problem [43, 44]. By utilizing ADMM, the constructed SDP is divided into smaller subproblems whose solutions are either analytically known or easy to compute. It is demonstrated on practically significant applications that, by using the proposed ADMM based method, phase values for generating desired beam characteristics for large arrays having more than 500 elements can be obtained.

Chapter 2

Support Adaptive Hermite-Gaussian Expansions: A New Tool For Time-Frequency Analysis of Compact Support Signals

2.1 Introduction

Hermite-Gaussian (HG) functions constitute a natural basis for signals with compact time-frequency supports (TFSs). They have found applications in various fields of signal processing. In image processing, Hermite Transform has been proposed for capturing local information [45]. Another image processing application is given in [46] for rotation of images. Also, in [47], HG functions are used for reconstruction of video frames. In telecommunications, highly localized pulse shapes both in time and frequency domains can be generated by using linear combinations of the HG functions [48]. As part of biomedical applications, representation of EEG and ECG signals in terms of HGs also have been proposed [49, 50].

In [51], HG functions are used for characterization of the origins of vibrations in swallowing accelerometry signals. An electromagnetics application is reported in [52], where the time domain response of a three dimensional conducting object excited by a compact TFS function is modeled by using HG expansions to obtain a an efficient extrapolator based on this expansion. Another electromagnectics application reported in [53], where a new method for evaluating distortion in multiple waveform sets in UWB communications has been proposed. Finally, as signal processing applications, HG functions are used for designing high resolution, multi-window time-frequency representation, where different order HGs are employed to realize multiple windows, and non-stationary spectrum estimation [54, 55, 56, 57].

Single or multi-component signals with compact TFSs are frequently encountered in radar, sonar, seismic, acoustic, speech and biomedical signal processing applications [1, 2, 3, 4, 5, 6]. Decomposition of such a signal into its components is an important application of time-frequency analysis [7]. For signals whose components have generalized time-bandwidth products of around 1, wavelet and chirplet based signal analysis techniques have been developed [58, 59, 60].

In this work, we are proposing a new signal analysis technique for signals whose components may have larger time-bandwidth products. Such signals are commonly employed in electronic warfare, including radar and sonar applications, because of their high resolution properties. Furthermore, biomedical signals including EEG and ECG have complicated time-frequency structures that significantly benefits from the proposed approach. The proposed signal analysis technique makes use of adaptive HG basis expansion to estimate individual signal components. It is a well known fact that HG functions form an orthonormal basis for the space of finite energy signals which are piecewise smooth in every finite interval [11]. What makes HGs special among other types of basis functions is their optimal localization properties in both time and frequency domains. For any circular TFS around the origin, HGs provide the highest energy concentration inside that region [61, 62, 63]. Therefore, if a signal component has a circular TFS around the origin, its representation by using the HG basis provides the optimal representation for a given representation order. However, if the signal component has a non-circular TFS positioned away from the origin, its HG representation is no longer optimal. Here, we propose an adaptive pre-processing stage where TFS of the signal component is transformed to a circular one centred around the origin so that it can be efficiently represented by HGs. The expansion order is estimated by a noise penalized cost function. Then, the desired representation is obtained by back transforming the identified signal component. For signals with multiple components that do not have overlapping TFSs, an EM based iterative procedure is proposed for joint analysis and expansion of individual signal components in HG basis.

The outline of this chapter is as follows. In Section 2.2, we give a brief review of HG functions and emphasize their fundamental properties. In Section 2.3, the proposed pre-processing stage is introduced. EM based iterative component estimation for analysis of multi-component signals and determination of optimal expansion orders are explained in Section 2.4. Results on synthetic and real signals are provided in Section 2.5. Conclusions are given in Section 2.6.

2.2 Review of Hermite-Gaussian Functions

HG functions form a family of solutions to the following non-linear differential equation:

$$f''(t) + 4\pi^2 \left(\frac{2n+1}{2\pi} - t^2 \right) f(t) = 0. \tag{2.1}$$

The n^{th} order HG function $h_n(t)$ is related to the n^{th} order Hermite polynomial $H_n(t)$ as

$$h_n(t) = \frac{2^{1/4}}{\sqrt{2^n n!}} H_n(\sqrt{2\pi} t) e^{-\pi t^2}, \tag{2.2}$$

where, with the initialization of $H_0(t) = 1$ and $H_1(t) = 2t$, $H_n(t)$ can be recursively obtained as

$$H_{n+1}(t) = 2tH_n(t) - 2nH_{n-1}(t). \tag{2.3}$$

Therefore, HG functions can also be computed recursively. A detailed discussion on HG functions and Hermite polynomials are available in [64] and [65], respectively. HG functions, of which the first four are shown in Fig.2.1, form

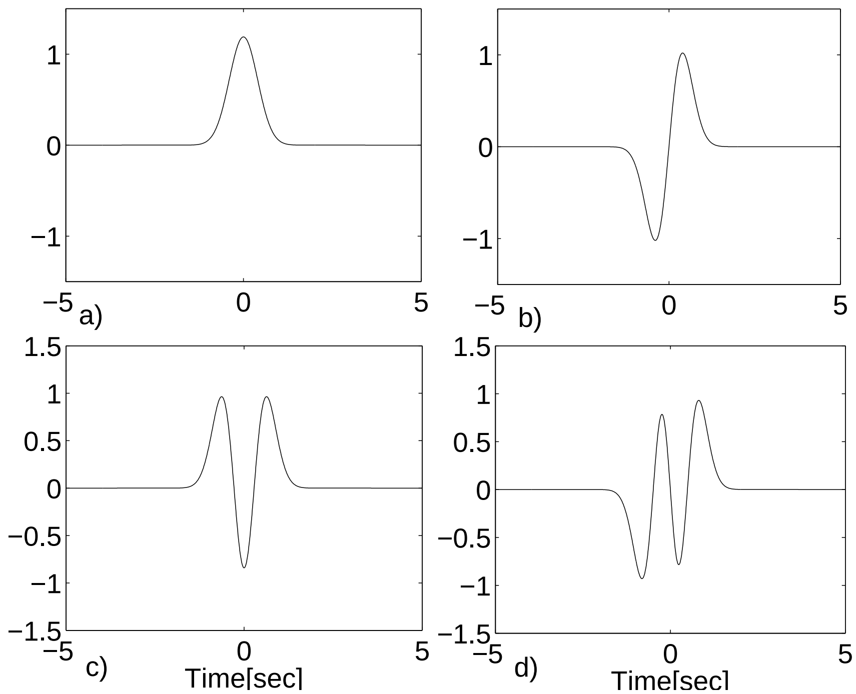

Figure 2.1: The first four HG functions: (a) $h_0(t)$; (b) $h_1(t)$; (c) $h_2(t)$; (d) $h_3(t)$.

an orthonormal basis for the space of finite energy signals which are piecewise smooth in every finite $[-\tau, \tau]$ interval [11]. Hence, if $s(t)$ is in this space, it can be represented as

$$s(t) = \sum_{n=0}^{\infty} \alpha_n h_n(t), \tag{2.4}$$

where the expansion coefficients are[1] :

$$\alpha_n = \int h_n(t) s(t) dt. \tag{2.5}$$

Furthermore, HG functions are eigenvectors of the Fourier transformation [66]:

$$\mathcal{F} h_n(t) = \lambda_n h_n(t), \tag{2.6}$$

where $\mathcal{F}$ is the Fourier transform operator defined as

$$\mathcal{F} s(t) = \int s(t) e^{-j2\pi f t} dt, \tag{2.7}$$

and $\lambda_n = e^{-j\frac{\pi}{2}n}$ is its n^{th} eigenvalue. Similarly, the fractional Fourier transform[2] (FrFT) of order $-2 \leq a < 2$, also admits the HG functions as its eigenfunctions

---

[1] All the integrals in this chapter are computed from $-\infty$ to ∞ unless otherwise is stated.

[2] Definition of fractional Fourier transform is provided in Appendix-A.

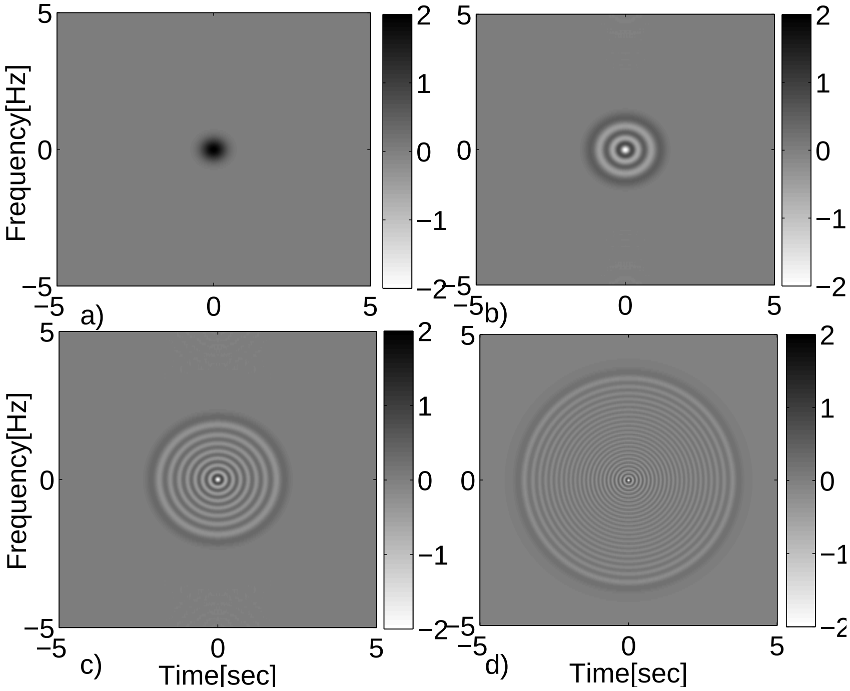

Figure 2.2: Wigner-Ville distribution of (a) $h_0(t)$; (b) $h_5(t)$; (c) $h_{15}(t)$; (d) $h_{45}(t)$.

[67]:

$$\mathcal{F}^a h_n(t) = e^{-j\frac{\pi}{2}an} h_n(t), \tag{2.8}$$

where $\mathcal{F}^a$ is the FrFT operator of order a. Hence, FrFT of $s(t)$ can be obtained as:

$$\mathcal{F}^a s(t) = \sum_{n=0}^{\infty} \alpha_n e^{-j\frac{\pi}{2}an} h_n(t). \tag{2.9}$$

As seen from equation (2.8), the FrFT simply scales HGs. Thus, HG functions have circular support in the time-frequency plane. To demonstrate this fact, in Fig.2.2, Wigner-Ville distribution[3] of $h_0(t), h_5(t), h_{15}(t)$ and $h_{45}(t)$ are shown.

---

[3] Definition of Wigner-Ville distribution is provided in Appendix-A.

2.3 Support Adaptive Hermite-Gaussian Expansion

A piecewise smooth signal $s(t)$ can be approximated by using the following L^{th} order HG expansion:

$$\tilde{s}^{(L)}(t) = \sum_{n=0}^{L} \alpha_n h_n(t), \tag{2.10}$$

with its corresponding normalized approximation error:

$$e^{(L)} = \frac{\int |s(t) - \tilde{s}^{(L)}(t)|^2 dt}{\int |s(t)|^2 dt}, \tag{2.11}$$

where α_n are obtained as in (2.5). Since the basis functions are orthonormal, in the absence of noise, by increasing the expansion order L, the approximation error can be decreased. However, for noisy $s(t)$, to avoid noise fitting the expansion order should not be increased indefinitely. Thus, in the noisy case, a low order representation with a reasonably small approximation error is desired. If $s(t)$ has circular TFS centred at the origin of the time-frequency plane, HG basis provides the optimal representation in the sense that the fewest of number of basis functions are required for its representation [61, 62, 63]. If $s(t)$ has a non-circular TFS away from the origin, high number of HGs would be used and most of them will have their support largely dominated by noise or other signal components that might be present, rather than the signal component. This fact is demonstrated in Figs.2.3 and 2.4. In Fig.2.3, synthetically generated noisy observations of non-circular support (a) and circular support (b) signals are shown together with their spectrograms[4] provided in (c) and (d), respectively. In Fig.2.4, the actual noise-free signal components and their respective HG approximations are shown. Even at this low SNR, the signal with circular TFS is successfully approximated by HG functions. However, in the case of non-circular support, the representation has significant noise artifacts. Since in practice, TFSs of signal components are not necessarily circular nor centred at the origin, HG representation of them do not provide desirable results. To overcome this problem, we propose a pre-processing stage which transforms the TFS of the signal component

---

[4] Definition of spectrogram is provided in Appendix-A.

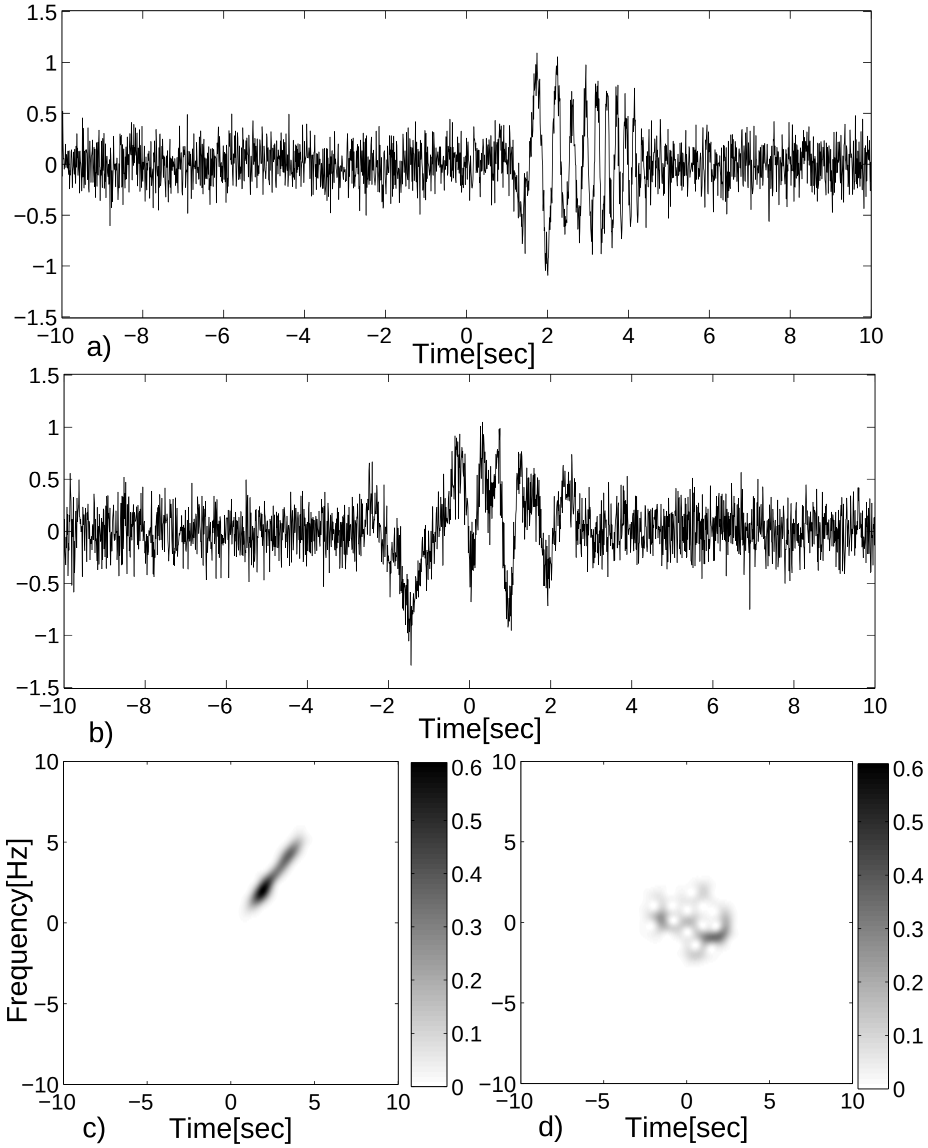

Figure 2.3: Synthetically generated noisy observations of (a) non-circular and (b) circular TFS signals; (c,d) Their respective spectrograms. While computing the spectrograms, a Gaussian window with standard deviation $\sigma = 1/\sqrt{2\pi}$sec was used.

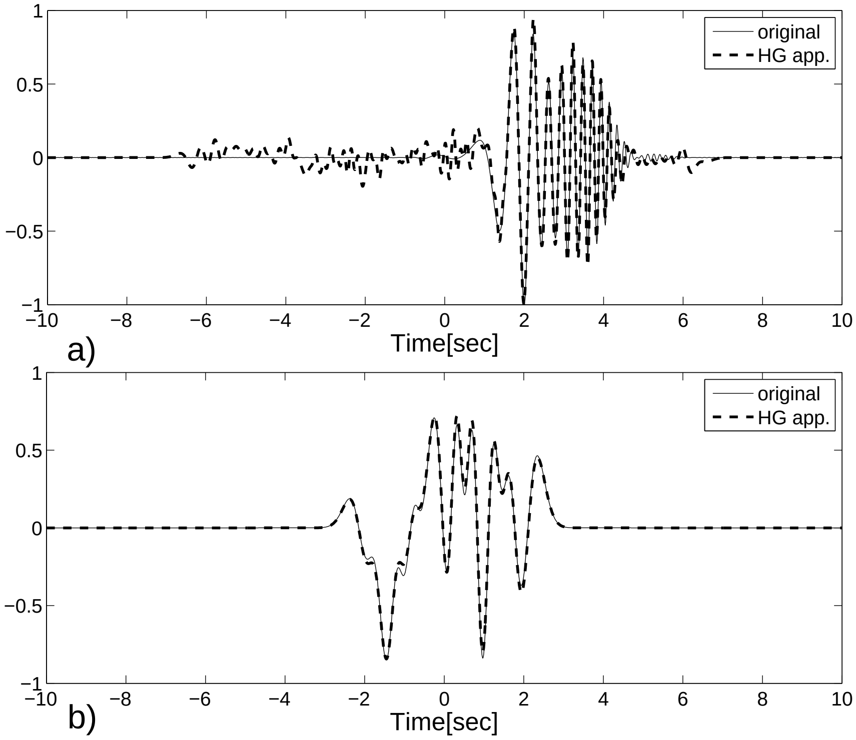

Figure 2.4: The original (solid) and HG expansion based approximation (dashed) of the (a) non-circular support and (b) circular support signal shown in Fig.2.3.

to a circular one centred around the origin. This transformation is achieved by applying sequentially three time-frequency operations: 1) time-frequency translation, 2) instantaneous-frequency shifting and 3) scaling. Then, the transformed signal component is represented by HG basis. Finally, obtained representation is transformed back to the original support of the component by applying the corresponding inverse operations as a post-processing stage. In the proceeding subsections, first, proposed operations operating on a mono-component, noise free signal $s(t)$ will be presented. Then, how to apply these operations on noisy observations of multi-component signals will be detailed.

2.3.1 Time-Frequency Translation Operation

As a first step of support transformation, as in [5], time and frequency centers of a mono-component signal $s(t)$ are obtained by using

$$t_c = \frac{\int t|s(t)|^2 dt}{\int |s(t)|^2 dt}, \tag{2.12}$$

$$f_c = \frac{\int f|S(f)|^2 df}{\int |s(t)|^2 dt}, \tag{2.13}$$

where $S(f)$ is the Fourier transform of $s(t)$. Then, the signal is translated in the time-frequency plane so that its time-frequency center is at the origin:

$$s_c(t) = s(t + t_c)e^{-j2\pi f_c t}. \tag{2.14}$$

2.3.2 Instantaneous Frequency Shifting Operation

To represent $s_c(t)$ with fewest number of HG functions, its TFS should fit into a circular region centered at the origin in the time-frequency plane. This means that, the generalized time-bandwidth product (GTBP) of the translated signal $s_c(t)$ should be minimized [58]. GTBP of $s_c(t)$ can be minimized by shifting its instantaneous frequency (IF) to the dc level for all time instants. IF of $s_c(t)$ can be computed as

$$f_c(t) = \frac{\int f W_{s_c}(t, f) df}{\int W_{s_c} t, f) df}, \tag{2.15}$$

where $W_{s_c}(t, f)$ is the Wigner-Ville distribution of $s_c(t)$ [68]. Note that since $s_c(t)$ is mono-component and noise free, computed $f_c(t)$ is the true instantaneous frequency of $s_c(t)$. Then, IF shifting operation is applied to $s_c(t)$ as:

$$s_\phi(t) = s_c(t)e^{-j2\pi\phi_c(t)}, \tag{2.16}$$

where $\phi_c(t)$ is the instantaneous phase of $s_c(t)$ defined as the cumulative IF function [68]:

$$\phi_c(t) = \int_{-\infty}^{t} f_c(\tau) d\tau. \tag{2.17}$$

2.3.3 Scaling Operation

Once time-frequency translation and IF shifting operations are applied to $s(t)$, it should be scaled by a proper scaling factor so that its effective duration and bandwidth are equalized. Effective duration and bandwidth of $s_\phi(t)$ are defined as [68]:

$$D_\phi = \left[\frac{\int (t - t_\phi)^2 |s_\phi(t)|^2 dt}{\int |s_\phi(t)|^2 dt}\right]^{1/2}, \tag{2.18}$$

$$B_\phi = \left[\frac{\int (f - f_\phi)^2 |S_\phi(f)|^2 df}{\int |s_\phi(t)|^2 dt}\right]^{1/2}, \tag{2.19}$$

where $S_\phi(f)$ is the Fourier transform of $s_\phi(t)$, t_ϕ and f_ϕ are, respectively, time and frequency centers of the $s_\phi(t)$ given by

$$t_\phi = \frac{\int t |s_\phi(t)|^2 dt}{\int |s_\phi(t)|^2 dt}, \tag{2.20}$$

$$f_\phi = \frac{\int f |S_\phi(f)|^2 df}{\int |s_\phi(t)|^2 dt}. \tag{2.21}$$

Effective duration and bandwidth of $s_\phi(t\nu)$ are equalized by choosing the scaling factor ν as:

$$\nu = \sqrt{D_\phi / B_\phi}\ . \tag{2.22}$$

Following this scaling, effective duration and bandwidth of $s_\phi(t\nu)$ are both equal to $\sqrt{D_\phi B_\phi}$. After applying the scaling operation, we get:

$$s_s(t) = s(t\nu + t_c) e^{-j2\pi\phi(t\nu + t_c)}. \tag{2.23}$$

The effect of the proposed time-frequency operations on the TFS of a mono-component signal is demonstrated in Fig.2.5. In (a), TFS of the signal is shown. Here, the radius R effectively determines expansion order for the signal achieving a reasonably small approximation error. After applying (b) time-frequency translation, (c) IF shifting and (d) scaling operations, TFS of the resulting signal fits into a circular region with a smaller area centred around the origin of the time-frequency plane. Since R' is smaller than R, the signal can be represented with significantly less number of basis functions than its original version. Once these transforms are applied to $s(t)$ as the pre-processing stage, resulting signal $s_s(t)$ is approximated by an L^{th} order expansion:

$$\tilde{s}_s(t) = \sum_{n=0}^{L} \alpha_n h_n(t), \tag{2.24}$$

where $\alpha_n = \int h_n(t) s_s(t) dt$. Inverse operations are applied to this approximation to obtain an estimate of the original signal $s(t)$:

$$\tilde{s}(t) = \tilde{s}_s(\frac{t - t_c}{\nu}) e^{j2\pi\phi(t)}. \tag{2.25}$$

In Fig.2.6, block diagram of the proposed support adaptive HG expansion for a mono-component signal $s(t)$ is shown in a compact form. First, pre-processing stage is applied to $s(t)$ to transform its TFS to a circular region centered around the origin. The input $\mathbf{p}$ denotes the parameter vector consisting of the required parameters for the pre-processing stage, i.e., $\mathbf{p} = \{t_c, f(t), v\}$. Another important input parameter of the mono-component signal analysis is the representation order L, which will be discussed in detail in Section 2.4. For a reasonable approximation error, L is chosen according to the area of the effective TFS of $s_s(t)$. Since $s_s(t)$ has compact circular TFS, time-bandwidth product of $s_s(t)$ is a good measure for its TFS [58]. The HG basis expansion in (2.24) essentially performs a representation of $s_s(t)$ by using $L+1$ basis functions where $L+1$, the degrees of freedom in the representation, is approximately same as the time-bandwidth product of $s_s(t)$. Given $\mathbf{p}$ and L, $s_s(t)$ is approximated by $\tilde{s}_s(t)$ as in (2.24). Then, inverse operations are applied to transform back the support of the obtained signal estimate $\tilde{s}_s(t)$ to its original location.

To demonstrate the performance of the proposed time-frequency transforms, a synthetic mono-component, noise free signal whose real part is shown in Fig.2.7(a), was generated. The spectrogram of the signal before and after the pre-processing stage are also provided in (b) and (c), respectively. Note that, the proposed time-frequency operations successfully translate the TFS of the signal to a circular region around the origin. In Fig.2.8, we compare the normalized approximation error defined in (2.11) as a function of approximation order

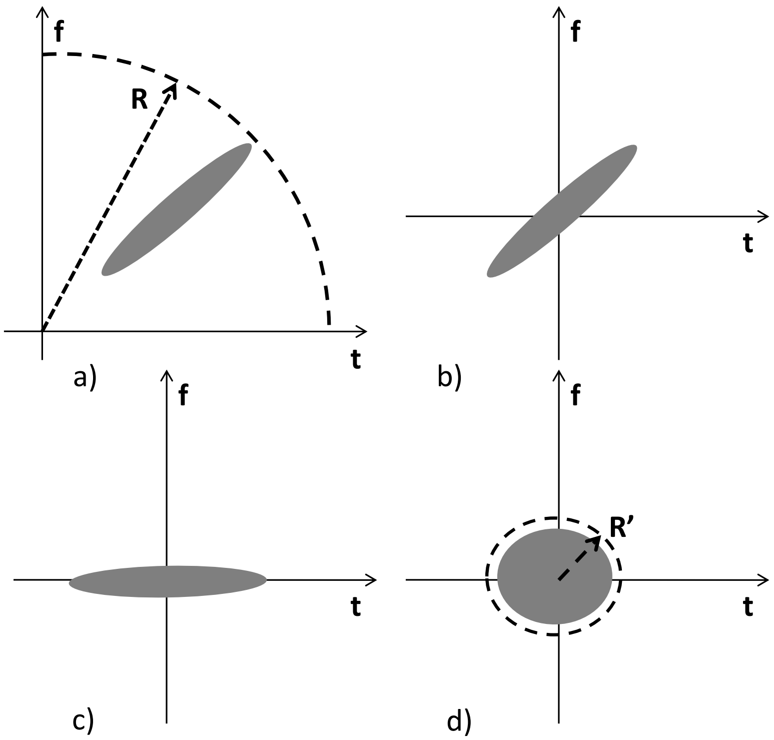

Figure 2.5: Illustration of the proposed pre-processing stage: (a) TFS of the signal; (b) After time-frequency translation; (c) After instantaneous frequency shifting; (d) After scaling. R and R' denote the radius of the smallest circle, which encloses the signal support.

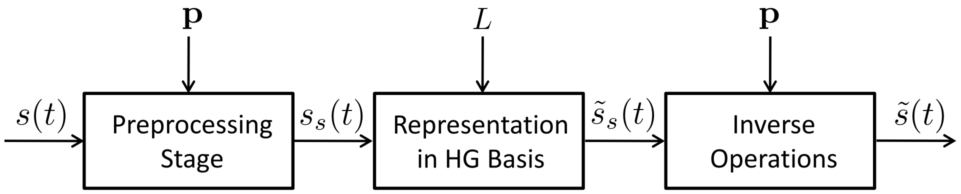

Figure 2.6: Support adaptive HG expansion for mono-component signals.

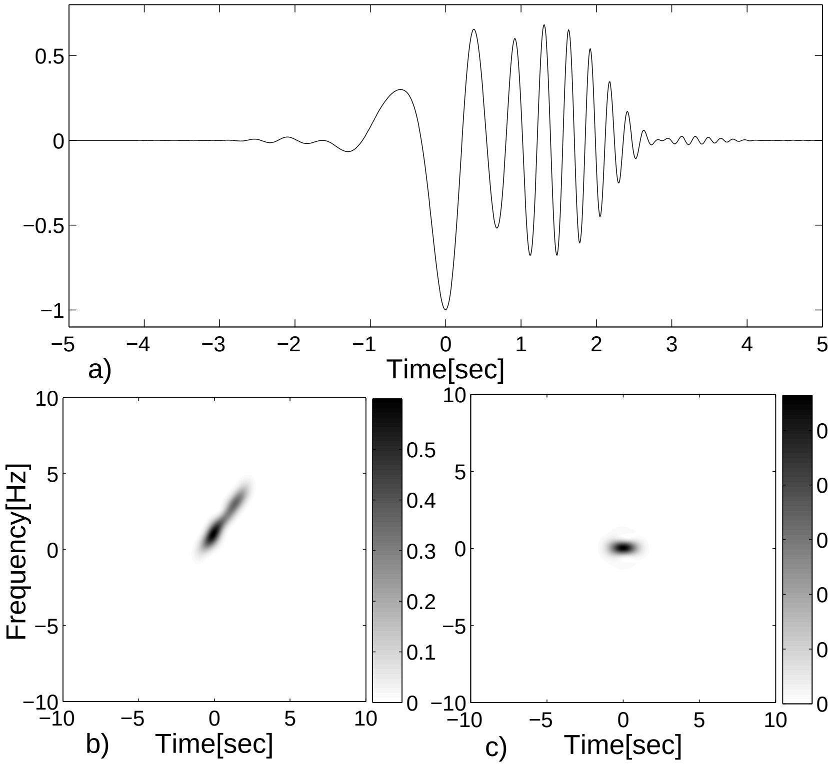

Figure 2.7: (a) Synthetically generated signal. Its spectrogram (b) before and (c) after the pre-processing stage. While computing the spectrogram, a Gaussian window with standard deviation $1/\sqrt{2\pi}$ sec was used.

L, (i) when no operations is applied to the signal (marked with squares), (ii) when only time-frequency translation is applied (marked with stars) and (iii) when all the proposed operations are applied (marked with circles). Note that in Fig.2.8 approximation order 0 corresponds to the HG representation by using a single HG function of order 0. Therefore, depending on the effectiveness of the pre-processing, the resultant error of the representation even with a single HG function makes a difference. As illustrated, proposed pre-processing stage significantly decreases the required number of HG functions to achieve a reasonably small approximation error. In Fig.2.9, the original signal and its order-10 HG approximation after applying the proposed pre-processing stage are shown for a normalized approximation error of -25dB. Note that the same level of approximation error would be achieved by using more than 70 basis functions when no pre-processing is performed and more than 35 basis functions when only time-frequency translation is applied.

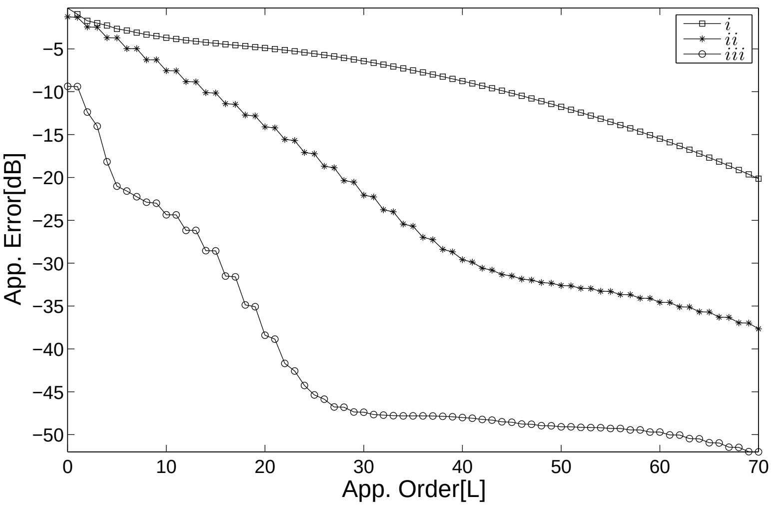

Figure 2.8: Normalized approximation error as a function of approximation order L: (i) When no operation is applied (marked with square); (ii) When only time-frequency translation is applied (marked with star); (iii) When all the proposed operations are applied (marked with circle).

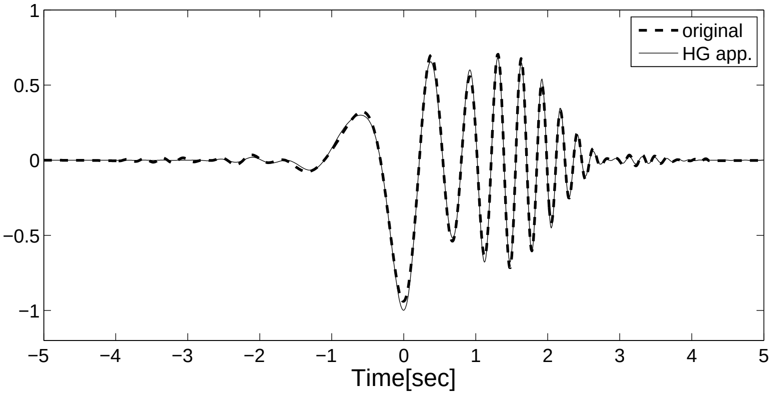

Figure 2.9: Comparison of original signal (solid) and order-10 HG approximation (dashed) after applying the proposed pre-processing stage.

2.4 Iterative Component Estimation for Analysis of Multi-Component Signals

In this section, we discuss the analysis of multi-component signals by using the proposed method. Consider the multi-component signal in noise:

$$x(t) = s_1(t) + s_2(t) + ... + s_K(t) + n(t) \ , \tag{2.26}$$

where $s_k(t), \ k = 1, .., K$ are signal components with non-overlapping compact TFSs and $n(t)$ is the additive observation noise with variance σ^2, which is assumed to have circularly symmetric white Gaussian distribution. For this multi-component signal, the proposed mono-component analysis technique can not be applied directly to obtain reliable estimates of the pre-processing stage parameters $\{t_c, f(t), v\}$. For estimating each component, the parameters belonging to that particular component should be estimated from the available observation $x(t)$, separately. For this purpose, we propose an EM like iterative, fully automated component estimation technique.

The pre-processing stage parameters for the k^{th} signal component $s_k(t)$ can be estimated from its spectrogram. Since the signal components are assumed to have non-overlapping TFSs, the spectrogram of $s_k(t)$ can be estimated by running a segmentation algorithm on the spectrogram of $x(t)$. At the initialization step $i = 0$ of the proposed iterative technique, the spectrogram of the available observation $|X(t, f)|^2$ is computed, where $X(t, f)$ denotes the short time Fourier transform[5] (STFT) of $x(t)$. While computing the spectrogram, a Gaussian window with a valid variance which resolves all the signal components in the resulting time-frequency distribution is used. This variance can be chosen by observing the time and frequency support of $x(t)$. Let T_x and B_x denote the observed time and frequency support of $x(t)$, respectively. The standard deviation of the Gaussian window for time-bandwidth product optimal STFT is given by $\sqrt{T_x}/\sqrt{2\pi B_x}$ [58]. Then, we use a segmentation algorithm to obtain the initial TFSs of individual signal components. For this purpose, Chan-Vese active contours can be utilized

---

[5] Definiton of short time Fourier transform is provided in Appendix-A.

[69]. In this segmentation technique, by minimizing an appropriately chosen energy functional, intensity images are segmented with enclosing contours. Ideally, this energy functional is minimized when the active contours are settled on the boundary of the regions. However, to improve the performance, in [69], authors proposed a variety of user defined stopping criteria for different types of images. In our case, the active contour iterations are terminated when the average intensity along a current contour is larger than a threshold which is chosen as $p_1^i = \lambda^i |X(\bar{t}, \bar{f})|^2 + (1-\lambda^i)\sigma^2/F_s$, where, σ^2 is the noise variance, F_s is the sampling frequency, $|X(\bar{t}, \bar{f})|^2$ is the maximum value of $|X(t,f)|^2$ and $0 < \lambda^i < 1$ is the parameter controlling the threshold level at iteration i. Here the choice of λ^i is critical, since a very low λ^i may yield a single TFS by combining TFSs of all the components (occurs more often when the TFSs of the components are close to each other), on the other hand, a very large λ^i may force the segmentation algorithm to miss the TFSs of low amplitude components. After choosing an appropriate λ^i, the segmentation algorithm returns what will be called as initial time-frequency masks $M_k(t,f),\ k = 1, 2, .., K$ for each component. Then, $\tilde{T}_k(t,f) = X(t,f)M_k(t,f)$ serves as an initial estimate for the STFT of $s_k(t)$. Time-frequency translation parameters of the k^{th} component can be estimated from $\tilde{T}_k(t,f)$ by using:

$$\tilde{t}_c^k = \frac{\int\int t|\tilde{T}_k(t,f)|^2 dtdf}{\int\int |\tilde{T}_k(t,f)|^2 dtdf}, \tag{2.27}$$

$$\tilde{f}_c^k = \frac{\int\int f|\tilde{T}_k(t,f)|^2 dtdf}{\int\int |\tilde{T}_k(t,f)|^2 dtdf}. \tag{2.28}$$

Similarly, IF of $s_k(t)$ can be estimated by:

$$\tilde{f}^k(t) = \frac{\int f|\tilde{T}_k(t,f)|^2 df}{\int |\tilde{T}_k(t,f)|^2 df}. \tag{2.29}$$

Once these parameters are estimated, time-frequency translation and IF shifting are applied to the available observation:

$$\begin{aligned} x_\phi^k(t) &= x(t + t_c^k)e^{-j2\pi\phi^k(t+t_c^k)} \\ &= s_{\phi,k}(t) + \sum_{\substack{h=1 \\ h\neq k}}^{K} s_h(t + t_c^k)e^{-j2\pi\phi^k(t+t_c^k)} + n_\phi^k(t), \end{aligned} \tag{2.30}$$

where $n_\phi^k(t)$ is the resulting noise process and $s_{\phi,k}(t) = s_k(t+t_c^k)e^{-j2\pi\phi^k(t+t_c^k)}$. To obtain the scaling factor, STFT of the translated and IF shifted signal component $s_{\phi,k}(t)$ should be estimated. Let $X_\phi^k(t,f)$ denote the STFT of $x_\phi^k(t)$. To obtain an estimate of STFT of $s_{\phi,k}(t)$, one more segmentation is used on $|X_\phi^k(t,f)|^2$ providing more accurate mask $M_{\phi,k}(t,f)$ around the origin by using the segmentation threshold $p_{2,k}^i = \lambda^i|X_\phi^k(\bar{t},\bar{f})|^2 + (1-\lambda^i)\frac{\sigma^2}{F_s}$, where $|X_\phi^k(\bar{t},\bar{f})|^2$ is the maximum value of $|X_\phi^k(t,f)|^2$. By using $M_{\phi,k}(t,f)$, STFT of $s_{\phi,k}(t)$ can be estimated by $\tilde{T}_{\phi,k}(t,f) = X_\phi^k(t,f)M_{\phi,k}(t,f)$. Then, effective duration and bandwidth of $s_{\phi,k}(t)$ are obtained from $\tilde{T}_{\phi,k}(t,f)$ by using

$$\tilde{d}_\phi^k = \left[\frac{\int\int(t-\tilde{\mu}_t^k)^2|\tilde{T}_{\phi,k}(t,f)|^2dtdf}{\int\int|\tilde{T}_{\phi,k}(t,f)|^2dtdf}\right]^{1/2}, \tag{2.31}$$

$$\tilde{b}_{\phi,k} = \left[\frac{\int\int(f-\tilde{\mu}_f^k)^2|\tilde{T}_{\phi,k}(t,f)|^2dtdf}{\int\int|\tilde{T}_{\phi,k}(t,f)|^2dtdf}\right]^{1/2}, \tag{2.32}$$

where $\tilde{\mu}_t^k$ and $\tilde{\mu}_f^k$ are estimates of time and frequency averages:

$$\tilde{\mu}_t^k = \frac{\int\int t|\tilde{T}_{\phi,k}(t,f)|^2dtdf}{\int\int|\tilde{T}_{\phi,k}(t,f)|^2dtdf}, \tag{2.33}$$

$$\tilde{\mu}_f^k = \frac{\int\int f|\tilde{T}_{\phi,k}(t,f)|^2dtdf}{\int\int|\tilde{T}_{\phi,k}(t,f)|^2dtdf}. \tag{2.34}$$

Since STFT uses a window function, effective duration and bandwidth that are computed over the STFT of the signal are related with the effective duration and bandwidth of the STFT window function through the following equation [68]:

$$d_\phi^k = \sqrt{(D_\phi^k)^2 + D_g^2}, \tag{2.35}$$

$$b_\phi^k = \sqrt{(B_\phi^k)^2 + B_g^2}. \tag{2.36}$$

Here, D_ϕ^k and D_g are the true effective durations of $s_\phi^k(t)$ and the STFT window function $g(t)$, respectively, computed using (2.18). B_ϕ^k and B_g are the corresponding bandwidths computed using (2.19). d_ϕ^k and b_ϕ^k are the effective durations and bandwidths of $s_{\phi,k}(t)$ computed over its STFT, $T_{\phi,k}(t,f)$, using (2.31),(2.32). Then the scaling factor can be estimated as

$$\tilde{\nu}^k = \sqrt{\frac{(\tilde{d}_\phi^k)^2 - D_g^2}{(\tilde{b}_\phi^k)^2 - B_g^2}}. \tag{2.37}$$

As $\tilde{T}_{\phi,k}(t,f)$ approaches the true STFT of $s_{\phi,k}(t)$, the estimate in (2.37) approaches the true scaling parameters $\sqrt{[(d_{\phi}^{k})^2 - D_g^2]/[(b_{\phi}^{k})^2 - B_g^2]}$. After estimating all the transform parameters for all components $\{t_c^k, f^k(t), v^k,\ k = 1, 2, .., K\}$ at the initialization step $i = 0$ of the algorithm, the pre-processing stage is applied to the available observation $x(t)$ for each component:

$$\begin{aligned} x_s^k(t) &= x(t\nu^k + t_c^k)e^{-j2\pi\phi^k(t\nu^k + t_c^k)} \\ &= s_{s,k}(t) + \sum_{\substack{h=1 \\ h\neq k}}^{K} s_h(t\nu^k + t_c^k)e^{-j2\pi\phi^k(t\nu^k + t_c^k)} + n_s^k(t), \end{aligned} \tag{2.38}$$

where $n_s^k(t)$ is the resulting noise process and $s_{s,k}(t) = s_k(t\nu^k + t_c^k)e^{-j2\pi\phi^k(t\nu^k + t_c^k)}$. Note that, after the pre-processing operations, $n_s^k(t)$ is still circularly symmetric Gaussian noise. Then, for estimating each component, its corresponding transformed observation $x_s^k(t)$ is expanded in the HG basis. The expansion coefficients are computed by $\alpha_{n,k} = \int h_n(t)x_s^k(t)dt$ and initial estimate of each signal component is computed:

$$\tilde{s}_k^i(t) = \sum_{n=0}^{L_k} \alpha_{n,k} h_n(\frac{t - t_c^k}{\nu^k})e^{j2\pi\phi^k(t)}. \tag{2.39}$$

At this point, assume that the optimal expansion orders $L_k, k = 1, 2, .., K$ are known. At the end of this section, determination of optimal expansion orders will be explained.

Then, we start the EM iterations to further refine the component estimates. This time, for estimating the transform parameters of the k^{th} component, complete information for each component is obtained by the using the following signals: $x_k^{i+1}(t) = x(t) - \sum_{p\neq k} \tilde{s}_p^i(t)\ \forall k = 1, 2, .., K$ is used. The idea is that during the iterations $x_k^{i+1}(t)$ gets closer to a mono-component signal and hence more reliable estimates for the k^{th} component parameters can be obtained. The segmentation algorithm is run over the spectrogram of $x_k^{i+1}(t)$ with a lower threshold parameter $\lambda^{i+1} = \lambda^i c$, where $0 < c < 1$, which is typically chosen as $c = 0.8$, and the transform parameters of the k^{th} component are reestimated from the returned TFS. This parameter estimation process is repeated for all the components before the next EM iteration. The iterations are stopped when the average normalized change in signal estimates between two consecutive EM iterations

$\frac{1}{K}\sum_{k=1}^{K}\|\tilde{s}_k^{i+1}(t)-\tilde{s}_k^{i}(t)\|^2/\|\tilde{s}_k^{i+1}(t)\|^2$ is lower than a certain threshold q, which is typically chosen as 0.01.

While running the above iterative method, to obtain a reliable estimate of each component, at each iteration, the expansion orders should be chosen optimally. To simplify the notation, we will drop the superscript i, which indicates the iteration number. Since the available observation includes multiple components, the optimal approximation orders $\hat{\mathbf{L}} = [\hat{L}_1, \hat{L}_2, .., \hat{L}_K]$ should be determined jointly so that the identified supports for the components do not have significant overlaps. To determine the optimal approximation orders $\hat{\mathbf{L}}$, the expected value of the total approximation error energy $E\{\int |s(t)-\sum_{k=1}^{K}\tilde{s}_k(t)|^2 dt\}$ should be minimized over $\mathbf{L}$. Here, $s(t)=\sum_{k=1}^{K}s_k(t)$ and $\tilde{s}_k(t)$ is the order-L_k HG approximation of $s_k(t)$ given in (2.39). To simplify the presentation, we will consider discrete observation case where the bold characters denote the vector of samples of the corresponding continuous time signal. The optimal approximation orders can be estimated by minimizing the following cost function:

$$J(\mathbf{L}) = E\left\{\|\mathbf{s}-\sum_{k=1}^{K}\tilde{\mathbf{s}}_k\|^2\right\}, \tag{2.40}$$

where $\tilde{\mathbf{s}}_k = \sum_{n=0}^{L_k}\alpha_{n,k}\mathbf{g}_{n,k}$ and representation coefficients $\alpha_{n,k}$ are obtained as $\alpha_{n,k} = \mathbf{h}_n^H\mathbf{x}_s^k$ with $\mathbf{x}_s^k$ being the available observation signal obtained after the pre-processing stage applied for the k^{th} component given in (2.38). Here, $\mathbf{g}_{n,k}$ is the post-processed HG function of order n for the k^{th} component, specifically, $g_{n,k}(t) = h_n(\frac{t-t_c^k}{\nu^k})e^{j2\pi\phi^k(t)}$, where $\mathbf{h}_n$'s are orthonormalized. Then, the cost function in (2.40) can be expanded as

$$\begin{aligned} J(\mathbf{L}) = &\ E\left\{\mathbf{s}^H\mathbf{s}-2Re\left\{\sum_{k=1}^{K}\mathbf{s}^H\tilde{\mathbf{s}}_k\right\}+\sum_{k=1}^{K}\sum_{l=1}^{K}\tilde{\mathbf{s}}_k^H\tilde{\mathbf{s}}_l\right\} \\ = &-2Re\left\{\sum_{k=1}^{K}E\left\{\mathbf{s}^H\tilde{\mathbf{s}}_k\right\}\right\}\sum_{k=1}^{K}E\left\{\tilde{\mathbf{s}}_k^H\tilde{\mathbf{s}}_k\right\}+ \\ &+\sum_{k=1}^{K}\sum_{l\neq k}^{K}E\left\{\tilde{\mathbf{s}}_k^H\tilde{\mathbf{s}}_l\right\}, \end{aligned} \tag{2.41}$$

where $E\{\mathbf{s}^H\mathbf{s}\}$ term is dropped because it is not a function of $\mathbf{L}$. The first term in (2.41) can be simplified as:

$$\begin{aligned}
Re\left\{\sum_{k=1}^{K} E\left\{\mathbf{s}^H\tilde{\mathbf{s}}_k\right\}\right\} &= Re\left\{\sum_{k=1}^{K} E\left\{\mathbf{s}^H\sum_{n=0}^{L_k}\alpha_{n,k}\mathbf{g}_{n,k}\right\}\right\} \\
&= Re\left\{\sum_{k=1}^{K}\sum_{n=0}^{L_k} E\left\{\alpha_{n,k}\right\}\mathbf{s}^H\mathbf{g}_{n,k}\right\} \\
&= Re\left\{\sum_{k=1}^{K}\sum_{n=0}^{L_k} E\left\{\mathbf{h}_n^H\mathbf{x}_s^k\right\}\mathbf{s}^H\mathbf{g}_{n,k}\right\} \\
&= Re\left\{\sum_{k=1}^{K}\sum_{n=0}^{L_k} E\left\{\mathbf{h}_n^H(\mathbf{s}_s^k+\mathbf{n}_s^k)\right\}\mathbf{s}^H\mathbf{g}_{n,k}\right\}. \qquad (2.42)
\end{aligned}$$

Since $\mathbf{n}_s^k$ is zero mean,

$$\begin{aligned}
Re\left\{\sum_{k=1}^{K} E\left\{\mathbf{s}^H\tilde{\mathbf{s}}_k\right\}\right\} &= Re\left\{\sum_{k=1}^{K}\sum_{n=0}^{L_k}\mathbf{h}_n^H\mathbf{s}_s^k\mathbf{s}^H\mathbf{g}_{n,k}\right\} \\
&= Re\left\{\sum_{k=1}^{K}\sum_{n=0}^{L_k}\beta_{n,k}\beta_{n,k}^*\nu^k\right\} \\
&= \sum_{k=1}^{K}\sum_{n=0}^{L_k}\nu^k|\beta_{n,k}|^2. \qquad (2.43)
\end{aligned}$$

Here, $\mathbf{s}_s^k$ and $\mathbf{n}_s^k$ are the sum of the signal components and noise after the pre-processing stage applied for the k^{th} component in (2.38) respectively, i.e., $s_s^k(t) = s(t\nu^k + t_c^k)e^{-j2\pi\phi^k(t\nu^k+t_c^k)}$, and $n_s^k(t) = x_s^k(t) - s_s^k(t)$. The coefficient $\beta_{n,k}$ is the projection of $s_s^k(t)$ on the n^{th} HG function, i.e., $\beta_{n,k} = \mathbf{h}_n^H\mathbf{s}_s^k$, and $\mathbf{s}^H\mathbf{g}_{n,k} = \beta_{n,k}^*$ since $\int h_n(t)^*s_s(t)dt = \frac{1}{\nu^k}\int g_{n,k}(t)^*s(t)dt$. Note that pre-processing stage doesn't change the statistical properties of the noise process, which is assumed to have a circularly symmetric white Gaussian distribution with variance σ^2. The expectation in the second term in (2.41) can be computed as:

$$\sum_{k=1}^{K} E\left\{\tilde{\mathbf{s}}_k^H\tilde{\mathbf{s}}_k\right\} = \sum_{k=1}^{K} E\left\{\left(\sum_{n=0}^{L_k}\alpha_{n,k}\mathbf{g}_{n,k}\right)^H\left(\sum_{m=0}^{L_k}\alpha_{m,k}\mathbf{g}_{m,k}\right)\right\}. \qquad (2.44)$$

Since $\mathbf{g}_{n,k}^H \mathbf{g}_{m,k} = \nu^k \delta(m-n)$, it reduces to

$$\begin{aligned}
\sum_{k=1}^{K} E\left\{\tilde{\mathbf{s}}_k^H \tilde{\mathbf{s}}_k\right\} &= \sum_{k=1}^{K} E\left\{\sum_{n=0}^{L_k} \nu^k |\alpha_{n,k}|^2\right\} \\
&= \sum_{k=1}^{K} \sum_{n=0}^{L_k} \nu^k E\left\{\mathbf{h}_n^H \mathbf{x}_s^k \mathbf{x}_s^{k^H} \mathbf{h}_n\right\} \\
&= \sum_{k=1}^{K} \sum_{n=0}^{L_k} \nu^k \mathbf{h}_n^H E\left\{(\mathbf{s}_s^k + \mathbf{n}_s^k)(\mathbf{s}_s^k + \mathbf{n}_s^k)^H\right\} \mathbf{h}_n. \qquad (2.45)
\end{aligned}$$

Since $\mathbf{n}_s^k$ is circularly symmetric white Gaussian noise,

$$\begin{aligned}
\sum_{k=1}^{K} E\left\{\tilde{\mathbf{s}}_k^H \tilde{\mathbf{s}}_k\right\} &= \sum_{k=1}^{K} \sum_{n=0}^{L_k} \nu^k \mathbf{h}_n^H [\mathbf{s}_s^k \mathbf{s}_s^{k^H} + \sigma^2 \mathbf{I}] \mathbf{h}_n \\
&= \sum_{k=1}^{K} \sum_{n=0}^{L_k} \nu^k |\beta_{n,k}|^2 + \sum_{k=1}^{K} \nu^k (L_k + 1) \sigma^2, \qquad (2.46)
\end{aligned}$$

where $\mathbf{I}$ is the identity matrix. Finally, the expectation in the third term in (2.41) can be computed as:

$$\begin{aligned}
\sum_{k=1}^{K} \sum_{l \neq k}^{K} E\left\{\tilde{\mathbf{s}}_k^H \tilde{\mathbf{s}}_l\right\} &= \sum_{k=1}^{K} \sum_{l \neq k}^{K} E\left\{\left(\sum_{n=0}^{L_k} \alpha_{n,k}^* \mathbf{g}_{n,k}^H\right)\left(\sum_{m=0}^{L_l} \alpha_{m,l} \mathbf{g}_{m,l}\right)\right\} \\
&= \sum_{k=1}^{K} \sum_{l \neq k}^{K} \sum_{n=0}^{L_k} \sum_{m=0}^{L_l} E\left\{\alpha_{n,k}^* \alpha_{m,l}\right\} \xi_{n,k}^{n,l}, \qquad (2.47)
\end{aligned}$$

where $\xi_{n,k}^{m,l} = \mathbf{g}_{n,k}^H \mathbf{g}_{m,l}$. Then,

$$\begin{aligned}
\sum_{k=1}^{K} \sum_{l \neq k}^{K} E\left\{\tilde{\mathbf{s}}_k^H \tilde{\mathbf{s}}_l\right\} &= \sum_{k=1}^{K} \sum_{l \neq k}^{K} \sum_{n=0}^{L_k} \sum_{m=0}^{L_l} E\left\{\mathbf{h}_m^H \mathbf{x}_s^l \mathbf{x}_s^{k^H} \mathbf{h}_n\right\} \xi_{n,k}^{m,l} \\
&= \sum_{k=1}^{K} \sum_{l \neq k}^{K} \sum_{n=0}^{L_k} \sum_{m=0}^{L_l} \mathbf{h}_m^H E\left\{\left(\mathbf{s}_s^l + \mathbf{n}_s^l\right)\left(\mathbf{s}_s^k + \mathbf{n}_s^k\right)^H\right\} \mathbf{h}_n \xi_{n,k}^{m,l} \\
&= \sum_{k=1}^{K} \sum_{l \neq k}^{K} \sum_{n=0}^{L_k} \sum_{m=0}^{L_l} \mathbf{h}_m^H \left(\mathbf{s}_s^l \mathbf{s}_s^{k^H} + \sigma^2 \mathbf{I}\right) \mathbf{h}_n \xi_{n,k}^{m,l}. \qquad (2.48)
\end{aligned}$$

Since $\mathbf{h}_m^H \mathbf{h}_n = \delta(m-n)$,

$$\begin{aligned}\sum_{k=1}^{K}\sum_{l\neq k}^{K} E\left\{\tilde{\mathbf{s}}_k^H \tilde{\mathbf{s}}_l\right\} = &\sum_{k=1}^{K}\sum_{l\neq k}^{K}\sum_{n=0}^{L_k}\sum_{m=0}^{L_l} \beta_{m,l}\beta_{n,k}^{*}\xi_{n,k}^{m,l} \\ &+ \sigma^2 \sum_{k=1}^{K}\sum_{l\neq k}^{K}\sum_{n=0}^{\min\{L_k,L_l\}} \xi_{n,k}^{n,l}. \end{aligned} \tag{2.49}$$

Then the equation in (2.40) reduces to the following form:

$$\begin{aligned} J(\mathbf{L}) = &-\sum_{k=1}^{K}\sum_{n=0}^{L_k}\nu^k|\beta_{n,k}|^2 + \sum_{k=1}^{K}\nu^k(L_k+1)\sigma^2 \\ &+ \sum_{k=1}^{K}\sum_{l\neq k}^{K}\sum_{n=0}^{L_k}\sum_{m=0}^{L_l} \beta_{m,l}\beta_{n,k}^{*}\xi_{n,k}^{m,l} \\ &+ \sigma^2 \sum_{k=1}^{K}\sum_{l\neq k}^{K}\sum_{n=0}^{\min\{L_k,L_l\}} \xi_{n,k}^{n,l}. \end{aligned} \tag{2.50}$$

However, since we do not have access to the noise free signal $s(t)$, $\beta_{n,k}$ can not be computed directly. However, as detailed in the next derivation, $|\beta_{n,k}|^2 \approx |\alpha_{n,k}|^2 - \sigma^2$. This is because $E\{|\alpha_{n,k}|^2\} = |\beta_{n,k}|^2 + \sigma^2$.

$$\begin{aligned} E\{|\alpha_{n,k}|^2\} &= E\left\{\mathbf{h}_n^H \mathbf{x}_s^k {\mathbf{x}_s^k}^H \mathbf{h}_n\right\} \\ &= \mathbf{h}_n^H E\left\{\mathbf{x}_s^k {\mathbf{x}_s^k}^H\right\}\mathbf{h}_n \\ &= \mathbf{h}_n^H E\left\{\left(\mathbf{s}_s^k + \mathbf{n}_s^k\right)\left(\mathbf{s}_s^k + \mathbf{n}_s^k\right)^H\right\}\mathbf{h}_n \\ &= \mathbf{h}_n^H \left(\mathbf{s}_s^k {\mathbf{s}_s^k}^H + \sigma^2\mathbf{I}\right)\mathbf{h}_n \\ &= |\beta_{n,k}|^2 + \sigma^2, \end{aligned} \tag{2.51}$$

By using this approximation, the following computable cost function, which is to be minimized, is used in the proposed approach here.

$$\begin{aligned} \hat{J}(\mathbf{L}) = &-\sum_{k=1}^{K}\sum_{n=0}^{L_k}\nu^k|\alpha_{n,k}|^2 + 2\sum_{k=1}^{K}\nu^k(L_k+1)\sigma^2 \\ &+ \sum_{k=1}^{K}\sum_{l\neq k}^{K}\sum_{n=0}^{L_k}\sum_{m=0}^{L_l} \alpha_{n,k}^{*}\alpha_{m,l}\xi_{n,k}^{m,l}. \end{aligned} \tag{2.52}$$

In the above cost function, while the second term controls the effect of noise, third term controls the cross correlation between the signal estimates. For mono-component case $K = 1$, the cost function in (2.52) reduces to

$$\hat{J}(\mathbf{L})_{K=1} = -\sum_{n=0}^{L} \nu^1 |\alpha_{n,1}|^2 + 2\nu^1 (L+1)\sigma^2. \tag{2.53}$$

To simulate the performance of the expansion order estimator for mono-component signals given in (2.53), we generated ten thousand different realizations of a noisy synthetic signal of the form $x(t) = \sum_{n=0}^{\bar{L}} \alpha_n h_n(t) + n(t)$. In each realization, the HG coefficients $\alpha_n,\ n = 0, .., \bar{L}$ were chosen from a normal distribution and the noise samples $n(t)$ were generated from a zero mean Gaussian distribution, whose variance was set according to the given SNR value. For different representation orders $\bar{L}$ (ranging from 0 to 100), and different SNR values (ranging from -10dB to 10dB), we calculated the sample mean and sample standard deviation of the absolute error between the actual representation order $\bar{L}$ and its estimate $\tilde{L}$, i.e. $|\bar{L} - \tilde{L}|$. In Fig.2.10(a) and (b), these two statistical measures are plotted as a function of $\bar{L}$ for different SNR values. As observed from this plot, even for a complicated signal that is composed of as many as 100 HGs and under very low SNR values such as -10dB, the average absolute error in expansion order estimation is only around 3.5 with standard deviation of 5.5. Having discussed choosing the expansion orders optimally, the fully automated iterative method for signal component estimation is summarized in Algorithm-1.

When the signal components have overlapping TFSs, decomposing the observation signal into its components is a harder problem. Although the proposed approach is designed for analysis of signals whose time-frequency components do not have significant overlaps in the time-frequency domain, some insights for the overlapping case will be provided. Consider a signal $s(t)$, which have two components with overlapping TFSs $s(t) = s_1(t) + s_2(t)$, as demonstrated in Fig.2.11. In the figure, S_1 and S_2 denote the effective TFS of $s_1(t)$ and $s_2(t)$, respectively. S_{int} is the effective support of the overlap region. Let $\mathbb{S}[.]$ be an operator which returns the effective support of the given signal, i.e., $\mathbb{S}[s_k(t)] = S_k, k = 1, 2$, and H_0 denote the effective support of HG function of order-0, i.e., $\mathbb{S}[h_0(t)] = H_0$. The following two theorems explain the uniqueness of the decomposition of $s(t)$ into

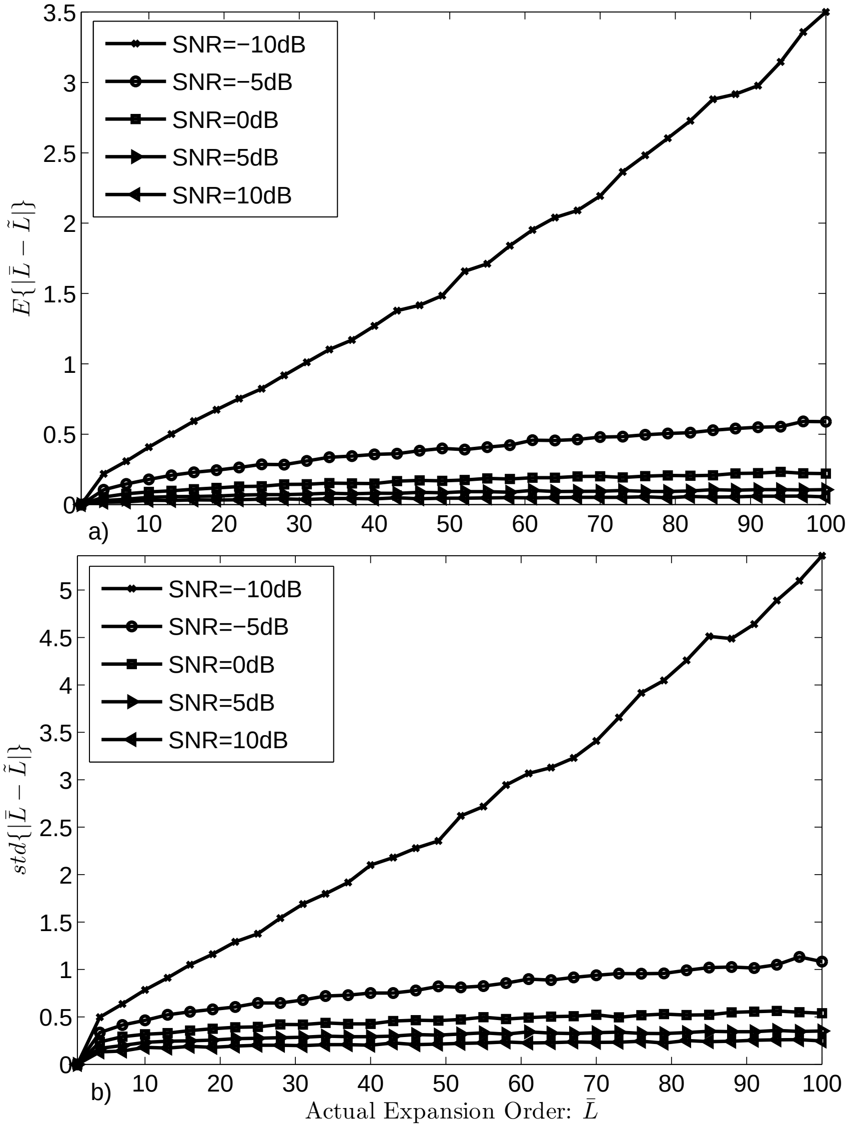

Figure 2.10: (a) Ensemble average of the absolute error between actual representation order $\bar{L}$, its estimate $\tilde{L}$ and (b) its standard deviation as a function of $\bar{L}$ for different SNR values.

Algorithm 1 Component extraction based on iterative parameter estimation

```
**Input**
A noisy observation $x(t)$ composed of compact support signal components $s_k(t), k = 1, 2, ..$
**Output**
En estimate of each signal component $\tilde{s}_k(t), k = 1, 2, ..$
**Initialization**
$i \leftarrow 0$
Set segmentation threshold parameter $\lambda^i$
Set segmentation threshold $p_1^i = \lambda^i |X(\bar{t}, \bar{f})|^2 + (1 - \lambda^i)\frac{\sigma^2}{F_s}$
Estimate $t_c^k, f^k(t)$ $\forall k = 1, 2, .., K$ by segmenting $|X(t, f)|^2$ with the segmentation threshold $p_1^i$
Compute $x_\phi^k(t)$ $\forall k = 1, 2, .., K$ by using $t_c^k, f^k(t)$
Set segmentation threshold $p_{2,k}^i = \lambda^i |X_\phi^k(\bar{t}, \bar{f})|^2 + (1 - \lambda^i)\frac{\sigma^2}{F_s}$ $\forall k = 1, 2, .., K$
Estimate $v^k$ $\forall k = 1, 2, .., K$ by segmenting $|X_\phi^k(t, f)|^2$ with the segmentation threshold $p_{2,k}^i$
Form $x_s^k(t)$ $\forall k = 1, 2, .., K$
Compute $\alpha_{n,k}, \xi_{n,k}^{m,l}$ $\forall k, l = 1, 2, .., K,\ \forall n, m = 1, 2, ..$
Solve (2.52) using $\{\alpha_{n,k}, \xi_{n,k}^{m,l}, \nu^k,\ \forall k, l = 1, 2, .., K,\ \forall n, m = 1, 2, ..\}$
Compute $\tilde{s}_k^i(t),\ \forall k = 1, 2, .., K$
$q^i = 1$
**EM Iterations**
**while** $q^i > q$ **do**
    $i \leftarrow i + 1$
    $\lambda^i = c\lambda^{i-1}$
    **for** $k = 1$ to $K$ **do**
        $x_k^i(t) \leftarrow x(t) - \sum_{p \neq k} \tilde{s}_p^{i-1}(t)$
        Set segmentation threshold $p_1^i = \lambda^i |X^k(\bar{t}, \bar{f})|^2 + (1 - \lambda^i)\frac{\sigma^2}{F_s}$
        Estimate $t_c^k, f^k(t)$ by segmenting $|X^k(t, f)|^2$ with the segmentation threshold $p_1^i$
        Compute $x_\phi^k(t)$ by using $t_c^k, f^k(t)$
        Set segmentation threshold $p_2^i = \lambda^i |X_\phi^k(\bar{t}, \bar{f})|^2 + (1 - \lambda^i)\frac{\sigma^2}{F_s}$
        Estimate $v^k$ by segmenting $|X_\phi^k(t, f)|^2$ with the segmentation threshold $p_2^i$
    **end for**
    Form $x_s^k(t)$ $\forall k = 1, 2, .., K$
    Compute $\alpha_{n,k}, \xi_{n,k}^{m,l}$ $\forall k, l = 1, 2, .., K,\ \forall n, m = 1, 2, ..$
    Solve (2.52) using $\{\alpha_{n,k}, \xi_{n,k}^{m,l}, \nu^k,\ \forall k, l = 1, 2, .., K,\ \forall n, m = 1, 2, ..\}$
    Compute $\tilde{s}_k^i(t),\ \forall k = 1, 2, .., K$
    $q^i = \frac{1}{K} \sum_{k=1}^{K} \|\tilde{s}_k^i(t) - \tilde{s}_k^{i-1}(t)\|^2 / \|\tilde{s}_k^i(t)\|^2$
**end while**
```

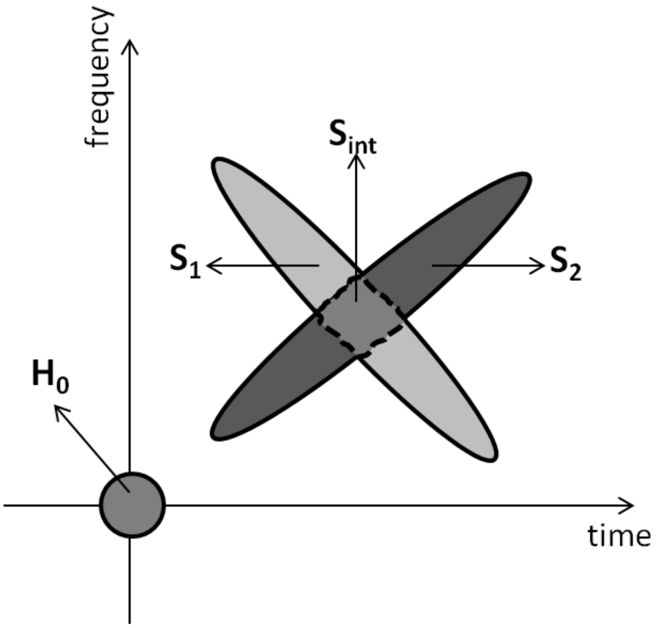

Figure 2.11: Demonstration of a multi-component signal whose components have overlapping TFSs. S_1 and S_2 are the effective TFSs of the signal components. S_{int} is the effective overlapping region. H_0 denotes the effective TFS of the HG function of order 0.

$s_1(t)$ and $s_2(t)$ according to the area of the effective intersection region between the component supports.

Theorem 1. *If the intersection region S_{int} allows covering an ellipse of area larger than or equal to the area of H_0, the decomposition $s(t) = \tilde{s}_1(t) + \tilde{s}_2(t)$ such that $\mathbb{S}[\tilde{s}_1(t)] = S_1$ and $\mathbb{S}[\tilde{s}_1(t)] = S_2$ is non-unique.*

Proof. Since area of S_{int} is larger than H_0, there exist a signal $s_{int}(t)$ with a sufficiently small energy such that $\mathbb{S}[s_{int}(t)] \subseteq S_{int}$. The decomposition can be rewritten as

$$\begin{aligned} s(t) =& \tilde{s}_1(t) + \tilde{s}_2(t) \\ =& \tilde{s}_1(t) + \tilde{s}_2(t) + s_{int}(t) - s_{int}(t) \\ =& \tilde{s}_1(t) + s_{int}(t) + \tilde{s}_2(t) - s_{int}(t) \end{aligned} \tag{2.54}$$

Since $\mathbb{S}[\tilde{s}_1(t) + s_{int}(t)] = S_1$ and $\mathbb{S}[\tilde{s}_2(t) - s_{int}(t)] = S_2$, $s(t) = [\tilde{s}_1(t) + s_{int}(t)] + [\tilde{s}_2(t) - s_{int}(t)]$ is another decomposition of $s(t)$. Hence, the decomposition is non-unique. ☐

Theorem 2. *If the intersection region S_{int} doesn't allow covering an ellipse of area larger than or equal to the area of H_0, the decomposition $s(t) = \tilde{s}_1(t) + \tilde{s}_2(t)$ such that $\mathbb{S}[\tilde{s}_1(t)] = S_1$ and $\mathbb{S}[\tilde{s}_2(t)] = S_2$ is unique.*

Proof. Assume that there exists non-unique decompositions $s(t) = \tilde{s}_1(t) + \tilde{s}_2(t)$ and $s(t) = \hat{s}_1(t) + \hat{s}_2(t)$. Then,

$$\begin{aligned} 0 =& \tilde{s}_1(t) + \tilde{s}_2(t) - \hat{s}_1(t) - \hat{s}_2(t) \\ =& [\tilde{s}_1(t) - \hat{s}_1(t)] + [\tilde{s}_2(t) - \hat{s}_2(t)] \\ =& e_1(t) + e_2(t) \end{aligned} \tag{2.55}$$

where $e_1(t) = \tilde{s}_1(t) - \hat{s}_1(t)$ and $e_2(t) = \tilde{s}_2(t) - \hat{s}_2(t)$. Since $e_1(t) + e_2(t) = 0$, then $\mathbb{S}[e_1(t)] = \mathbb{S}[e_2(t)]$. Therefore, $\mathbb{S}[e_1(t)] \subset S_{int}$ and $\mathbb{S}[e_2(t)] \subset S_{int}$. This is a contradiction since it is already assumed that area of S_{int} is smaller than H_0 and there exists no signal whose effective TFS is equal to S_{int}. Hence the decomposition is unique. ☐

In Theorem-1, it is proven that, if the overlapped region between two signal components has an area of larger than or equal to the effective support of a Gaussian atom (HG function of order 0), then the unique separation of these two components is not possible. Therefore, there exist no time-frequency analysis tools that can uniquely decompose overlapping components whenever their overlapped region is sufficiently large. Theorem-2 provides a positive result for the analysis of overlapping signal components. It states that if the overlapped area doesn't allow fitting a Gaussian atom, then the decomposition becomes unique. To extend the proposed approach to the case of overlapping signal components as described in Theorem-2, the proposed approach can be modified such that HG fitting is performed in the non-overlapping parts of the signal components after the pre-processing stage. However this extension of the proposed approach is left as a future work on the subject.

In the next section, analysis results on both simulated and real signals will be provided.

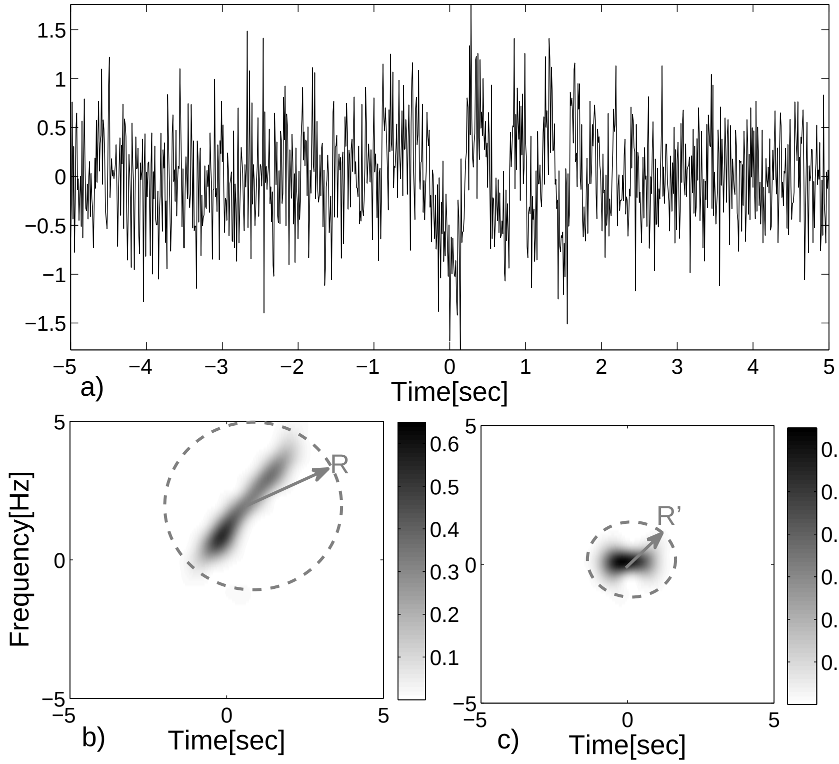

Figure 2.12: (a) Synthetically generated noisy observation of a mono-component, compact TFS signal. SNR is 0dB. Its spectrogram (b) before and (c) after preprocessing stage. R and R' represents the radius of the smallest circle that encloses the signal support. While computing the spectrograms, a Gaussian window with standard deviation $\sigma = 1/\sqrt{2\pi}$ sec was used.

2.5 Analysis of Results on Simulated and Real Signals

To demonstrate the performance of the proposed method, we conducted experiments on synthetically generated mono- and multi-component signals. For the mono-component case, the noisy observation of a compact support signal of the form:

$$s(t) = w(t; t_1, t_2)a(t)e^{-j2\pi(\alpha t^2+\beta t+\gamma)} \tag{2.56}$$

was generated. Here $a(t)$ is low-pass filtered circularly symmetric white noise, $\{\alpha, \beta, \gamma\}$ are IF parameters imposing linear frequency modulation to the signal. As shown in Fig.2.12, $w(t)$ is the time-window:

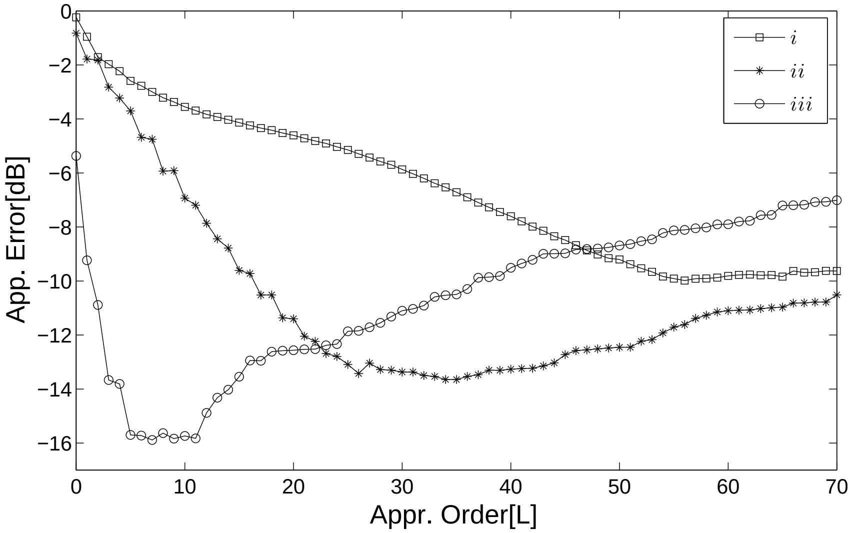

Figure 2.13: Approximation error as a function of approximation order: (*i*) If no transform is applied (marked with squares); (*ii*) If only time-frequency translation is applied (marked with stars); (*iii*) If all the proposed transforms are applied (marked with circles).

$$w(t; t_1, t_2) = \begin{cases} e^{-(t-t_1)^2/\kappa^2} & \text{if } t < t_1, \\ 1 & \text{if } t_1 \leq t \leq t_2, \\ e^{-(t-t_2)^2/\kappa^2} & \text{if } t > t_2, \end{cases} \tag{2.57}$$

forcing the signal to have a compact TFS. The noise variance was chosen such that the SNR was set to 0dB, which is defined as SNR $= 10 \log \|\mathbf{s}\|^2/(N_s\sigma^2)$ where N_s is the number of available samples along the signal support and σ^2 is the noise variance. The spectrograms of the available signal before and after the preprocessing stage are also provided in Fig.2.12(b) and (c), respectively. In a fully automated fashion, all the required parameters are estimated using signal support returned by the segmentation algorithm. In Fig.2.13, approximation error as a function of expansion order is plotted. As seen from this figure, if HG projections are directly applied to the signal without applying the proposed pre-processing technique (marked with squares), approximation error remains above −10dB. If only time-frequency translation is applied (marked with stars), the lowest approximation error achieved is around −13dB and corresponding approximation order is 35. If full scale pre-processing is applied (marked with circles), the lowest approximation error achieved is around −16dB and the corresponding expansion

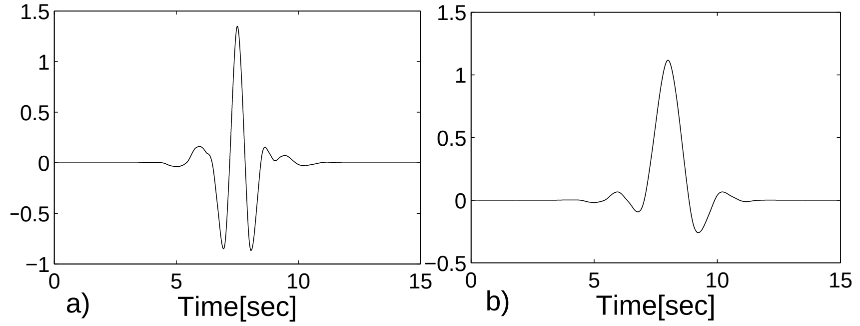

Figure 2.14: (a) Sym8 wavelet and (b) its corresponding scaling function.

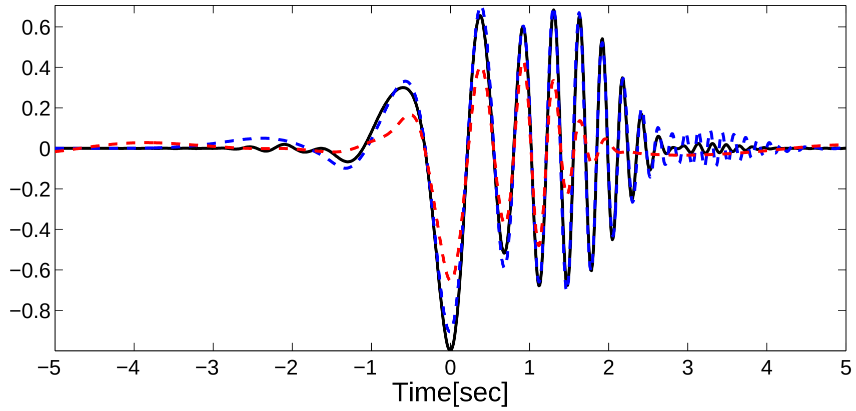

Figure 2.15: Original signal (solid-black), its approximation by proposed method (dashed-blue) and wavelet soft-thresholding technique (dashed-doted-red).

order is only 7. For this synthetic signal, we compared the performance of the proposed method with the powerful wavelet soft-thresholding technique [70]. First, discrete wavelet transform is applied to the available observation and wavelet coefficients $\xi_k, k = 0, .., N,$(N is the number of available samples) were obtained. We used the Daubechies' compactly supported, nearly linear phase wavelet *sym8* with 9 vanishing moments [71]. The *sym8* wavelet and its scaling function are shown in Fig.2.14. Then, soft thresholding is applied to the wavelet coefficients $\hat{\xi}_k$ as:

$$\hat{\xi}_k = \mathrm{sgn}(\xi_k)(|\xi_k| - \hat{\epsilon})_+ \qquad (2.58)$$

where $(.)_+$ is the non-negative part of its argument and the denoised signal was reconstructed by applying the inverse wavelet transform to the new coefficients. The threshold $\hat{\epsilon}$ was estimated according to the Stein's unbiased estimate of risk

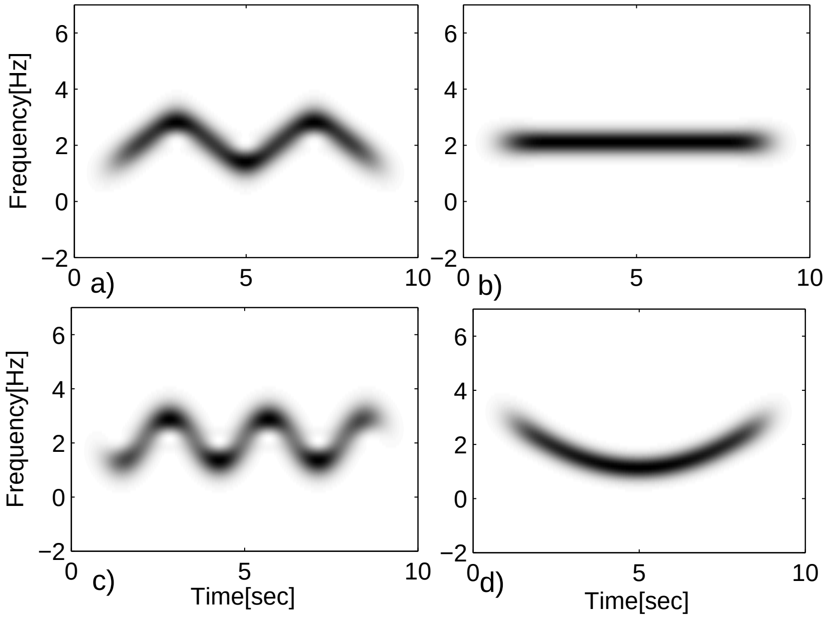

Figure 2.16: Spectrogram of the synthetic test signals with (a) triangular, (b) constant, (c) sinusoidal and (d) quadratic instantaneous frequencies.

[72]:

$$\hat{\epsilon} = \underset{0\leq\epsilon\leq\sqrt{2\log N}}{\arg\min}\big[N - 2\{k : |\xi_k \leq \epsilon|\} + \sum_{k=1}^{N}\min(|\xi_k|,\epsilon)\big] \tag{2.59}$$

In Fig.2.15, the original signal component (solid-black), its approximation by the proposed method (dashed-blue) and the wavelet soft-thresholding technique (dashed-dotted-red) are plotted. For the proposed method, the optimal expansion order is estimated by using (2.53) to be 5, which is consistent with Fig.2.13. While the proposed method achieves an approximation error of −15.2dB, the approximation error of the wavelet shrinkage technique remains around −6.8dB. As observed from this figure, although the available observations are significantly noisy, the proposed technique provides accurate estimates for the signal component.

To provide more comparison results of the proposed method with wavelet soft-thresholding technique, four more synthetic signals with triangular, constant, sinusoidal and quadratic instantaneous frequencies were generated. Spectrogram of each test signal is shown in Fig.2.16. For different SNR values, approximation errors of both methods are reported in Table-2.1. Proposed method achieved a

		Trian.	Cons.	Sin.	Quad.
SNR=0dB	Prop. Meth.	-13.6	-14.9	-14.6	-12.8
SNR=0dB	W. S. Thres.	-9.1	-10.5	-7.9	-9.8
SNR=5dB	Prop. Meth.	-17.6	-19.4	-15.6	-15.8
SNR=5dB	W. S. Thres.	-9.8	-12.8	-9	-11.6

Table 2.1: Approximation errors of the proposed method (Prop. Meth) and wavelet soft-thresholding (W. S. Thres.) for the test signals with triangular (Trian.), constant (Cons.), sinusoidal (Sin.) and quadratic (Quad) instantaneous frequencies shown in Fig.2.16, for different SNR values.

significantly lower approximation error for each test case.

For the multi-component scenario, a three-component signal is used. In this case, linear frequency modulation was imposed on the first and the second components and quadratic frequency modulation was imposed on the third component. The noisy signal and its spectrogram are shown in Fig.2.17(a) and (b), respectively. Since TFSs of the components are close to each other in the time-frequency plane, projecting the observation signal on even the time-frequency translated HGs can not yield reliable component estimates. As demonstrated in Fig.2.17(b), for each component, there is some energy leaked from the others in the region defined by the smallest circle that encloses the support of that particular component. After applying the pre-processing stage to the observation signal given in Fig.2.17 for each component separately, the spectrogram of the resulting signals are shown in Fig.2.18. Note that the radii of the smallest circles that enclose the TFSs of the components in the resulting signal R'_1, R'_3, R'_3 are considerably smaller compared to R_1, R_2, R_3 shown in Fig.2.17, decreasing the required number of HGs in the representation of the signal and hence decreasing the amount of noise fitting in the representation.

To demonstrate the performance of the proposed method on multi-component signals, synthetic signal shown in Fig.2.17 was used. For approximating each component Algorithm-1 was deployed. After 15 iterations, Algorithm-1 terminated. In Fig.2.19(a,c,e), estimated components and the actual ones at the end of the first iteration of Algorithm-1 are shown. Especially, for the low amplitude components (a) and (c), approximation error is high. In (b,d,f), results at the end of the

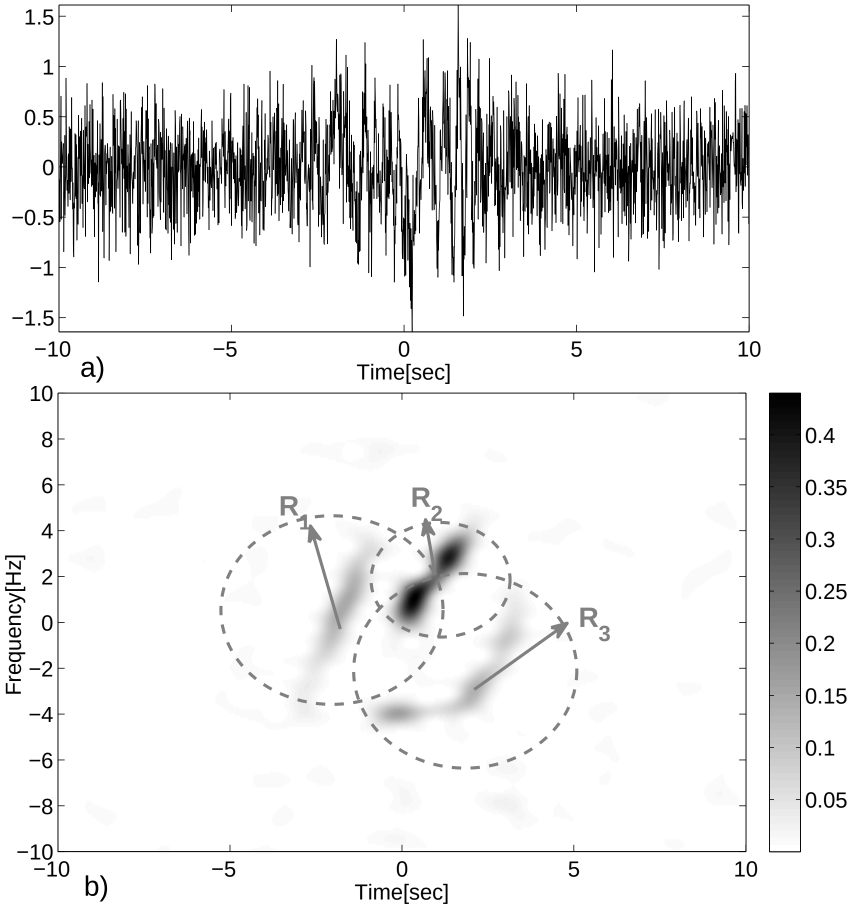

Figure 2.17: (a) Synthetically generated noisy observation of a 3-component signal and (b) its spectrogram. SNR is 0dB. R_1, R_2, R_3 represent the radius of the smallest circle that encloses the support of the first, second and third component, respectively. While computing the spectrogram, a Gaussian window with standard deviation $\sigma = 1/\sqrt{2\pi}$ sec was used.

last iteration are given. The approximation errors of the first iteration are highly reduced. Since all the signal components are detected by running Chan-Vese segmentation algorithm on the spectrogram of the available observation and all required parameters are estimated from the detected component supports, proposed method is a fully automated procedure. The effect of the incorporated segmentation technique is also investigated in the multi-component signal given in Fig.2.17. For the three components $p_1(t)$, $p_2(t)$, $p_3(t)$ in this signal, proposed method is utilized by using both Chan-Vese and Watershed segmentation [73] techniques. For each component two different estimates are obtained $\tilde{p}_k^{cv}(t), \tilde{p}_k^{w}(t), k = 1, 2, 3,$

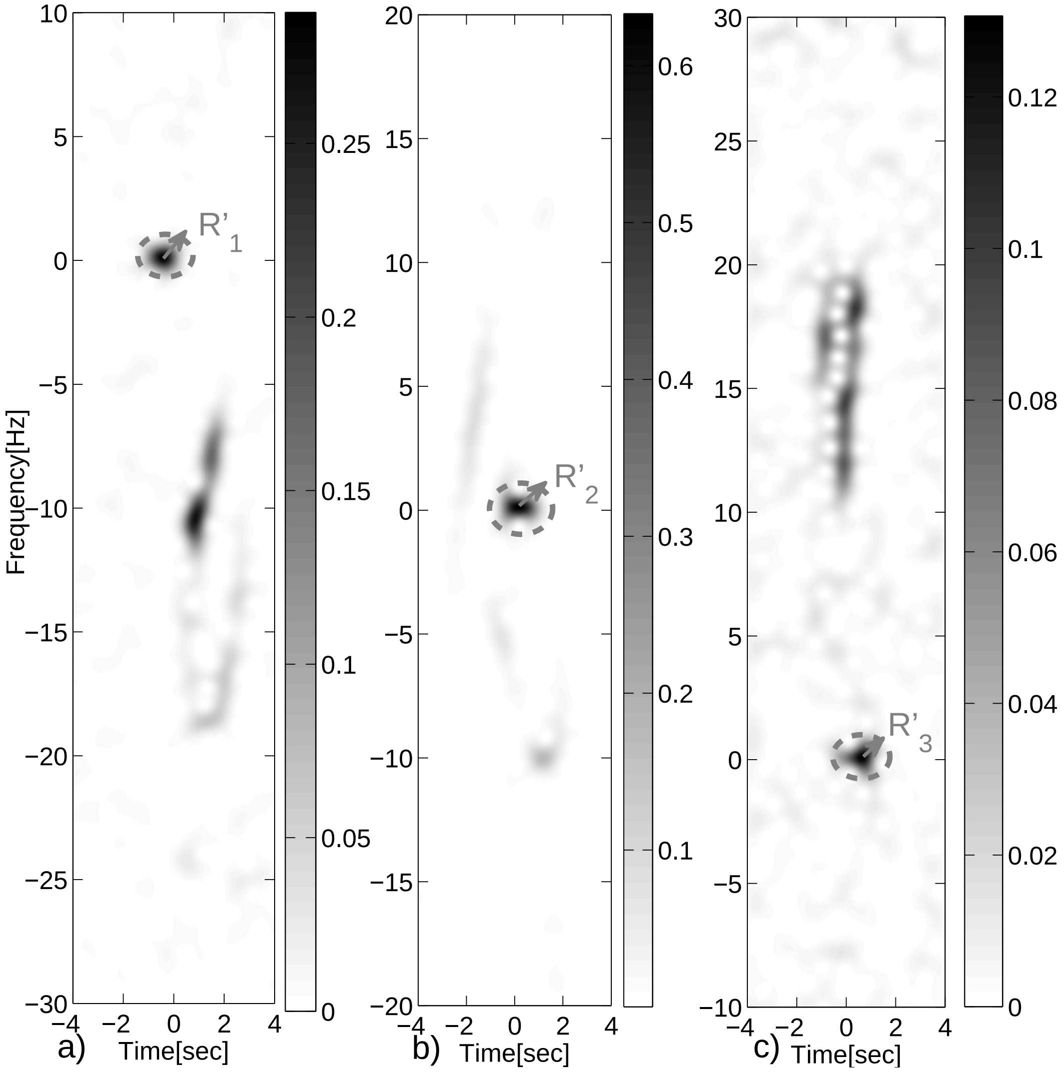

Figure 2.18: Spectrogram of the signal shown in Fig.2.17 after applying preprocessing stage by using the parameters of the (a) first, (b) second and (c) third component. R'_1, R'_2, R'_3 represent the radius of the smallest circle that encloses the support of the first, second and third component after the corresponding transformation. While computing the spectrograms, a Gaussian window with standard deviation $\sigma = 1/\sqrt{2\pi}$ sec was used.

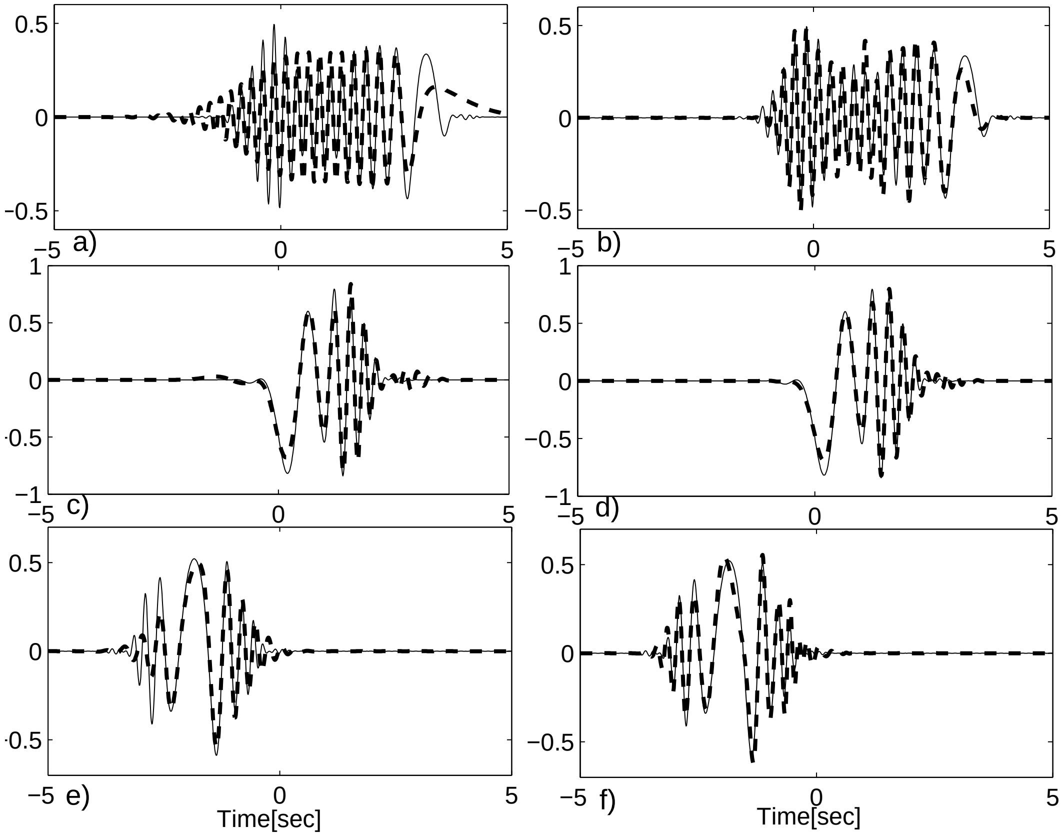

Figure 2.19: Actual (solid) and estimated (dashed) components at the end of the (a,c,e) 1^{th} and (b,d,f) 15^{th} iteration of Algorithm-1.

where the superscript cv and w denote the estimates based on Chan-Vese and Watershed segmentation techniques, respectively. The corresponding normalized approximation errors $e_k^{cv} = 10\log\left(\frac{\|p_k(t)-\tilde{p}_k^{cv}(t)\|^2}{\|p_k(t)\|^2}\right)$, $e_k^{w} = 10\log\left(\frac{\|p_k(t)-\tilde{p}_k^{w}(t)\|^2}{\|p_k(t)\|^2}\right)$ and normalized energy difference percentages $ed_k = 100\frac{\|\tilde{p}_k^{cv}(t)-\tilde{p}_k^{w}(t)\|^2}{\|\tilde{p}_k^{cv}(t)\|^2}$ are tabulated in Table-2.2. As observed, there is no significant difference between the signal components estimate by utilizing two different segmentation techniques.

Finally, we tested our method on two real signals. The first one is the bat echolocation signal [74] shown in Fig.2.20a. It is a 2.8msec echolocation pulse emitted by the Large Brown Bat, Eptescius Fuscus. We added synthetically generated circularly symmetric white noise such that the SNR was set to 0dB. The resulting noise corrupted signal and its spectrogram are shown in Fig.2.20(b) and (c), respectively. By applying the proposed multi-component analysis technique,

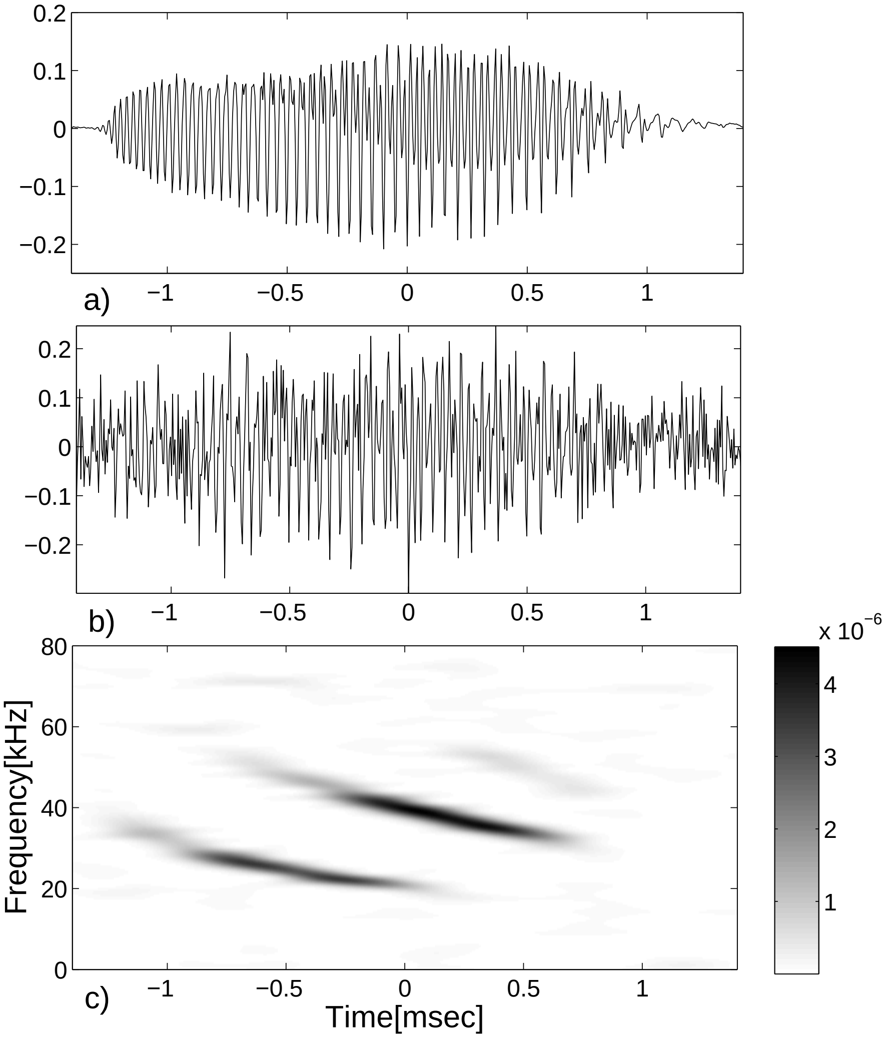

Figure 2.20: (a) Echolocation pulse emitted by the Large Brown Bat, Eptescius Fuscus; (b) its noisy version at 0dB; (c) spectrogram of the noisy signal. While computing the spectrogram in (b), a Gaussian window with standard deviation $\sigma = 14 \times 10^{-5}$sec was used.

Norm. App. Err/ Comp.	$p_1(t)$	$p_2(t)$	$p_3(t)$
e^{cv}	-14.7	-16.1	-14.3
e^{w}	-14.3	-15.6	-14.8
ed	0.17	0.25	0.21

Table 2.2: Normalized approximation error and energy difference for each component estimated by utilizing Chan-Vese and Watershed segmentation techniques in the proposed method.

the strongest 3 components have been identified and extracted. The approximation orders were estimated to be 4 for the first (occurring at time 0.5msec and 50kHz), 9 for the second (occurring at time 0.1msec and 40kHz) and 8 for the third component (occurring at time -0.5msec and 25kHz), using (2.52). The sum of estimated components is plotted in Fig.2.21(a). The normalized approximation error between this signal and the original one shown in Fig.2.20(a) is around -11.7dB. This error was around -14.8dB when we analyzed the original noise-free signal. Its spectrogram is given in Fig.2.21(b). Comparing this plot with Fig.2.20(c), proposed multi-component analysis method estimated the signal components reliably.

To obtain a high resolution time-frequency representation of this multi-component signal, we used Wigner-Ville distribution (WVD). WVD provides the highest time-frequency resolution for a mono-component signal which has linear frequency modulation. However, direct computing WVD of a multi-component signal generates alien energy localizations, which do not actually exist in the signal, in the resulting time-frequency representation. These alien energy localizations are referred as cross-terms or cross-cross-terms. To eliminate cross-terms, WVD of each component estimated by the proposed method is computed and superposed. However, since none of the estimated components has exact linear instantaneous frequency, WVD of each component still has alien energy localizations. This time, these alien energy localizations are referred as auto-cross terms. Auto-cross terms can also be eliminated by the proposed method. When the pre-processing stage is applied to the signal component, the resulting signal has its component under analysis with a compact circular support without significant non-linear frequency variation. Once HG representation is applied on to the signal extracting the component under analysis, the obtained signal doesn't generate auto-cross terms in its WVD. Then, inverse transforms (post-processing stage) is applied to the computed WVD. Let $\tilde{s}_s^k(t),\ k = 1,2,3$ denote the estimate of the k^{th} component after the pre-processing stage given in (2.38) and $WV_s^k(t,f)$ denote its WVD . The auto-cross-term-free WVD of $\tilde{s}_k(t)$ is given by:

$$WV^k\left(t,f\right) = \frac{1}{v^k} WV_s^k\left(\frac{t-t_c^k}{v^k}, v^k(f - f^k(t))\right), \tag{2.60}$$

where and $\{t_c^k, f^k(t), v^k\},\ k = 1,2,3$ are the transform parameters. The sum $WV(t,f) = WV^1(t,f) + WV^2(t,f) + WV^3(t,f)$ is both auto-cross term and cross-cross-term free WVD of the bath echolocation pulse and shown in Fig.2.21(c).

The second real signal that we analysed is a 2 sec EEG recording (1 sec pre, 1 sec post stimulus), stimulated by an oddball paradigm shown in Fig.2.22 [75]. Only the post stimulus region (time $>$ 0sec) was analysed. 3 components were identified and extracted by the proposed method. Estimated components $c_1(t), c_2(t), c_3(t)$ are shown in Fig.2.23(a),(b),(c), respectively. In Fig.2.24(a), the original recording $x(t)$ (solid-black) and sum of the estimated components $\tilde{c}(t) = c_1(t) + c_2(t) + c_3(t)$ are plotted. To provide comparisons, wavelet based denoising method in [75] has also been implemented and applied to the recording only for the post stimulus interval. The resulting denoised signal $\hat{c}(t)$ (dashed-dotted-red) is given in Fig.2.24(a). In Fig.2.24(b), the residuals $\tilde{r}(t) = x(t) - \hat{x}(t)$ (dashed-blue) and $\hat{r}(t) = x(t) - \hat{c}(t)$ are also shown. As observed, superposition of the estimated components by our method provides a better fit to the original recording. Note that, while the wavelet method returns only the total denoised signal, our method is capable of providing each individual signal component buried in the available observation.

2.6 Conclusions for Chapter 2

A new fully automated signal analysis technique is proposed for decomposition of signals into its components that have compact TFSs. The proposed approach utilizes HG functions that are adapted to the identified TFSs of the individual signal components. To fully achieve the optimal localization properties of the

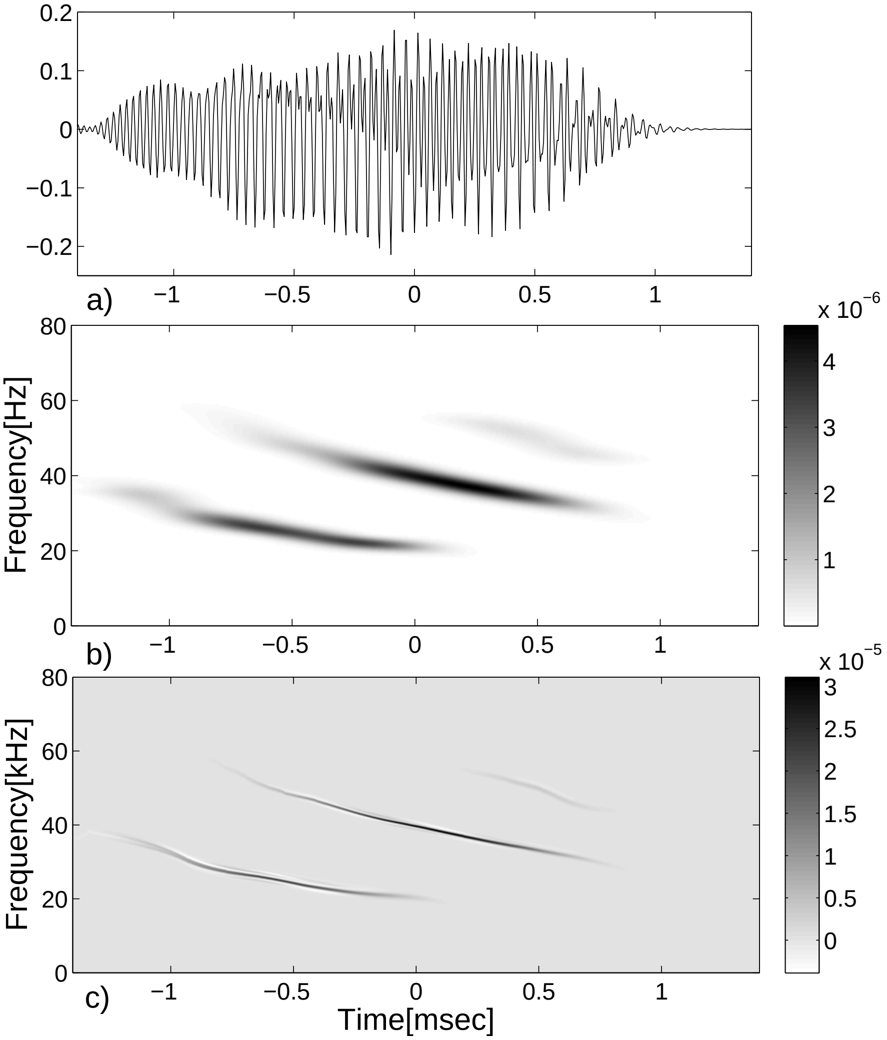

Figure 2.21: (a) Sum of the estimated components and (b) its spectrogram. While computing the spectrogram, a Gaussian window with standard deviation $\sigma = 14 \times 10^{-5}$ sec was used. (c) Obtained both auto-cross-term and cross-cross-term free Wigner-Ville distributions of the echolocation pulse.

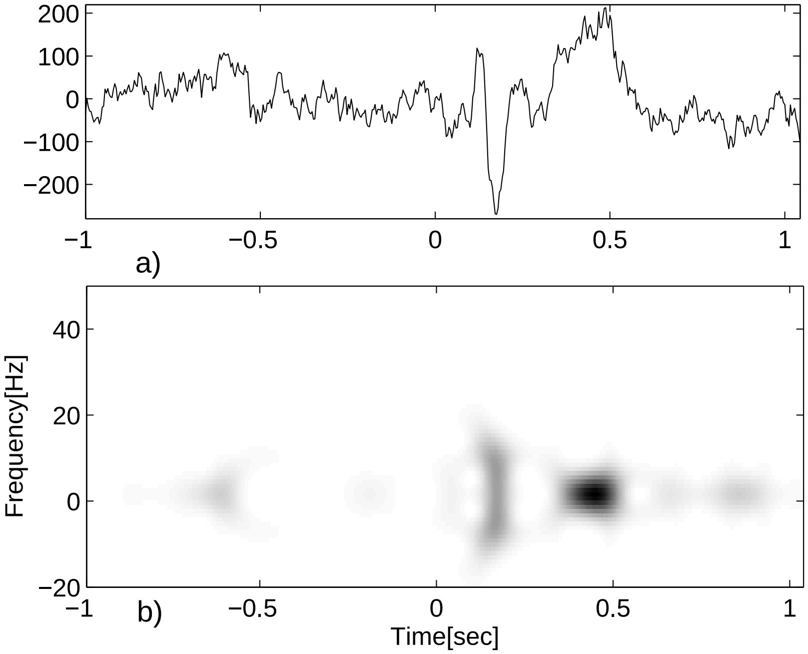

Figure 2.22: (a) EEG recording and (b) its spectrogram. While computing the spectrogram, a Gaussian window with standard deviation $\sigma = 0.1/\sqrt{2\pi}$ sec was used.

HG function expansion, a pre-processing technique is developed to transform the support of a chosen signal component to a circular one centered around the origin. Also an EM like iterative procedure is developed for accurate analysis of multi-component signals. Robust techniques are introduced for reliable estimation of pre-processing and expansion parameters. Obtained results show that proposed method provides reliable identification and extraction of signal components even under severe noise cases.

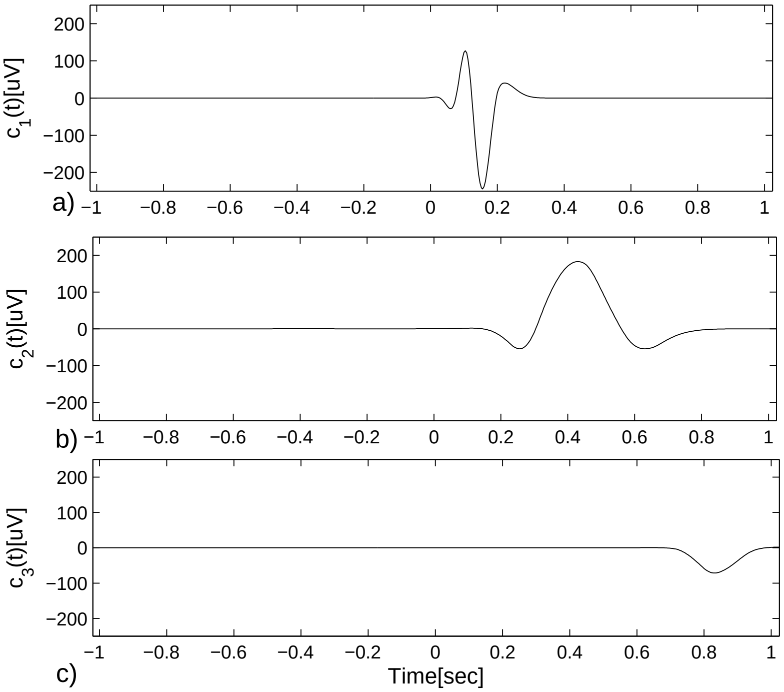

Figure 2.23: Estimated signal components (a-c) from the EEG recording shown in Fig.2.22.

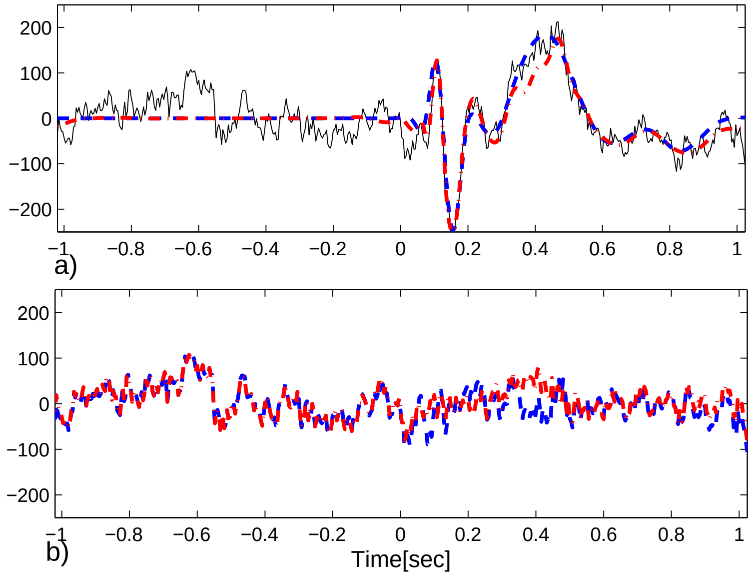

Figure 2.24: (a) Original EEG recording (solid-black), sum of the estimated components (dashed-blue), wavelet denoising result (dotted-dashed-red). (b) Residuals for the proposed method (dashed-blue) and wavelet denoising (dotted-dashed-red).

Chapter 3

UWB Orthogonal Pulse Shape Set Design by Using Hermite-Gaussian Functions

3.1 Introduction

The emerging ultra-wideband (UWB) technology has attracted great attention for designing systems for short range, high data rate communications [12, 13, 14, 15]. Since the pulse shapes used by UWB communication systems has short durations in the order of nano seconds, these systems occupy a very broad spectrum and hence cause interference to the existing wireless communication systems in the vicinity. To avoid this problem, U.S. Federal Commission of Communications (FCC) has released the spectral mask, shown in Fig.3.1, imposing restrictions on the spectrum of the pulse shapes used by the UWB systems [16]. Some researchers have defined more strict spectral masks, which is also shown in Fig.3.1 to account for multipath regrowth. Although the spectral mask restricts the transmission power of the UWB system, at the receiver side high transmission power is required to improve the detection performance. As a result, designing high energy pulse shapes satisfying the spectral mask has become a widely investigated research

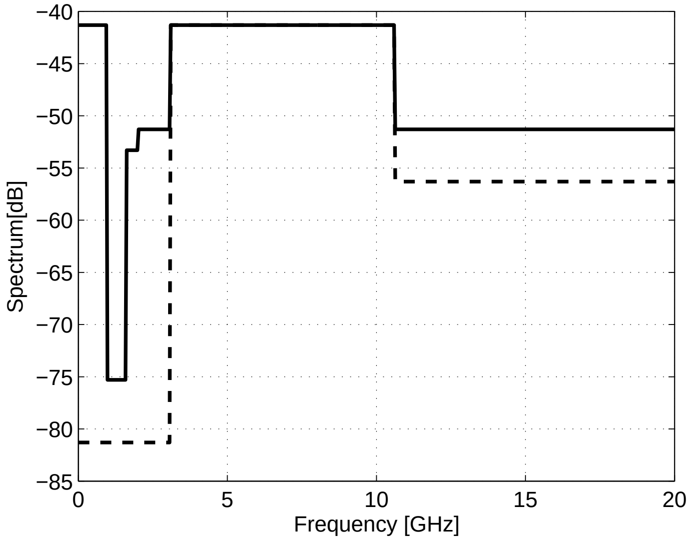

Figure 3.1: Specktral mask defined by FCC (solid) and a more strict spectral mask for accounting multipath regrowth (dashed).

problem.

In [76], projection on to convex sets is applied for designing a single pulse. The single pulse shape design problem has been extended to designing multiple orthogonal pulse shapes to further increase the data rate and the channel utilization. In [17], pulse shapes are obtained by computing the dominant eigenvectors of a channel matrix constructed by sampling the spectral mask. However, in this way only a low number of orthogonal pulse shapes could be generated and their pulse shapes do not efficiently utilize the spectral mask, resulting in a decrease on SNR at the receiver side. In [18], each pulse is represented as a linear combination of time shifted Gaussian mono-pulses. A sequential design procedure has been proposed, where at each step a single pulse shape is constructed by solving a convex optimization problem. The performance of this method is improved by inserting a phase adaptation routine to each step of the sequential design procedure for achieving a better phase match between spectral mask and the designed pulse shapes [19]. Hermite-Gaussian (HG) functions have also been used for designing UWB orthogonal pulse shapes because of their optimal time-frequency localization characteristics. Since, HG functions constitute an orthogonal family which occupies the smallest area in the time-frequency plane, they are very essential for representing signals which are constrained both in time and frequency [8]. In [20], a circuit topology is proposed for generating HG functions to be used for pulse shape generation in UWB communication systems. In [21], a procedure for designing orthogonal pulse shapes, where each pulse is modelled as linear combination of HGs, has been proposed. However, obtained pulse shapes do not effectively utilize the spectral mask.

In all of the approaches listed above, designed orthogonal pulse shapes are used as the correlators at the receiver. However, high-efficiency antennas are typically resistive-capacitive devices which often behave as differentiators [22, 23]. As a result, when the designed orthogonal pulses arrive at the receiver, they are no more orthogonal. Basically, a scaled second derivative of the pulse is received at the receiver. To solve this problem, one approach would be using integrators at the receiver. However, since the pulse duration is extremely short, there would be severe problems in the hardware implementation. Another approach is to design the pulse shapes such that their second derivatives are orthogonal. This time second derivatives of the pulse shapes should be generated at the receiver to form the correlating functions, which would lead to different transmitter-receiver structures. Also implementing the hardware which generates second derivatives of the pulse shapes having durations around one nanosecond at the receiver would not be straight forward. To overcome this problem in [24], pulse shapes are constructed as combinations of elementary HG functions with weighting coefficients derived by employing orthogonal-triangular factorization (QR) of the model matrix which ensures the orthogonality of the received pulse shapes at the receiver. However, no spectral constraints on the pulses have been considered. In [25], a simplified suboptimal structure for non-matched correlation detection is proposed, where the received pulses are correlated with the locally generated HG pulses. Although the generated pulses are adapted the spectral mask, the method is suboptimal.

In this chapter, we propose three different approaches for designing high energy UWB pulse shapes, which are orthogonal at the receiver and satisfy the spectral mask in the air, by considering the differentiating affect of the transmitting and receiving antennas. Each pulse shape is represented as a linear combination of time-shifted and scaled HG functions. The transmitting and receiving antennas are modelled as differentiators with a certain gain. Although three different optimization problems are constructed, all of them use the following design criteria: 1) Energy of the received pulse shapes in their effective passband should be maximized to improve the detection performance at the receiver side; 2) Designed pulse shapes should satisfy the spectral mask on the air; 3) Duration of the pulse shapes should be smaller than the given pulse duration at the transmitter side; 4) All the pulse shapes should be orthogonal at the receiver side. We also show that derivative of any HG function can be represented by a known linear combination of the HGs. By using this fact, a very simple receiver structure for preserving the orthogonality of the pulses at the receiver side is proposed.

The organization of this chapter is as follows: In Section 3.2, problem formulation is introduced. Transmit/receive antenna model is detailed in Section 3.3. In Section 3.4, pulse model is introduced. Dictionary design for representing the pulse shapes is given in Section 3.5. Proposed transmitter and receiver structure is provided in Section 3.6. Section 3.7 is reserved for design examples. Finally, concluding remarks for chapter 3 are given in Section 3.8.

3.2 Problem Formulation

Let $p_n(t), n = 1, 2, .., N_p$ denote the pulse shapes generated at the transmitter. Let $g_n(t), n = 1, 2, .., N_p$ denote the transmitted pulse through the antenna system and let $r_n(t), n = 1, 2, .., N_p$ denote the received pulses at the output of the receiving antenna system. Given the spectral mask $M(f)$ and allowed pulse duration T_p as design constraints, the UWB pulse shape design problem can be stated by the following optimization problem[1]:

$$\begin{aligned}
\max_{p_1(t),p_2(t),..,p_{N_p}(t)} \quad & \sum_{n=1}^{N_p} \int_{F_p} |R_n(f)|^2 df \\
\text{s.t. } & |G_n(f)|^2 \leq M(f),\ n = 1,..,N_p, \\
& T_{p_n} \leq T_p,\ n = 1,..,N_p, \\
& \int r_n(t) r_m(t) dt = 0,\ n,m = 1,..,N_p,\ n \neq m,
\end{aligned} \tag{3.1}$$

where $R_n(f)$ and $G_n(f)$ are the Fourier transforms of $r_n(t)$ and $g_n(t)$, respectively. T_{p_n} is the effective duration of $p_n(t)$ and F_p is its effective passband. Here, the benefit function is cast as superposition of energy of the received pulse shapes. The first constraint forces the pulses, which propagate from transmitter to the receiver, to satisfy the spectral mask. The second constraint puts an upper limit on the pulse durations. The last constraint ensures the orthogonality of the pulses at the receiver.

Rather than maximizing the total energy of the pulses, a max-min type benefit function could also be constructed leading to the following optimization problem:

$$\begin{aligned}
\max_{p_n(t)} \ \min_{n \in \{1,2,..,N_p\}} \quad & \int_{F_p} |R_n(f)|^2 df \\
\text{s.t. } & |G_n(f)|^2 \leq M(f),\ n = 1,..,N_p, \\
& T_{p_n} \leq T_p,\ n = 1,..,N_p, \\
& \int r_n(t) r_m(t) dt = 0,\ n,m = 1,..,N_p,\ n \neq m.
\end{aligned} \tag{3.2}$$

In this setting, the minimum pulse energy is to be maximized, which results in a set of pulses about the same energy level. On the other hand, pulse shapes obtained as the solution to (3.1) may have significantly different energy levels.

In (3.1) and (3.2), all the pulse shapes are obtained through a joint optimization. To reduce the complexity, a sequential design methodology may also be used [18, 19]. Assume that $n-1$ orthogonal pulses have already been designed.

---

[1] All the integrals in this chapter are computed from $-\infty$ to ∞ unless otherwise is stated.

The following optimization problem can be cast to obtain the n^{th} pulse shape:

$$
\begin{aligned}
\max_{p_n(t)} \; & \int\limits_{F_p} |R_n(f)|^2 df \\
& \text{s.t. } |G_n(f)|^2 \leq M(f), \\
& T_{p_n} \leq T_p \;, \\
& \int r_n(t) r_m(t) dt = 0, \;\; m = 1, 2, .., n-1.
\end{aligned}
\tag{3.3}
$$

In sequential pulse shape design methodology, the first pulse is designed by solving (3.3) with no orthogonality constraints. The remaining pulses will be designed by solving (3.3) sequentially for $n = 2, .., N_p$. In the next section the effect of transmitting and receiving antennas on the pulse shapes and corresponding mathematical model will be investigated.

3.3 Transmit/Receive Antenna Model

High-efficiency antennas are typically resistive-capacitive devices which often behave as differentiators [22, 23]. We model each antenna in transmitter and receiver as differentiators with a certain gain factor, hence the following relations between the generated pulse in the transmitter, pulse transmitted by the antenna and the pulse received at the output of the receiver antenna are assumed:[2]

$$g_n(t) = \alpha_t p'_n(t), \tag{3.4}$$

$$r_n(t) = \alpha_r g'_n(t) = \alpha_t \alpha_r p''_n(t). \tag{3.5}$$

Here, α_t and α_r are the gain factors of the transmitter and receiver antennas, respectively.

To mathematically describe the duration constraint in (3.1), (3.2) and (3.3), the following definition for the effective duration of a pulse shape will be used:

$$\int (1 - \lambda(t)) |p_n(t)|^2 dt < \zeta, \tag{3.6}$$

---

[2] $()'$ and $()''$ indicate the first and second derivative of the underlying function with respect to its argument.

where $\lambda(t)$ is the rectangular window function, which is 1 for $t \in [0, T_p]$ and 0 else, and ζ is the energy threshold. With this definition, energy of the pulse shape outside the $[0, T_p]$ interval is restricted to be less than ζ. Since the transmitted pulse $g_n(t)$ is constrained by the frequency mask, then the generated pulse at the transmitter $p_n(t)$ should satisfy

$$|P_n(f)|^2 \leq \frac{M(f)}{\alpha_t^2 |j\pi f|^2} \; \forall f. \tag{3.7}$$

Then, ζ can be chosen as

$$\zeta = \gamma \int\limits_{F_p} \frac{M(f)}{\alpha_t^2 |j\pi f|^2} df, \tag{3.8}$$

where γ is the threshold parameter, which is typically chosen as $\gamma = 0.0001$. In the following section the model that we use for representing the pulse shapes will be detailed.

3.4 Pulse Subspace

In all the three approaches for orthogonal pulse shape design problem in Section 3.2, optimization variables are the pulse shapes, which are continuous functions of time. Hence, each optimization problem is infinite dimensional. The search space can be reduced to a finite dimensional space by using a parametric pulse model. Consider the following model for the n^{th} pulse shape to be designed:

$$p_n(t) = \sum_{k=1}^{K} \alpha_{n,k} q_k(t) = \mathbf{Q}(t)\boldsymbol{\alpha}_n \tag{3.9}$$

where $\mathbf{Q}(t) = [q_1(t), .., q_K(t)]$ is the signal dictionary, whose elements are linearly independent, and $\boldsymbol{\alpha}_n = [\alpha_{n,1}, .., \alpha_{n,K}]^T$ is the coefficient vector for the n^{th} pulse shape generated at the transmitter. With this model, each pulse is considered as a superposition of the elements of the signal dictionary $\mathbf{Q}(t)$ and represented by its coefficient vector $\boldsymbol{\alpha}_n$. Inserting (3.9) in (3.1), we have the following finite dimensional optimization problem:

$$\begin{aligned} \min_{\boldsymbol{\alpha}_1,\boldsymbol{\alpha}_2,..,\boldsymbol{\alpha}_{Np}} \quad & -\sum_{n=1}^{N_p} \boldsymbol{\alpha}_n^H \mathbf{A} \boldsymbol{\alpha}_n \\ \text{s.t. } & \boldsymbol{\alpha}_n^H \mathbf{B}_k \boldsymbol{\alpha}_n \leq \hat{m}_k,\ n = 1,..,N_p,\ k = 1,..,N_f, \\ & \boldsymbol{\alpha}_n^H \mathbf{C} \boldsymbol{\alpha}_n \leq \zeta,\ n = 1,..,N_p, \\ & \boldsymbol{\alpha}_n^H \mathbf{D} \boldsymbol{\alpha}_m = 0,\ n, m = 1,..,N_p,\ n \neq m. \end{aligned} \tag{3.10}$$

Here, $\mathbf{A} = \int_{F_p} \hat{\mathbf{Q}}_2(f)^H \hat{\mathbf{Q}}_2(f) df$, $\mathbf{B}_k = Re\{\hat{\mathbf{Q}}_1(f_k)^H \hat{\mathbf{Q}}_1(f_k)\}$, $\hat{m}_k = M(f_k)$, $\mathbf{C} = \int (1 - \lambda(t)) \mathbf{Q}(t)^H \mathbf{Q}(t) dt$ and $\mathbf{D} = \int \mathbf{Q}_2(t)^H \mathbf{Q}_2(t) dt$, where $\hat{\mathbf{Q}}_1(f)$ is the Fourier transform of $\mathbf{Q}_1(t)$, $\hat{\mathbf{Q}}_2(f)$ is the Fourier transform of $\mathbf{Q}_2(t)$, with $\mathbf{Q}_1(t) = \alpha_t \mathbf{Q}'(t)$ and $\mathbf{Q}_2(t) = \alpha_t \alpha_r \mathbf{Q}''(t)$. The maximization in P_1 is replaced with a minimization by negating its benefit function. Note that, the frequency variable in the first constraint of P_1 is uniformly sampled at N_f frequency points and finite number of mask constraints is also attained. The frequency sampling is performed dense enough (N_f can be chosen as $N_f = 15 \times N_p \times K$, where D is the dimension of the problem, according to [77]) to converge to the same optimal solution. Similarly, (3.2) and (3.3), respectively, take the following forms:

$$\begin{aligned} \min_{\boldsymbol{\alpha}_n} \max_{n \in \{1,2,..,N_p\}} \quad & -\boldsymbol{\alpha}_n^H \mathbf{A} \boldsymbol{\alpha}_n \\ \text{s.t. } & \boldsymbol{\alpha}_n^H \mathbf{B}_k \boldsymbol{\alpha}_n \leq \hat{m}_k,\ n = 1,..,N_p,\ k = 1,..,N_f, \\ & \boldsymbol{\alpha}_n^H \mathbf{C} \boldsymbol{\alpha}_n \leq \zeta,\ n = 1,..,N_p, \\ & \boldsymbol{\alpha}_n^H \mathbf{D} \boldsymbol{\alpha}_m = 0,\ n, m = 1,..,N_p,\ n \neq m. \end{aligned} \tag{3.11}$$

$$\begin{aligned} \min_{\boldsymbol{\alpha}_n} \quad & -\boldsymbol{\alpha}_n^H \mathbf{A} \boldsymbol{\alpha}_n \\ \text{s.t. } & \boldsymbol{\alpha}_n^H \mathbf{B}_k \boldsymbol{\alpha}_n \leq \hat{m}_k,\ k = 1,..,N_f, \\ & \boldsymbol{\alpha}_n^H \mathbf{C} \boldsymbol{\alpha}_n \leq \zeta \hat{m}, \\ & \boldsymbol{\alpha}_n^H \mathbf{D} \boldsymbol{\alpha}_m = 0,\ m = 1,..,n-1. \end{aligned} \tag{3.12}$$

In (3.10) and (3.11), the dimension of the problem is $N_p \times K$, where K is the size of the dictionary $\mathbf{Q}(t)$, and the number of constraints is $N_p(N_f + (N_p + 1)/2)$. Also, in these two formulations, the constructed optimization problem is non-convex. The sequential design methodology decreases the problem dimension and the number of constraints. In (3.12) problem dimension is K and the number of constraints is N_f+n. Moreover, (3.12) can be converted to a convex optimization problem by defining the following cost function [18]:

$$\begin{aligned} J &= \int\limits_{F_p} \left|\sqrt{M(f)}e^{j\phi(f)} - P_n(f)\right|^2 df \\ &= \int\limits_{F_p} \left|\sqrt{M(f)}e^{j\phi(f)} - \mathbf{Q}(f)\boldsymbol{\alpha}_n\right|^2 df, \end{aligned} \tag{3.13}$$

where $\phi(f)$ is the phase of the spectral mask $M(f)$, which is assumed to be known. Later on, this assumption will be removed by choosing $\phi(f)$. The cost function in (3.13) computes the energy of the difference between the spectral mask and the designed pulse. Note that, given the power spectral density $M(f)$ and the phase $\phi(f)$, $\sqrt{M(f)}e^{j\phi(f)}$ serves as the frequency domain representation of the spectral mask. Inserting (3.13) into (3.12), we have the following convex optimization problem[3]:

$$\begin{aligned} \min_{\boldsymbol{\alpha}_n} \; & -\boldsymbol{\alpha}_n^H \mathbf{A} \boldsymbol{\alpha}_n + 2\mathbf{r}^H \boldsymbol{\alpha}_n \\ \text{s.t. } & \boldsymbol{\alpha}_n^H \mathbf{B}_k \boldsymbol{\alpha}_n \leq \hat{m}_k, \; k = 1, .., N_f, \\ & \boldsymbol{\alpha}_n^H \mathbf{C} \boldsymbol{\alpha}_n \leq \zeta \;, \\ & \boldsymbol{\alpha}_n^H \mathbf{D} \boldsymbol{\alpha}_m = 0, \; m = 1, .., n-1, \end{aligned} \tag{3.14}$$

where $\boldsymbol{r}^H = -\int_{F_p} Re\{\sqrt{M(f)}e^{-j\phi(f)}\mathbf{Q}(f)\}df$. (3.14) is a QCQP (Quadratically Constrained Quadratic Problem) and can be solved at the global optimum point by converting it to a SOCP (Second Order Cone Program) as [78]:

$$\begin{aligned} \min_{\boldsymbol{\alpha}_n, t} \; & -t + 2\mathbf{r}^H \boldsymbol{\alpha}_n \\ \text{s.t. } & \|\hat{\mathbf{A}}\boldsymbol{\alpha}_n\|^2 \leq t, \\ & \|\hat{\mathbf{B}}_k \boldsymbol{\alpha}_n\| \leq \hat{m}_k^{1/2}, \; k = 1, .., N_f, \\ & \|\hat{\mathbf{C}}_\lambda \boldsymbol{\alpha}_n\| < \zeta^{1/2}\hat{m}^{1/2}, \\ & \boldsymbol{d}_m^H \boldsymbol{\alpha}_n = 0, \; m = 1, .., n-1, \end{aligned} \tag{3.15}$$

where $\hat{\mathbf{A}}$ and $\hat{\mathbf{C}}$ are the matrices such that $\hat{\mathbf{A}}^H\hat{\mathbf{A}} = \mathbf{A}$ and $\hat{\mathbf{C}}^H\hat{\mathbf{C}} = \mathbf{C}$. $\hat{\mathbf{B}}_k = Re\{\mathbf{Q}(f_k)\}$ and $\mathbf{d}_m = \mathbf{C}^H\boldsymbol{\alpha}_m$. Any SOCP solver can be deployed for solving (3.15). In this work SeDuMi is used for the solution of (3.15) [79].

---

[3] All the norms defined as $\|.\|$ indicate l_2 norm unless otherwise is stated.

Algorithm 2 Orthogonal Pulse Shape Set Design by Iterative Phase Adaptation

```
1: Initialization:
2: $\phi^0(f) = 0,\ \boldsymbol{\alpha}_n^0 = 0,\ i = 1$
3: Iterations:
4: Find optimal $\boldsymbol{\alpha}_n^i$ by solving (3.15)
5: $P_n^i(f) = \hat{\mathbf{Q}}(f)\boldsymbol{\alpha}_n^i$
6: $\phi^i(f) = \angle P_n^i(f)$
7: if $\|\boldsymbol{\alpha}_n^i - \boldsymbol{\alpha}_n^{i-1}\|^2/K \leq \eta$ then
8:     Terminate iterations
9: else
10:     $i \leftarrow i + 1$
11:     Go back to 4.
12: end if
```

The unknown phase $\phi(f)$ of the spectral mask can be iteratively adjusted as described in [19]. First, its phase is chosen as $\phi(f) = 0$ and (3.15) is solved. The Fourier transform of designed pulse shape is computed and its phase is assigned to $\phi(f)$ and (3.15) is resolved. Iterations are terminated when the difference between the two consecutive solutions of (3.15) is below a certain threshold η. This method is summarized in Algorithm-2. In the next section, forming the dictionary $\mathbf{Q}(t)$ will be detailed.

3.5 Dictionary Design

To increase the dimension of the search space, the dictionary $\mathbf{Q}(t)$ should have as much linearly independent elements as possible. Since there are constraints on the pulse shape both in time and frequency, the waveforms in the dictionary $\mathbf{Q}(t)$ should be chosen accordingly. In [18, 19], time shifted Gaussian mono-pulses are used as the dictionary elements with the amount of time shifts $T = 1/(28GHz)$. For an allowed pulse duration T_p, in this approach the dictionary constructed as $\lceil T_p/T \rceil + 1$ time-shifted Gaussian mono-pulses[4]. In [21, 24, 25], HG functions are

---

[4] The operator $\lceil . \rceil$ returns the nearest integer larger than its argument.

used because of their optimal time-frequency localization characteristics. However, using high number of HG functions requires higher complexity in the transmitter/receiver structure. To avoid this, in this thesis, it is proposed to construct a dictionary from low order HG functions and their time-shifted versions.

To represent pulse shapes which have durations around one nanosecond, the dictionary elements should be properly scaled in time. Let $T_{h,n}$ and $B_{h,n}$ denote the effective time and frequency support of the n^{th} HG function, respectively, and B_w is the maximum allowed effective bandwidth for the dictionary elements. Since HG functions have circular support in the time-frequency plane [8], their effective time and frequency supports are equal, i.e., $T_{h,n} = B_{h,n}$. Assume that N_h HG functions of order $0, 1, .., N_h - 1$ are to be used for forming the dictionary. Each HG function could be scaled such that its effective bandwidth is set to B_w. However, this will complicate the hardware structure because it requires generation of Gaussian functions with different standard deviations. Rather than that, all of them are scaled with a fixed scaling factor $c = B_w/B_{h,N_h-1}$. Then, effective time and frequency support of each scaled HG function is given by $\tilde{T}_{h,n} = T_{h,n}/c$, $\tilde{B}_{h,n} = B_{h,n}c$. To represent the pulse shape with duration of $[0, T_p]$, the waveform dictionary is constructed by using time shifted, scaled HGs. The shifting amount is selected as integer multiples of $T = 1/(28GHz)$ as in [18]. For the n^{th} scaled HG function, the shifting amounts are given by $\{k^n_{min}T, (k^n_{min} + 1)T, .., k^n_{max}T\}$ where $k^n_{min} = \lfloor \tilde{T}_{h,n}/(2T) \rfloor$ and $k^n_{max} = \lceil (T_p - \tilde{T}_{h,n}/2)T) \rceil$. Hence the constructed dictionary is given by:

$$\begin{aligned}\bar{\mathbf{Q}}(t) = \quad & [\tilde{h}_0(t - k^0_{min}T), \tilde{h}_0(t - (k^0_{min} + 1)T), .., \tilde{h}_0(t - k^0_{max}T), \\ & \tilde{h}_1(t - k^1_{min}T), \tilde{h}_0(t - (k^1_{min} + 1)T), .., \tilde{h}_0(t - k^1_{max}T), \\ & ... \\ & \tilde{h}_{N_h-1}(t - k^{N_h-1}_{min}T), \tilde{h}_{N_h-1}(t - (k^{N_h-1}_{min} + 1)T), .., \tilde{h}_0(t - k^{N_h-1}_{max}T)].\end{aligned} \tag{3.16}$$

Since the constructed dictionary contains many waveforms, some of them could be linearly dependent. However, such a linearly dependent dictionary will generate different waveform combinations corresponding to the same pulse shape, hence it is not desired. To overcome this problem, we define a new dictionary

Algorithm 3 Dictionary Construction for Pulse Representation

```
Definitions:
Let $\bar{q}_m(t), m = 1, .., M$ denote the $m^{th}$ waveform of $\bar{\mathbf{Q}}(t)$
Let $\sigma_{min}$ and $\sigma_{max}$ be the minimum and maximum singular values of $\mathbf{A}$,
    respectively.
Initialization:
Construct $\bar{\mathbf{Q}}(t)$ in (3.16)
$\mathbf{Q}(t) = \bar{q}_1(t)$
$m = 2$
Iterations:
for $m = 2 : M$ do
    $\mathbf{A} = [\mathbf{Q}(t), \bar{q}_m(t)]$
    Compute sigular values of $\mathbf{A}$ and find $\sigma_{min}, \sigma_{max}$
    if $\sigma_{max}/\sigma_{min} \leq \varsigma$ then
        $\mathbf{Q}(t) = [\mathbf{Q}(t), \bar{q}_m(t)]$
    end if
end for
```

$\mathbf{Q}(t)$ and insert elements of $\bar{\mathbf{Q}}(t)$ one by one. In each insertion we compute the singular values of $\mathbf{Q}(t)$ and observe the ratio between the maximum and minimum valued singular values. If this ratio is larger than a predefined threshold ς, the last inserted waveform is discarded due to its larger than tolerable projection on to the subspace of previously chosen dictionary elements. This procedure is summarized in Algorithm-3. In the next section the structure of the transmitter and receiver will be discussed.

3.6 Proposed Transmitter/Receiver Structure

Since all the waveforms in the dictionary $\mathbf{Q}(t)$ are scaled HG functions with the same scale, shifted in time by integer multiples of $1/(28GHz)$ seconds and since each pulse is represented as a linear combination of the dictionary elements, the transmitter can be built based on the highly regular structure shown in Fig.3.2, where, N_h is the number of HG functions used, $\mathbf{Q}(t)$ is the constructed waveform dictionary provided by Algorithm-3, $\mathbf{\Psi}$ is the coefficient matrix, whose $n^{th}, n = 1, 2, .., N_p$ row corresponds to the optimized coefficients of the n^{th} pulse shape.

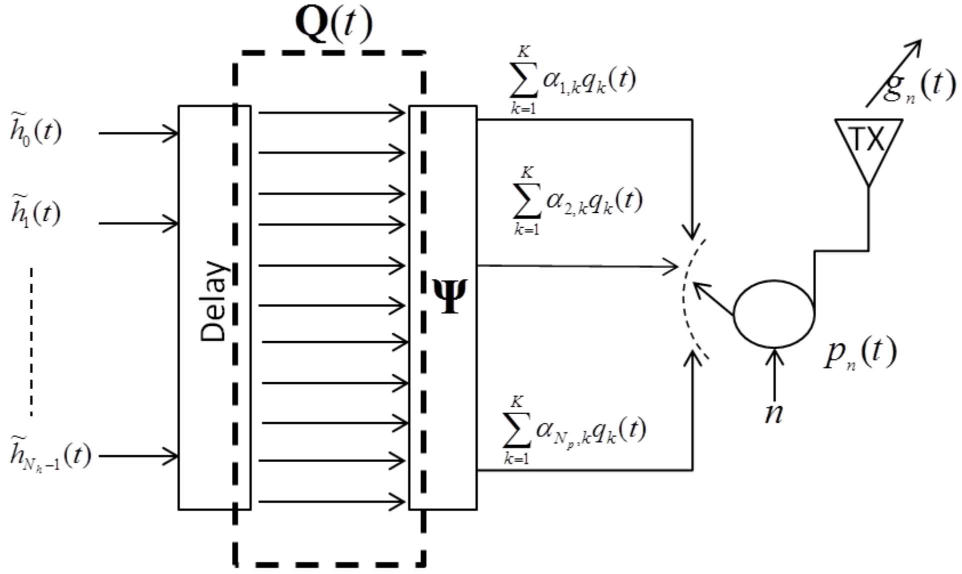

Figure 3.2: Proposed transmitter structure.

In the receiver side, the received waveform is correlated with N_p number of correlative functions, each of which corresponds to one pulse shape at the transmitter side, and the one which has the maximum correlation with the received waveform is decoded as the transmitted pulse shape. The correlating functions are $r_n(t),\ n = 1, .., N_p$ in (3.5), which are the second derivatives of the transmitted pulse shapes with certain gains. Hence, second derivatives of the HG functions that are in the dictionary should be generated at the receiver. Direct generations of derivatives of HGs having durations around one nanosecond would bring implementation difficulties. However, as shown in Apprendix-B, derivatives of HG functions can be represented as linear combinations of HGs as well. Specifically the following relations hold:

$$\begin{aligned}
h_0'(t) &= \beta_{0,1}h_1(t),\\
h_0''(t) &= \theta_{0,0}h_0(t) + \theta_{0,2}h_2(t),\\
h_1'(t) &= \beta_{1,0}h_0(t) + \beta_{1,2}h_2(t),\\
h_1''(t) &= \theta_{1,1}h_1(t) + \theta_{1,3}h_3(t),\\
h_n'(t) &= \beta_{n,n-1}h_{n-1}(t) + \beta_{n,n+1}h_{n+1}(t),\ \forall n \geq 2,\\
h_n''(t) &= \theta_{n,n-2}h_{n-2}(t) + \theta_{n,n}h_n(t) + \theta_{n,n+2}h_{n+2}(t),\ \forall n \geq 2.
\end{aligned} \tag{3.17}$$

Table 3.1: Representation coefficients of the first and second derivatives of the first four HG functions.

	$h_0'(t)$	$h_0''(t)$	$h_1'(t)$	$h_1''(t)$	$h_2'(t)$	$h_2''(t)$	$h_3'(t)$	$h_3''(t)$
$h_0(t)$	0	-3.141	1.772	0	0	4.443	0	0
$h_1(t)$	-1.772	0	0	-9.424	2.5066	0	0	7.695
$h_2(t)$	0	4.442	-2.506	0	0	-15.708	3.070	0
$h_3(t)$	0	0	0	7.695	-3.07	0	0	-21.991
$h_4(t)$	0	0	0	0	0	10.882	-3.544	0
$h_5(t)$	0	0	0	0	0	0	0	14.049

In Table-3.1, $\theta_{a,b}$ coefficients of the first and second derivative of the first 4 HG functions are provided. Hence the waveforms propagated through the transmitter antenna, $g_n(t)$, and at output of the receiver antenna, $r_n(t)$, can be represented as:

$$g_n(t) = \mathbf{Q}(t)\mathbf{\Pi}_1\boldsymbol{\alpha_n},\ n = 1, 2, .., N_p \tag{3.18}$$

$$r_n(t) = \mathbf{Q}(t)\mathbf{\Pi}_2\boldsymbol{\alpha_n},\ n = 1, 2, .., N_p \tag{3.19}$$

where $\mathbf{\Pi}_1$ and $\mathbf{\Pi}_2$ are the corresponding sparse matrices composed of $\theta_{a,b}$ coefficients that are used to represent derivatives of HGs in terms of HGs. Proposed simple receiver structure is given in Fig.3.3. In the next section, design examples will be provided.

3.7 Design Examples

In this section, results of the proposed pulse shape design procedure are provided for two different pulse durations $T_p = 0.55$ nanosecond, and $T_p = 0.88$ nanosecond. In both designs, the constructed optimization problems (3.10), (3.11), (3.15) are solved and the results are compared.

For the first pulse duration, 8 pulse shapes are designed by solving each constructed optimization problem. In Fig.3.4 and Fig.3.5, designed pulse shapes $p_n(t), n = 1, .., 8$ by solving (3.15) are shown. The power spectral densities of the transmitted pulse shapes $g_n(t), n = 1, .., 8$ together with the normalized spectral mask $M(f)$ are provided in Fig.3.6 and Fig.3.7. Results for solving (3.10)

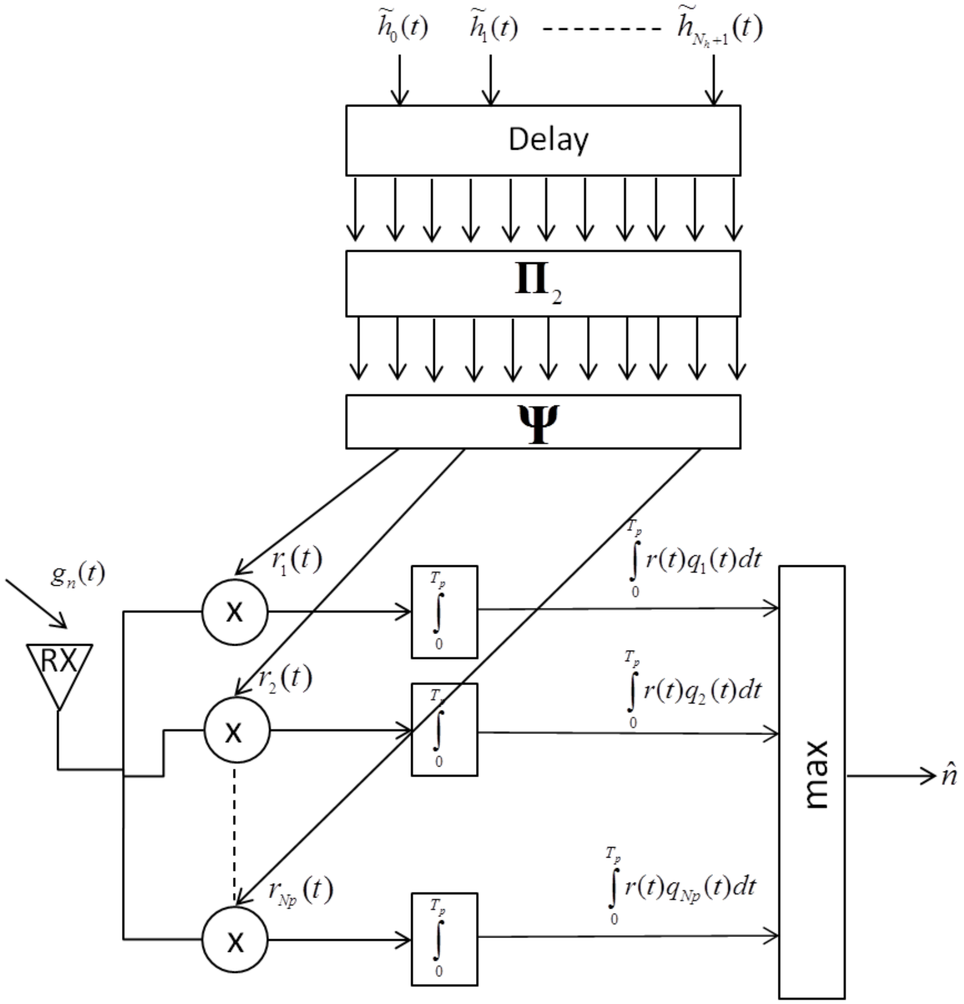

Figure 3.3: Proposed receiver structure.

and (3.11) are given in Fig.3.8 to Fig.3.11 and Fig.3.12 to Fig.3.15, respectively. For solving the non-convex problems in (3.10) and (3.11) MATLAB optimization toolbox [80], for solving the convex problem in (3.15) SeDuMi [79] is used .

To compare the performance of the three proposed approaches, we use the spectral utilization factor (SUF) defined as [18]:

$$SUF(n) = \frac{\int\limits_{F_p} |G_n(f)|^2 df}{\int\limits_{F_p} M(f) df}, \tag{3.20}$$

where $G_n(f)$ is the Fourier transform of n^{th} propagated pulse and F_p is the effective passband of the transmitted pulse shape, which is taken as $F_p = [0,\ 10.6]$GHz in this work. In Fig.3.16 and Fig.3.17, SUF of the designed pulse shapes for $T_p = 0.55$ns and $T_p = 0.88$ns durations, respectively, are given. As observed, optimization problems in (3.10) and (3.11) can design a larger set of orthogonal pulse shapes with higher SUF values compared to (3.15), since they are optimizing the coefficients of the all pulse shapes jointly.

3.8 Conclusions for Chapter 3

A new approach for designing high energy orthogonal UWB pulse shapes is proposed, in which orthogonality of the received pulses at the output of differentiating antennas are maintained. We model each pulse shape as a linear combination of time-shifted and scaled HG functions and construct three different optimization problems for designing high energy pulse shapes. By showing that derivative of each HG function can be represented as linear combination of other HGs, a simple receiver structure is achieved. Obtained results show that high energy orthogonal pulse shapes can be designed by using the proposed method.

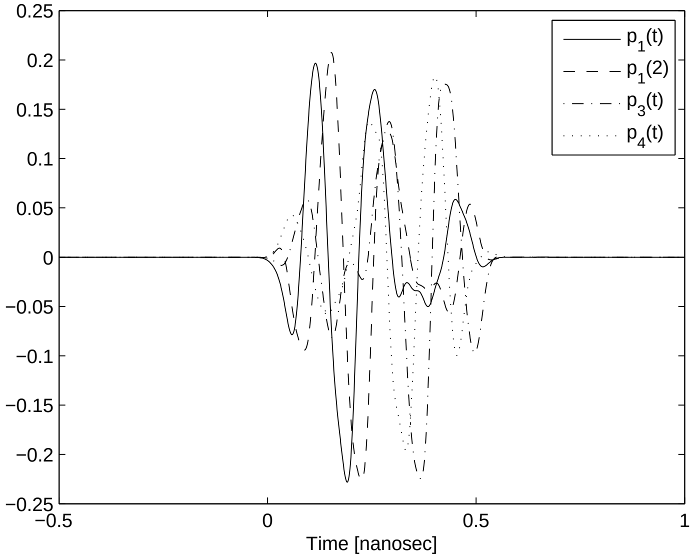

Figure 3.4: Designed pulse shapes $p_1(t)$ (solid), $p_2(t)$ (dashed), $p_3(t)$ (dashed-doted), $p_4(t)$ (doted) by solving the optimization problem (3.15) for pulse duration $T_p = 0.55$ nanosecond.

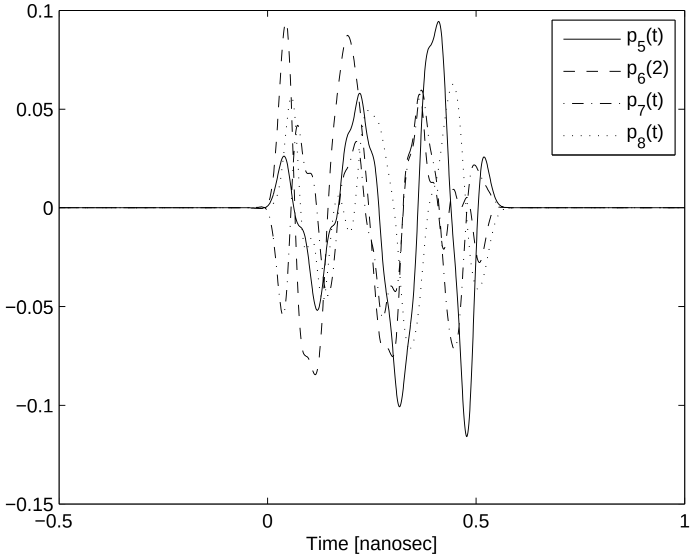

Figure 3.5: Designed pulse shapes $p_5(t)$ (solid), $p_6(t)$ (dashed), $p_7(t)$ (dashed-doted), $p_8(t)$ (doted) by solving the optimization problem (3.15) for pulse duration $T_p = 0.55$ nanosecond.

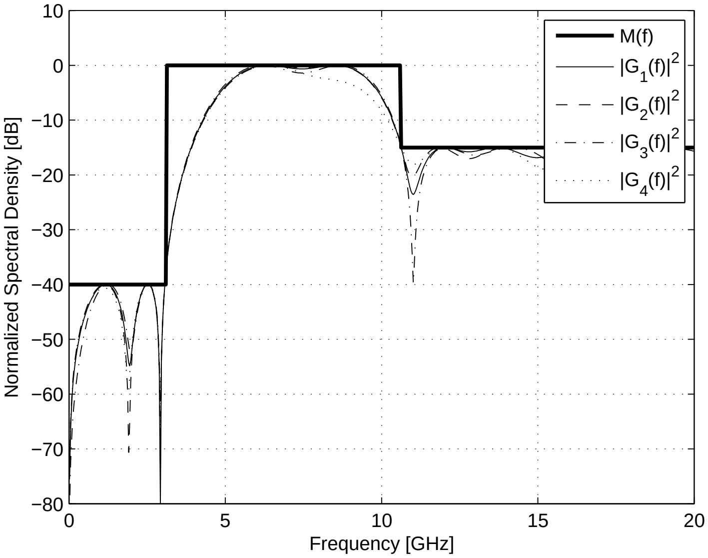

Figure 3.6: Power spectral densities of the transmitted pulse shapes $g_1(t)$ (solid), $g_2(t)$ (dashed), $g_3(t)$ (dashed-doted), $g_4(t)$ (doted) by solving the optimization problem (3.15) for pulse duration $T_p = 0.55$ nanosecond with the spectral mask $M(f)$.

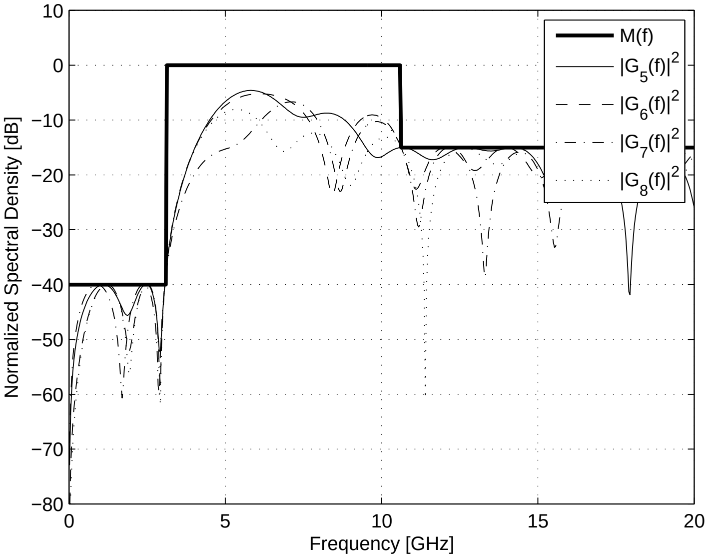

Figure 3.7: Power spectral densities of the transmitted pulse shapes $g_5(t)$ (solid), $g_6(t)$ (dashed), $g_7(t)$ (dashed-doted), $g_8(t)$ (doted) by solving the optimization problem (3.15) for pulse duration $T_p = 0.55$ nanosecond with the spectral mask $M(f)$.

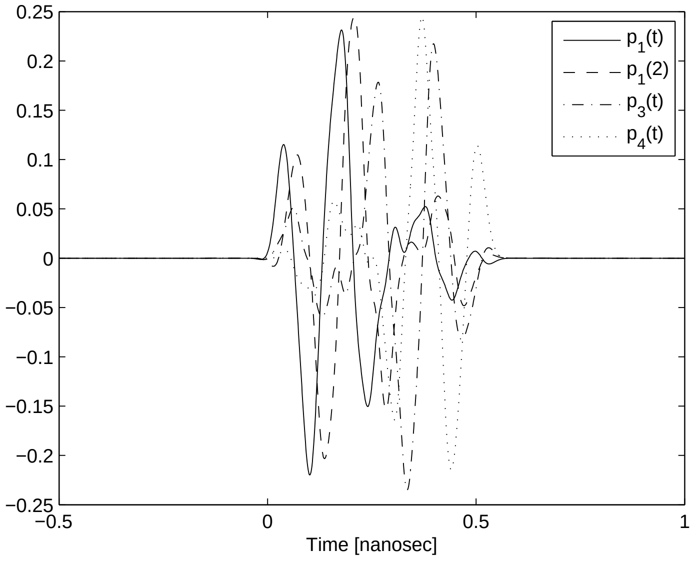

Figure 3.8: Designed pulse shapes $p_1(t)$ (solid), $p_2(t)$ (dashed), $p_3(t)$ (dashed-doted), $p_4(t)$ (doted) by solving the optimization problem (3.10) for pulse duration $T_p = 0.55$ nanosecond.

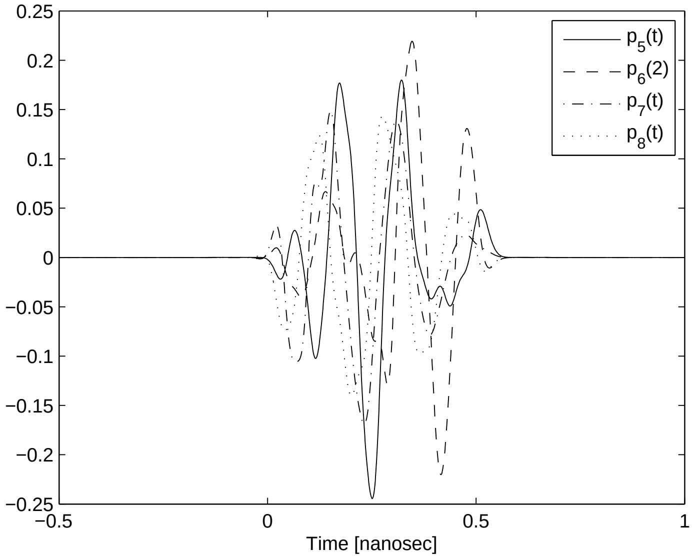

Figure 3.9: Designed pulse shapes $p_5(t)$ (solid), $p_6(t)$ (dashed), $p_7(t)$ (dashed-doted), $p_8(t)$ (doted) by solving the optimization problem (3.10) for pulse duration $T_p = 0.55$ nanosecond.

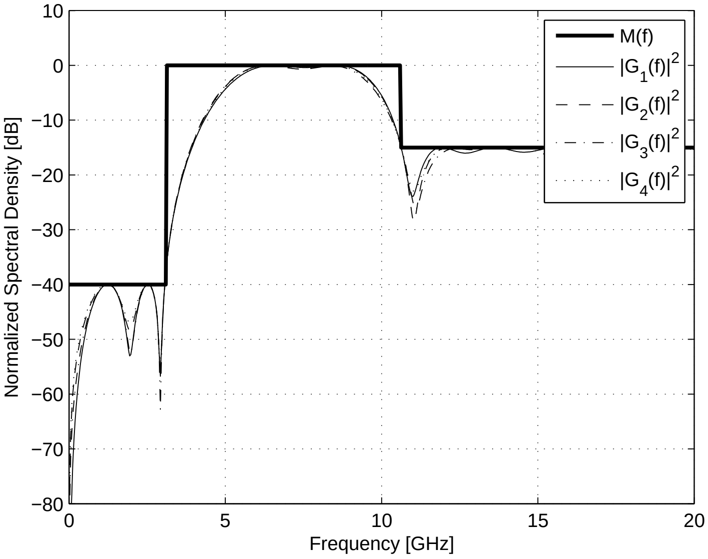

Figure 3.10: Power spectral densities of the transmitted pulse shapes $g_1(t)$ (solid), $g_2(t)$ (dashed), $g_3(t)$ (dashed-doted), $g_4(t)$ (doted) by solving the optimization problem (3.10) for pulse duration $T_p = 0.55$ nanosecond with the spectral mask $M(f)$.

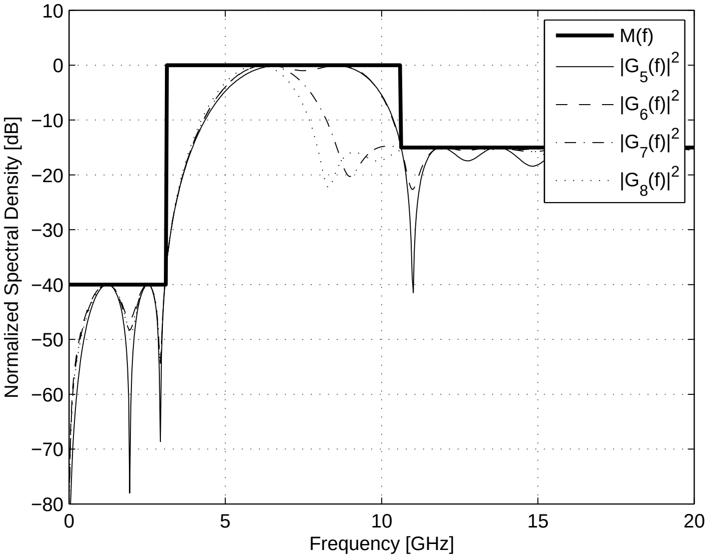

Figure 3.11: Power spectral densities of the transmitted pulse shapes $g_5(t)$ (solid), $g_6(t)$ (dashed), $g_7(t)$(dashed-doted), $g_8(t)$ (doted) by solving the optimization problem (3.10) for pulse duration $T_p = 0.55$ nanosecond with the spectral mask $M(f)$.

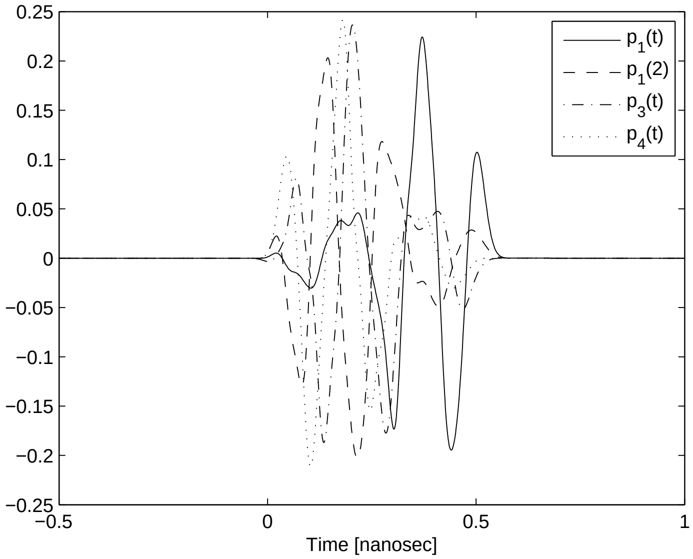

Figure 3.12: Designed pulse shapes $p_1(t)$ (solid), $p_2(t)$ (dashed), $p_3(t)$ (dashed-doted), $p_4(t)$ (doted) by solving the optimization problem (3.11) for pulse duration $T_p = 0.55$ nanosecond.

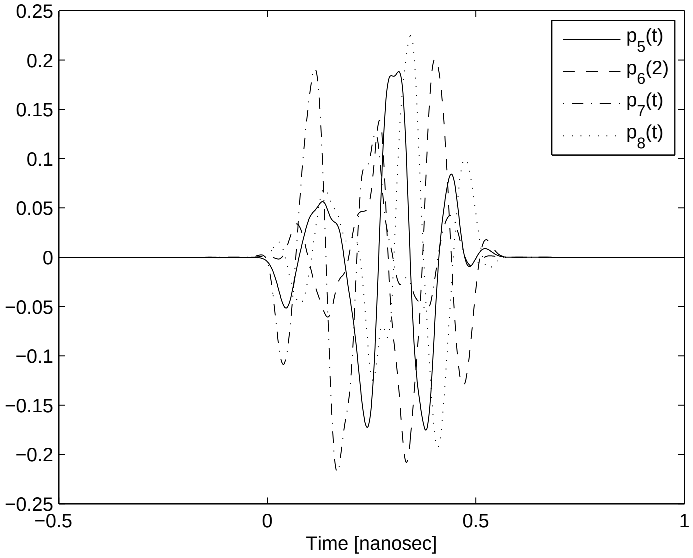

Figure 3.13: Designed pulse shapes $p_5(t)$ (solid), $p_6(t)$ (dashed), $p_7(t)$ (dashed-doted), $p_8(t)$(doted) by solving the optimization problem (3.11) for pulse duration $T_p = 0.55$ nanosecond.

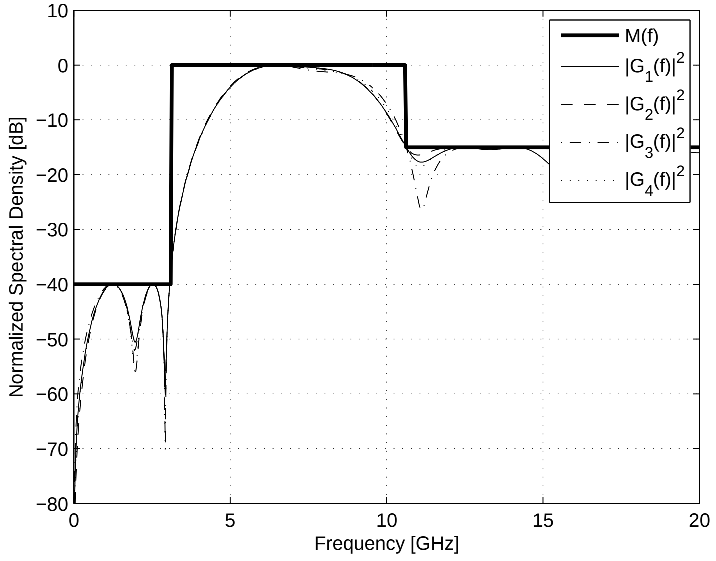

Figure 3.14: Power spectral densities of the transmitted pulse shapes $g_1(t)$ (solid), $g_2(t)$ (dashed), $g_3(t)$ (dashed-doted), $g_4(t)$(doted) by solving the optimization problem (3.11) for pulse duration $T_p = 0.55$ nanosecond with the spectral mask $M(f)$.

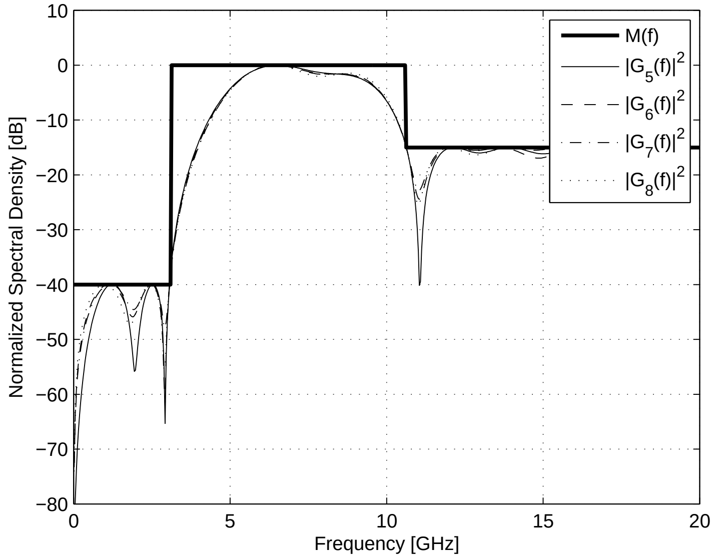

Figure 3.15: Power spectral densities of the transmitted pulse shapes $g_5(t)$ (solid), $g_6(t)$ (dashed), $g_7(t)$ (dashed-doted), $g_8(t)$ (doted) by solving the optimization problem (3.11) for pulse duration $T_p = 0.55$ nanosecond with the spectral mask $M(f)$.

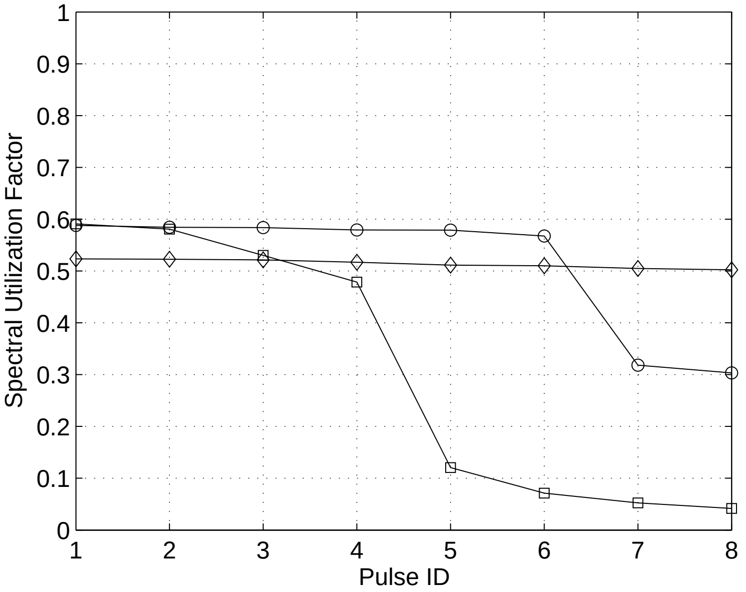

Figure 3.16: SUF of the designed pulse shapes by solving (3.10) (circle), (3.11) (diamond) and (3.15) (square) for pulse duration $T_p = 0.55$ nanosecond.

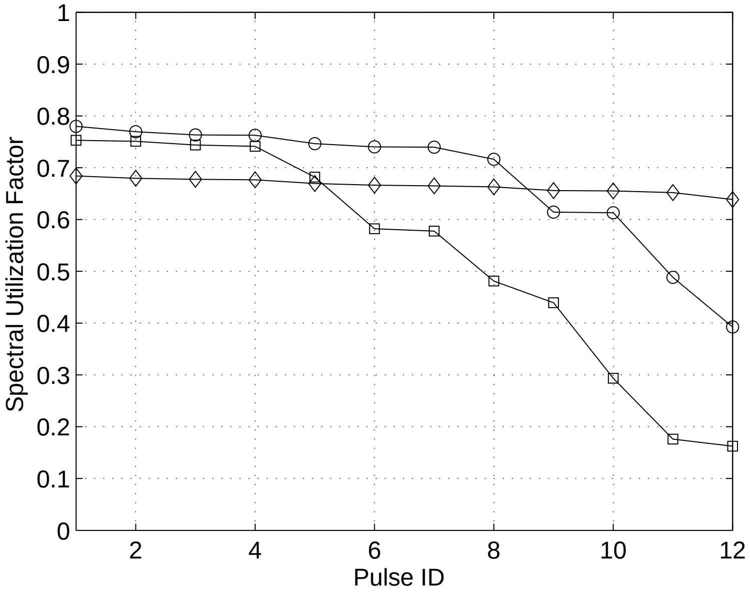

Figure 3.17: SUF of the designed pulse shapes by solving (3.10) (circle), (3.11) (diamond) and (3.15) (square) for pulse duration $T_p = 0.88$ nanosecond.

Chapter 4

Phase-Only Control of Array Antennas by Using Convex Programming

4.1 Introduction

Array antennas are used in many applications such as radar [28], sonar [29], communications [30], radio astronomy [31], seismology and tomography [32]. Operating frequency and spatial positions of the array elements define the main characteristics of antenna pattern. By applying different complex weights to the array elements, the beam pattern can be steered to directions of interest, sidelobe levels can be suppressed, mainlobe beam width can be reduced [33]. These complex element weights are implemented as amplitude controllers and phase shifters at the system level [81]. Because of cost constraints and hardware limitations, many systems do not have an individual amplitude controller for each array element. Hence, array beam pattern is typically controlled by only varying the element phases.

A synthesis method for generating multiple patterns from the same array antenna is proposed in [82], where a common amplitude distribution and individual phase for each target pattern are estimated. In [37, 38], particle swarm optimization and genetic algorithm are used to minimize a certain cost function of element phases for phase-only control of the beam pattern. Suppressing the beam pattern at some certain direction by only varying the element phases has been also widely investigated [34, 36, 35, 39]. Adaptive sidelobe nulling based on the autocorrelation function of the received signal is proposed in [34, 35]. However, proposed method can not be used for the transmit antenna case. A phase perturbation based method, where the non-linear phase-only nulling problem is linearised by assuming small phase perturbations is proposed in [36]. Since the phase variations are assumed to be small, there would be significant challenges in hardware implementations. Suppressing the beam power at a certain angle by adjusting the least significant bits of the phase shifter for minor deviations in the pattern at the steering direction by using genetic algorithm is proposed in [39]. However, since the cost function is non-convex, the optimality of the provided solution is not guaranteed.

In this work, unlike the previous approaches, a convex programming based method is proposed. First, an optimization problem corresponding to the physical problem is constructed. Then, a convex relaxation, which doesn't destroy the nature of the physical problem, is applied to obtain a convex optimization problem, which can be solved to obtain the global optimum point by utilizing an available convex solver. We define two specific problems related to phase-only control of beam pattern: 1) Phase-only beam synthesis for moderate size arrays; 2) Phase-only sidelobe suppression for large arrays. In the first problem, a set of element phases, for which the resulting beam pattern should satisfy the given "$\leq$", "$\geq$" constraints limiting the sidelobe and mainlobe power, are to be estimated. In the second problem, element phases are to be estimated to minimize the total radiation power of the resulting beam pattern at given directions, while satisfying the desired mainlobe power level. For both of the problems, first, a quadratically constrained quadratic problem (QCQP) is constructed to model the physical problem. Then, a convex semidefinite problem (SDP), which can be solved at the global optimum point in polynomial time, is obtained by relaxing the constructed QCQP. Although the resulting SDP is convex, its optimal solution is almost never a rank-1 matrix. For the first problem, to achieve a rank-1 solution, we propose a novel iterative rank refinement algorithm, where at each step an SDP with additional convex constraints are solved. We show that, after a few iterations, the optimal solution of the constructed SDP has very fast decaying singular values, converging to a rank-1 solution. Although the proposed method can be utilized for solving the second problem for moderate size arrays, it is not appropriate for large arrays having more than 100 elements since it requires solving a new SDP of dimension 10000 at each iteration. Convex solvers implementing interior point methods can not handle problems of this size on ordinary desktop computers. Hence, we propose an Alternating Direction Method of Multipliers (ADMM) based solution for the second problem. By utilizing ADMM, the constructed SDP is divided into smaller subproblems whose solutions are either analytically known or easy to compute. Moreover, as required, a rank-1 solution is obtained. Conducted experiments show that, the proposed ADMM based method for the second problem can provide desired solutions to large arrays having up to 500 elements by performing required computations on an ordinary desktop computer.

The organization of this chapter is as follows: In Section 4.2, a brief information on phased array antennas is provided. Phase-only beam synthesis problem and the proposed iterative rank refinement algorithm is given in Section 4.3. In Section 4.4, phase-only sidelobe suppression problem and the proposed ADMM based solution is discussed. Finally, concluding remarks are given in Section 4.5.

4.2 Phased Array Antennas

Let $\mathbf{p}_n,\ n = 1, ..., N$ denote the spatial positions of antenna elements, where $\mathbf{p}_n = [p_{n,x}, p_{n,y}, p_{n,z}]^T$. The beam pattern of the array is a two dimensional

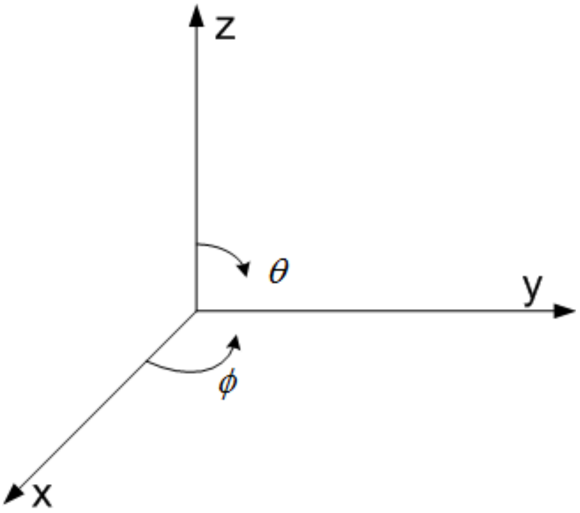

Figure 4.1: Definition of elevation (θ) and azimuth (ϕ) angles.

function defined as[1]:

$$B(\theta,\phi)=\sum_{n=1}^{N}\alpha_n v_n(\theta,\phi), \tag{4.1}$$

where α_n is the complex weight of the n^{th} element, θ and ϕ are elevation and azimuth angles defined in Fig.4.1, respectively. $v_n(\theta,\phi)$ is the manifold vector of the n^{th} antenna element given by:

$$v_n(\theta,\phi)=\exp\{j\frac{2\pi}{\lambda}\mathbf{p}_n^T\mathbf{a}\}. \tag{4.2}$$

Here λ is the operating wavelength and $\mathbf{a}=[\sin\theta\cos\phi,\ \ \sin\theta\sin\phi,\ \ \cos\theta]^T$ is the directional cosines. The power pattern, which defines the angular distribution of radiation, is computed as:

$$P(\theta,\phi)=|B(\theta,\phi)|^2. \tag{4.3}$$

To steer the antenna beam to the direction $(\bar{\theta},\bar{\phi})$, i.e., to set the direction of maximum radiation to $(\bar{\theta},\bar{\phi})$, the following optimization problem should be solved:

$$\begin{aligned}&\max_{\alpha_1,..,\alpha_N}\ P(\bar{\theta},\bar{\phi})\\ &\quad\text{s.t.}\ |\alpha_n|\leq 1,\ n=1,..,N,\end{aligned} \tag{4.4}$$

---

[1] Throughout this chapter, all the array elements are assumed to have omni directional radiation patterns.

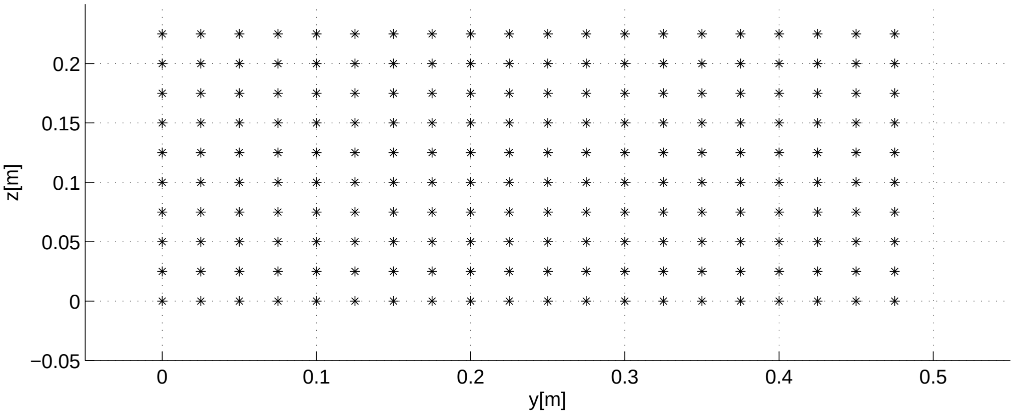

Figure 4.2: A 10 × 20 array geometry. Inter element spacings are chosen as $d_y = d_z = \lambda/2$. Operating frequency is 6 GHz.

where we assume that the amplitude controllers can set the radiation power of each element to any value in the interval [0, 1] Watt, without loss of generality. With this formulation, the radiation power at direction $(\bar{\theta}, \bar{\phi})$ is to be maximized by varying the element weights. The optimization problem in (4.4) has the following closed form solution:

$$\alpha_n = v_n(\bar{\theta}, \bar{\phi})^*, \; n = 1, .., N. \tag{4.5}$$

For the array geometry shown in Fig.4.2, at 6 GHz, the normalized power pattern[2] of the antenna, when the antenna beam is steered to $(\bar{\theta} = 90^o, \bar{\phi} = 0^o)$ and $(\bar{\theta} = 90^o, \bar{\phi} = 45^o)$ is given in Fig.4.3 and Fig.4.4. In Fig.4.5, elevation $\theta = 90^o$ cut of the Fig.4.3 and Fig.4.4 are shown in blue and red, respectively. As observed, by changing the element phases, array beam can be steered to desired direction. However, as discussed above, controlling the sidelobe levels of the beam pattern by only varying the element phases is not straight forward. In the following two sections, two problems discussing this issue, together with proposed solutions will be investigated.

---

[2] By normalization, we mean that the maximum radiation power of the antenna at the steering direction is set to 0 dB Watt.

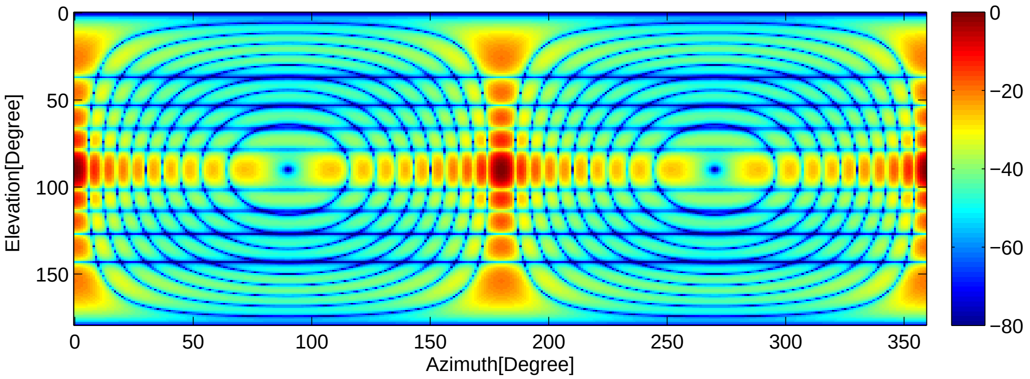

Figure 4.3: Normalized power pattern of the antenna array shown in Fig.4.2 operating at 6 GHz, when the array beam is steered to ($\bar{\theta} = 90^o, \bar{\phi} = 0^o$).

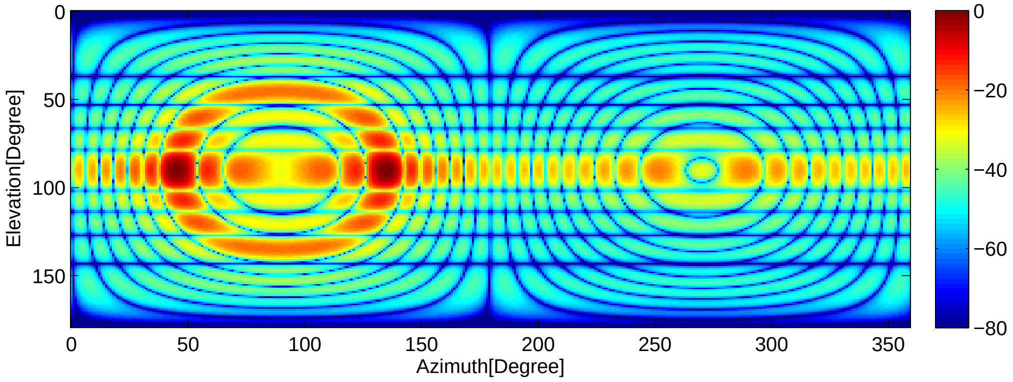

Figure 4.4: Normalized power pattern of the antenna array shown in Fig.4.2 operating at 6 GHz, when the array beam is steered to ($\bar{\theta} = 90^o, \bar{\phi} = 45^o$).

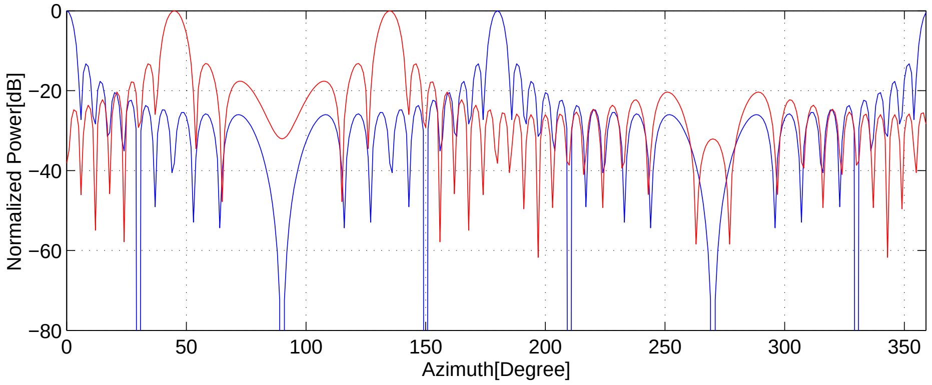

Figure 4.5: Elevation $\theta = 90^o$ cut of the power patterns given in Fig.4.3 and Fig.4.4 for steering direction ($\bar{\theta} = 90^o, \bar{\phi} = 0^o$) (blue) and ($\bar{\theta} = 90^o, \bar{\phi} = 45^o$) (red).

4.3 Phase-Only Beam Synthesis Problem

4.3.1 Problem Definition

We define the phase-only beam synthesis problem as follows: While keeping the mainlobe power above a given required level, find the phases of each element so that the sidelobe power in a set of given directions are restricted to be less than a given threshold. Hence, the following optimization problem can be constructed:

$$\begin{aligned}
&\text{find } \alpha_1, ..., \alpha_N \\
&\text{s.t. } |B(\bar{\theta}, \bar{\phi})|^2 \geq \delta, \\
&\quad |B(\theta_{s_k}, \phi_{s_k})|^2 \leq \delta_s,\ k = 1, .., K, \\
&\quad |\alpha_n|^2 = 1,\ n = 1, .., N, \\
&\quad |B(\bar{\theta}, \bar{\phi})|^2 > |B(\theta_{m_h}, \phi_{m_h})|^2,\ h = 1, .., H.
\end{aligned} \tag{4.6}$$

Here, $(\bar{\theta}, \bar{\phi})$ is the steering direction and δ is the allowed minimum power level in that direction, and $(\theta_{s_k}, \phi_{s_k}), k = 1, .., K$ are the sidelobe directions for which the maximum allowed power level is δ_s. Without loss of generality, we assume that all the elements operate at a power level of 1 Watt. The last constraint is to localize the direction of maximum radiation in the steering direction. Here, $(\theta_{m_h}, \phi_{m_h})$ are the directions around $(\bar{\theta}, \bar{\phi})$. This constraint is critical especially in direction finding applications. In Fig.4.6, these constraints are illustrated for a $N = 21$ element linear array.

The feasible set of (4.6) might be empty because of the constraints $|\alpha_n|^2 = 1$ constraints could be too strict. Hence, first we define the following relaxed

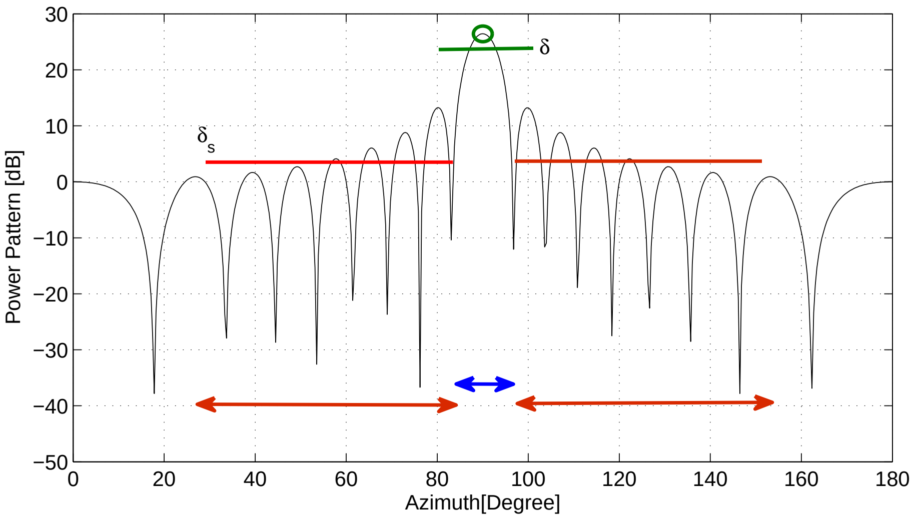

Figure 4.6: Illustration of the constraints in (4.6). Green ellipse indicate the steering direction. Green line is the mainlobe power level constraint δ. Red line is the threshold δ_s for sidelobe constraints. Green and red arrows indicate the mainlobe and sidelobe constraint directions $(\theta_{m_h}, \phi_{m_h}), h = 1, .., H$ and $(\theta_{s_k}, \phi_{s_k}), k = 1, .., K$, respectively.

problem, whose feasible set contains the feasible set of (4.6)[3]:

$$\begin{aligned} \max_{\boldsymbol{\alpha}\in\mathbb{C}^N} \ & \|\boldsymbol{\alpha}\|^2 \\ \text{s.t.} \ & |\boldsymbol{\alpha}^T\bar{\mathbf{v}}|^2 \geq \delta, \\ & |\boldsymbol{\alpha}^T\mathbf{v}_{s_k}|^2 \leq \delta_s, \ k = 1, ..., K, \\ & |\alpha_n|^2 \leq 1, \ n = 1, ..., N, \\ & |\boldsymbol{\alpha}^T\bar{\mathbf{v}}|^2 > |\boldsymbol{\alpha}^T\mathbf{v}_{m_h}|^2, \ h = 1, ..., H, \end{aligned} \tag{4.7}$$

where $\bar{\mathbf{v}} = [v_1(\bar{\theta}, \bar{\phi}), .., v_N(\bar{\theta}, \bar{\phi})]^T$, $\mathbf{v}_{s_k} = [v_1(\theta_{s_k}, \phi_{s_k}), .., v_N(\theta_{s_k}, \phi_{s_k})]^T$, $\mathbf{v}_{m_h} = [v_1(\theta_{m_h}, \phi_{m_h}), .., v_N(\theta_{m_h}, \phi_{m_h})]^T$, and $\boldsymbol{\alpha} = [\alpha_1, .., \alpha_N]^T$. In this formulation, total radiated power is to be maximized, sidelobe and mainlobe constraints of (4.6) are preserved and equality constraints on the antenna weights are replaced with inequality constraints. Hence, the feasible set of (4.7) is guaranteed to be nonempty for reasonable choices of δ and δ_s. If the feasibility problem in (4.6) has a solution, then it would also be an optimal solution for (4.7).

---

[3] All the norms defined as $\|.\|$ in this chapter indicate l_2 norm unless otherwise is stated.

The optimization problem in (4.7) has dimension N, where the optimization variables are complex numbers. It can equivalently be formulated as a $2N$ dimensional optimization problems in real variables:

$$\begin{aligned} \min_{\boldsymbol{\beta}\in\mathbb{R}^{2N}} \quad & -\boldsymbol{\beta}^T\boldsymbol{\beta} \\ \text{s.t.} \quad & \boldsymbol{\beta}^T\bar{\mathbf{V}}\bar{\mathbf{V}}^T\boldsymbol{\beta} \geq \delta, \\ & \boldsymbol{\beta}^T\mathbf{V}_{s_k}\mathbf{V}_{s_k}^T\boldsymbol{\beta} \leq \delta_s, \; k = 1, ..., K, \\ & \boldsymbol{\beta}^T\mathbf{W}_n^T\mathbf{W}_n\boldsymbol{\beta} \leq 1, \; n = 1, ..., N, \\ & \boldsymbol{\beta}^T\left(\bar{\mathbf{V}}\bar{\mathbf{V}}^T - \mathbf{V}_{m_h}\mathbf{V}_{m_h}^T\right)\boldsymbol{\beta} \geq \epsilon, \; h = 1, ..., H, \end{aligned} \tag{4.8}$$

where $\boldsymbol{\beta} = \begin{bmatrix} \Re\{\boldsymbol{\alpha}\} \\ \Im\{\boldsymbol{\alpha}\} \end{bmatrix}$, $\bar{\mathbf{V}} = \begin{bmatrix} \Re\{\bar{\mathbf{v}}^T\}, & -\Im\{\bar{\mathbf{v}}^T\} \\ \Im\{\bar{\mathbf{v}}^T\}, & \Re\{\bar{\mathbf{v}}^T\} \end{bmatrix}$, $\mathbf{V}_{s_k} = \begin{bmatrix} \Re\{\mathbf{v}_{s_k}^T\}, & -\Im\{\mathbf{v}_{s_k}^T\} \\ \Im\{\mathbf{v}_{s_k}^T\}, & \Re\{\mathbf{v}_{s_k}^T\} \end{bmatrix}$, $\mathbf{V}_{m_h} = \begin{bmatrix} \Re\{\mathbf{v}_{m_h}^T\}, & -\Im\{\mathbf{v}_{m_h}^T\} \\ \Im\{\mathbf{v}_{m_h}^T\}, & \Re\{\mathbf{v}_{m_h}^T\} \end{bmatrix}$, $\mathbf{W}_n$ is an $2 \times 2N$ matrix composed of all zeros except $\mathbf{W}_n(1, n) = 1$ and $\mathbf{W}_n(2, N+n) = 1$, and ϵ is a positive number very close to zero. The operators $\Re\{.\}$ and $\Im\{.\}$ return the real and imaginary parts of their arguments, respectively. Note that the maximization in (4.7) is converted to a minimization in (4.8). For notational simplicity, we further define the following matrices $\mathbf{A} = \bar{\mathbf{V}}\bar{\mathbf{V}}^T$, $\mathbf{B}_k = \mathbf{V}_{s_k}\mathbf{V}_{s_k}^T$, $\mathbf{C}_n = \mathbf{W}_n^T\mathbf{W}_n$, $\mathbf{D}_h = \bar{\mathbf{V}}\bar{\mathbf{V}}^T - \mathbf{V}_{m_h}\mathbf{V}_{m_h}^T$ and rewrite (4.8) as the following QCQP:

$$\begin{aligned} \min_{\boldsymbol{\beta}\in\mathbb{R}^{2N}} \quad & -\boldsymbol{\beta}^T\boldsymbol{\beta} \\ \text{s.t.} \quad & \boldsymbol{\beta}^T\mathbf{A}\boldsymbol{\beta} \geq \delta, \\ & \boldsymbol{\beta}^T\mathbf{B}_k\boldsymbol{\beta} \leq \delta_s, \; k = 1, ..., K, \\ & \boldsymbol{\beta}^T\mathbf{C}_n\boldsymbol{\beta} \leq 1, \; n = 1, ..., N, \\ & \boldsymbol{\beta}^T\mathbf{D}_h\boldsymbol{\beta} \geq \epsilon, \; h = 1, ..., H. \end{aligned} \tag{4.9}$$

Since the QCQP in (4.9) has non-convex cost function and constraints, its global optimizer might not be obtained in polynomial time [83]. In the next section, proposed iterative rank refinement algorithm for solving the non-convex optimization problem in (4.9) will be detailed.

4.3.2 Proposed Iterative Rank Refinement Algorithm

Constructed QCQP in (4.9) can be equivalently written as an SDP:

$$\begin{aligned}
\min_{\mathbf{\Lambda}\in\mathbb{R}^{2N\times 2N}} \quad & Tr\{-\mathbf{\Lambda}\} \\
\text{s.t.} \quad & Tr\{\mathbf{A}\mathbf{\Lambda}\} \geq \delta, \\
& Tr\{\mathbf{B}_k\mathbf{\Lambda}\} \leq \delta_s, \ k=1,...,K, \\
& Tr\{\mathbf{C}_n\mathbf{\Lambda}\} \leq 1, \ n=1,...,N, \\
& Tr\{\mathbf{D}_h\mathbf{\Lambda}\} \geq \epsilon, \ h=1,...,H, \\
& \mathbf{\Lambda} \succeq 0, \\
& \text{rank}(\mathbf{\Lambda}) = 1.
\end{aligned} \tag{4.10}$$

Note that optimization variable of this SDP is a matrix $\mathbf{\Lambda}\in\mathbb{R}^{2N\times 2N}$. By increasing the problem dimension from $2N$ to $4N^2$, all the quadratic constraints in (4.9) are handled as linear constraints in this formulation. If $\boldsymbol{\beta}_{opt}$ is an optimal solution for (4.9), then the matrix $\boldsymbol{\beta}_{opt}{\boldsymbol{\beta}_{opt}}^T$ is an optimal solution for (4.10). However, (4.10) is still an NP hard problem because of the rank constraint. By removing the rank constraint, it can be relaxed to a convex SDP, which can be solved to obtain the global optimum point in polynomial time [84]:

$$\begin{aligned}
\min_{\mathbf{\Lambda}\in\mathbb{R}^{2N\times 2N}} \quad & Tr\{-\mathbf{\Lambda}\} \\
\text{s.t.} \quad & Tr\{\mathbf{A}\mathbf{\Lambda}\} \geq \delta_m, \\
& Tr\{\mathbf{B}_k\mathbf{\Lambda}\} \leq \delta_s, \ k=1,...,K, \\
& Tr\{\mathbf{C}_n\mathbf{\Lambda}\} \leq 1, \ n=1,...,N, \\
& Tr\{\mathbf{D}_h\mathbf{\Lambda}\} \geq \epsilon, \ h=1,...,H, \\
& \mathbf{\Lambda} \succeq 0.
\end{aligned} \tag{4.11}$$

There are many convex solvers, such as CVX [85], SeDuMi [79], SDPT3 [86], which can be used for solving (4.11). However, optimal solution $\mathbf{\Lambda}_{opt}$ of (4.11) is not rank-1 in general, since convex solvers implementing interior point methods almost never provide rank-1 solutions for SDPs [84]. The rank-1 approximation of $\mathbf{\Lambda}_{opt}$, which minimizes $\|\mathbf{\Lambda}_{opt} - \tilde{\mathbf{\Lambda}}_{opt}\|_F^2$, can be formed as[4]:

$$\tilde{\mathbf{\Lambda}}_{opt} = \sigma_1 \mathbf{u}_1 \mathbf{u}_1^T, \tag{4.12}$$

where σ_1 is the largest singular value of $\mathbf{\Lambda}_{opt}$ and $\mathbf{u}_1$ is the corresponding left singular vector. Then, a candidate solution for the QCQP in (4.9) can be constructed as

$$\tilde{\boldsymbol{\beta}} = \sqrt{\sigma_1}\mathbf{u}_1. \tag{4.13}$$

However, since $\mathbf{\Lambda}_{opt}$ is not rank-1, $\tilde{\boldsymbol{\beta}}$ can be an infeasible point or a very distant point to the optimal solution of (4.9). Moreover, the convex semidefinite relaxation in (4.11) can not be forced to have a strictly rank-1 solution, since (4.9) and its equivalent formulation (4.10) are NP hard. However, it can iteratively be forced to have a solution matrix with fast decaying singular values, approximating to a rank-1 solution. Assume $\sigma_1^i \geq \sigma_2^i \geq ... \geq \sigma_{2N}^i$ are the singular values and $\mathbf{u}_1^i, \mathbf{u}_2^i, ..., \mathbf{u}_{2N}^i$ are the corresponding left singular vectors of $\mathbf{\Lambda}_{opt}^i$, where $\mathbf{\Lambda}_{opt}^i$ is the obtained optimal solution of (4.11) at the i^{th} iteration of the proposed method. Then, the following $2N-1$ convex quadratic constraints

$$(\mathbf{u}_k^i)^T \mathbf{\Lambda} (\mathbf{u}_k^i) \leq \zeta^i \frac{1}{2N} \sum_{n=1}^{2N} \sigma_n^i, \ k = 2, ..., 2N \tag{4.14}$$

are attached to (4.11) and it is resolved. Here, ζ^i is a predefined multiplier, which we initially choose as $\zeta^i = 1$. If the objective value $-Tr\{\mathbf{\Lambda}_{opt}^{i+1}\}$ is less than a target objective value O_t, then the multiplier at iteration $i+1$ is updated as $\zeta^{i+1} \leftarrow \mu\zeta^i$, where $0 < \mu < 1$ is the parameter controlling the convergence rate of the algorithm. After finite number of iterations N_{iter} or the difference between energy ratio of highest singular value of $\mathbf{\Lambda}_{opt}^i$ between two consecutive iterations, i.e.,

$$r(i) = \left| \frac{\sigma_1^i}{\sum\limits_{n=1}^{2N} \sigma_n^i} - \frac{\sigma_1^{i-1}}{\sum\limits_{n=1}^{2N} \sigma_n^{i-1}} \right| \tag{4.15}$$

---

[4] $\|.\|_F$ indicates the Frobenius norm of its argument.

is smaller than a certain threshold ν, iterations are terminated and the final solution of (4.9) is obtained as:

$$\tilde{\boldsymbol{\beta}}^{i} = \sqrt{\sigma_1^i}\mathbf{u}_1^i. \tag{4.16}$$

Then, the corresponding complex antenna weight vector can be formed as:

$$\tilde{\boldsymbol{\alpha}}^{i} = \hat{\mathbf{W}}\tilde{\boldsymbol{\beta}}^{i}, \tag{4.17}$$

where $\hat{\mathbf{W}}$ is an $N \times 2N$ matrix composed of zeros except $\hat{\mathbf{W}}(n,n) = 1, \hat{\mathbf{W}}(n, N+n) = j,$ for $n = 1, .., N$. If the value of the cost function in (4.9) evaluated at the optimal solution $\boldsymbol{\Lambda}_{opt}^{i}$ at the final iteration is greater than $-N$, then the complex antenna weights $\tilde{\alpha}_n^i, n = 1, .., N$, do not satisfy the power constraint in (4.4). Therefore, weights should be normalized as:

$$\hat{\alpha}_n^i = \tilde{\alpha}_n^i / |\tilde{\alpha}_n^i|, \ n = 1, ..., N. \tag{4.18}$$

In Algorithm-4, steps of the proposed optimization algorithm are summarized. In the next section experimental results demonstrating the performance of the proposed iterative rank refinement algorithm will be provided.

4.3.3 Experimental Results

To investigate the performance of the proposed method, a uniform linear array with $N = 21$ elements shown in Fig.4.7 is used. Inter element spacing is set to $d = 0.4\lambda$, where λ is the wavelength. The operating frequency is $f = 2$ GHz. As design constraints, we allow 5 dB power reduction in the steering direction ($\delta = 10 \log N^2 - 5$ dB) and require 23 dB sidelobe suppression ($\delta_s = 10 \log N^2 - 23$ dB). The beamwidth measured at 23 dB below the maximum power level ($10 \log N^2$) around the steering direction is constrained to be less than 15 degree in azimuth. All the antenna elements are required to operate at 1 Watt. The proposed method in Algorithm-4 is initialized with parameters $N_{iter} = 20$, $\nu = 0.01$ for steering direction of $\bar{\phi} = 90^o$ in azimuth and $\bar{\theta} = 0^o$ in elevation. For solving the SDP in (4.11), CVX is used [85].

Algorithm 4 Iterative semidefinite relaxations with rank refinement:

```
**Initialization:**
$i = 0$.
$\zeta^i = 1$.
$r(i) = 1$.
Find $\mathbf{\Lambda}_{opt}^i$ by solving (4.11).
Apply SVD to $\mathbf{\Lambda}_{opt}^i$ and find its singular values $\sigma_1^i \geq \sigma_2^i \geq .. \geq \sigma_{2N}^i$ and the corresponding left singular vectors $\mathbf{u}_1^i, \mathbf{u}_2^i, .., \mathbf{u}_{2N}^i$.
$\tilde{\boldsymbol{\beta}}^i = \sqrt{\sigma_1^i}\mathbf{u}_1^i$.
Compute $r(i)$ by using (4.15).
**Iterations:**
**while** $i \leq N_{iter}$ and $r(i) \geq \nu$ **do**
    Attach $(\mathbf{u}_k^i)^T \mathbf{\Lambda}(\mathbf{u}_k^i) \leq \zeta^i \frac{1}{2N}\sum_{n=1}^{2N} \sigma_n^i \ \forall k = 2, 3, .., 2N$ constraints to (4.11) and resolve it for finding $\mathbf{\Lambda}_{opt}^{i+1}$.
    Apply SVD to $\mathbf{\Lambda}_{opt}^{i+1}$ and find its singular values $\sigma_1^{i+1} \geq \sigma_2^{i+1} \geq .. \geq \sigma_{2N}^{i+1}$ and the corresponding left singular vectors $\mathbf{u}_1^{i+1}, \mathbf{u}_2^{i+1}, .., \mathbf{u}_{2N}^{i+1}$.
    $\tilde{\boldsymbol{\beta}}^{i+1} = \sqrt{\sigma_1^{i+1}}\mathbf{u}_1^{i+1}$.
    Compute $r(i+1)$ by using (4.15).
    **if** $Tr\{-\mathbf{\Lambda}_{opt}^{i+1}\} \leq O_t$ **then**
        $\zeta^{i+1} \leftarrow \mu\zeta^i$.
    **end if**
    $i \leftarrow i + 1$
**end while**
Form complex weights: $\tilde{\boldsymbol{\alpha}}^i = \hat{\mathbf{W}}\tilde{\boldsymbol{\beta}}^i$
Normalize complex weights: $\hat{\alpha}_n^i = \tilde{\alpha}_n^i / |\tilde{\alpha}_n^i|, n = 1, ..., N$.
```

After the first iteration, optimal value of the SDP in (4.11) is found to be -21. However, since the provided solution is not rank-1, the total power of the antenna elements is $\|\tilde{\boldsymbol{\alpha}}^1\|^2 = 8$, much smaller than 21. Hence the normalized coefficients $\hat{\boldsymbol{\alpha}}^1$ are quite different from the computed ones $\tilde{\boldsymbol{\alpha}}^1$. In Fig.4.8, elevation $\theta = 0^o$ cut of the power pattern generated for the normalized complex weight vector after the first ($\hat{\boldsymbol{\alpha}}^1$) is plotted (black). As observed, resulting beam pattern does not satisfy the design constraints. After 20 iterations, still the optimal value of the SDP in (4.11) is computed to be -21, the optimal solution matrix $\mathbf{\Lambda}_{opt}^{20}$ is nearly rank-1 and the total power of the antenna elements is $\|\tilde{\boldsymbol{\alpha}}^{20}\|^2 = 20.88$. Hence the normalized coefficients $\hat{\boldsymbol{\alpha}}^{20}$ are almost equal to $\tilde{\boldsymbol{\alpha}}^{20}$. The resulting pattern after iteration 20 is also plotted in Fig.4.8 (blue). As observed, all the design constraints are well satisfied.

In Fig.4.9, the ratio of the largest singular value of the optimal solution matrix $\mathbf{\Lambda}_{opt}^{i}$ of (4.11) to the sum of all its singular values as a function of iteration number i, i.e., $\sigma_1^i / \sum_{n=1}^{N} \sigma_n^i$, is plotted. As observed, at iteration $i = 20$, the solution matrix $\mathbf{\Lambda}^i$ is nearly rank one, since the largest singular value occupies most of its energy. Note that, as the iteration number increases, this ratio increases, demonstrating the converge behaviour of the proposed method. In Fig.4.10, 10 largest singular values of $\mathbf{\Lambda}_{opt}^{i}$ at iteration $i = 1$, $i = 3$, $i = 20$ are plotted. In the first iteration, singular values $\mathbf{\Lambda}_{opt}^{1}$ have a small decay rate. After iteration 3, singular values have a faster decay. At iteration 20, most of the energy is accumulated in the first singular value and the remaining ones are very close to 0, hence, effectively a rank-1 solution to (4.11) is obtained.

For different steering directions ($\bar{\theta} = 0^o$, $\bar{\phi} = 125^o$) and ($\bar{\theta} = 0^o$, $\bar{\phi} = 45^o$), same experiment is repeated. The resulting patterns after iteration $i = 1$ (black) and $i = 20$ (blue) are shown in Fig.4.11 and Fig.4.12, respectively. As observed, proposed method can find a set of phase values, for which the resulting pattern satisfies the given constraints in the set of given steering directions.

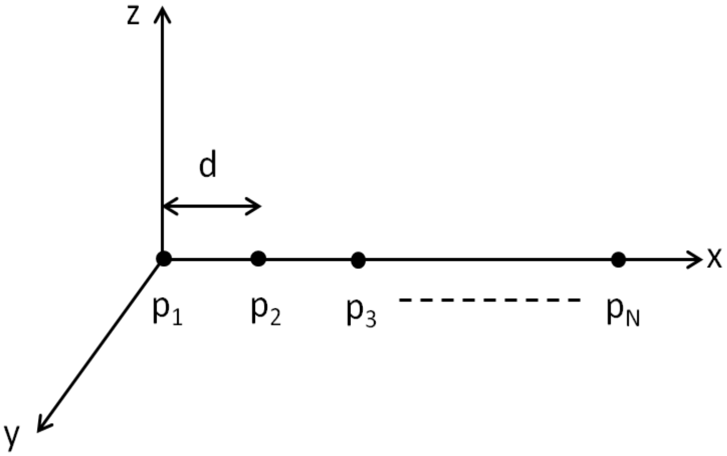

Figure 4.7: Uniform linear array with $N = 21$ elements. Inter element spacing is $d = 0.4\lambda$.

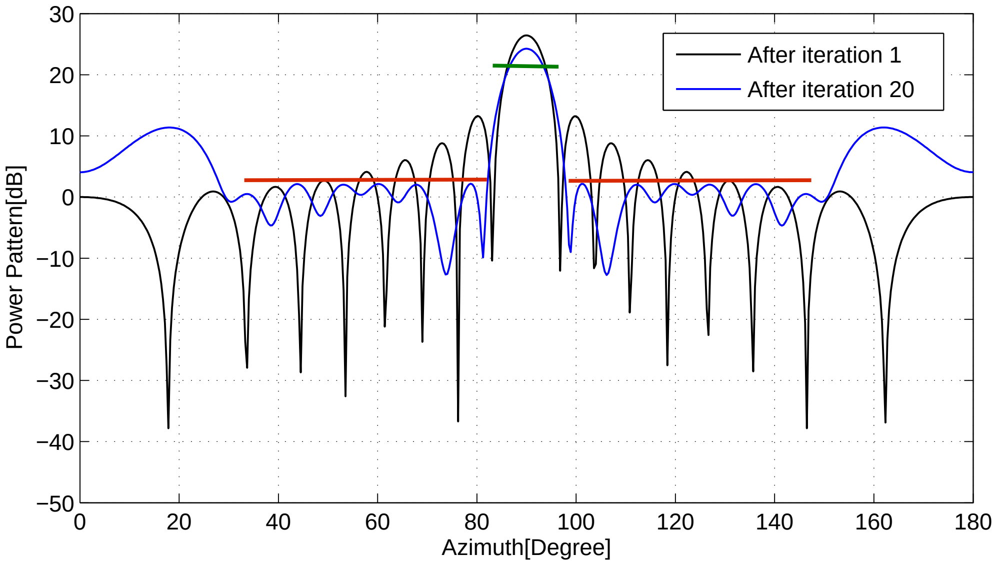

Figure 4.8: Elevation $\theta = 0^o$ cut of the power pattern for steering direction $(\bar{\theta} = 0^o, \bar{\phi} = 90^o)$ computed using the weights found at iteration $i = 1$ (black) and $i = 20$ (blue), respectively. Red lines indicate the sidelobe power level δ_s and green line indicates the main lobe power level δ.

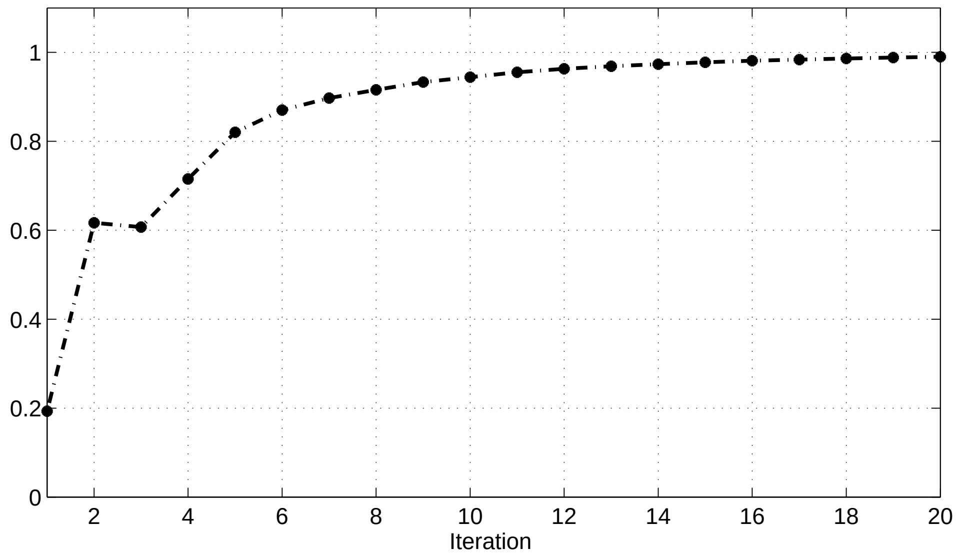

Figure 4.9: Ratio of the largest singular value of the optimal solution matrix $\mathbf{\Lambda}^i_{opt}$ of (4.11) to the sum of all its singular values as a function of iteration number i.

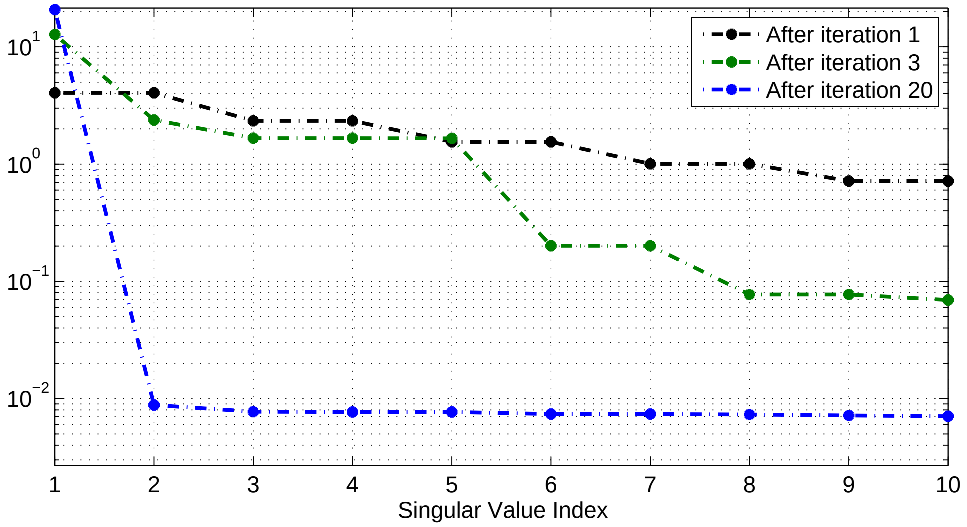

Figure 4.10: 10 largest singular values of $\mathbf{\Lambda}^i_{opt}$ at iteration $i = 1$ (black), $i = 3$ (green), $i = 20$ (blue).

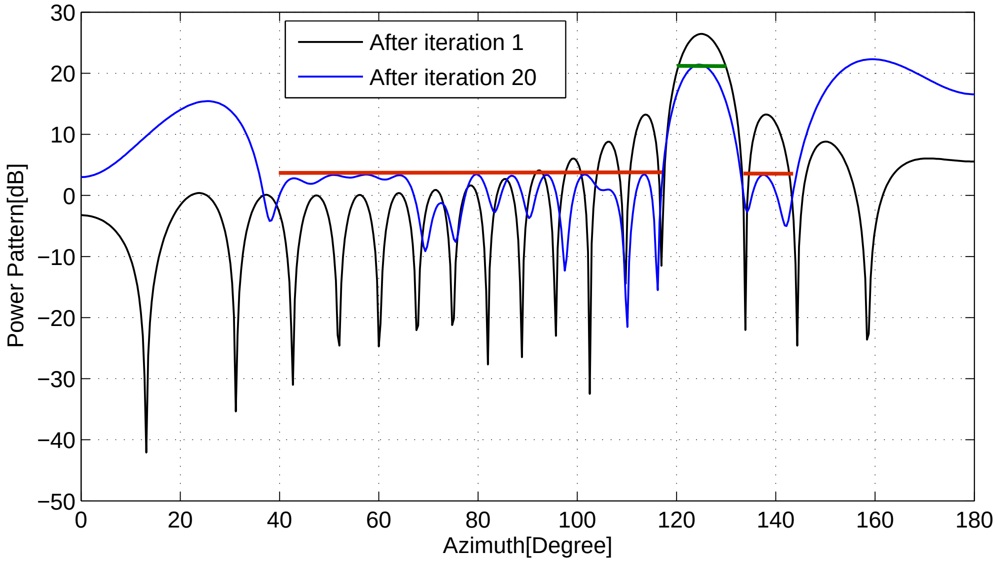

Figure 4.11: Elevation $\theta = 0^o$ cut of the power pattern for steering direction $(\bar{\theta} = 0^o, \bar{\phi} = 125^o)$ computed using the obtained weights after iteration $i = 1$ (black) and $i = 20$ (blue). Red lines indicate the sidelobe power level δ_s and green line indicates the main lobe power level δ.

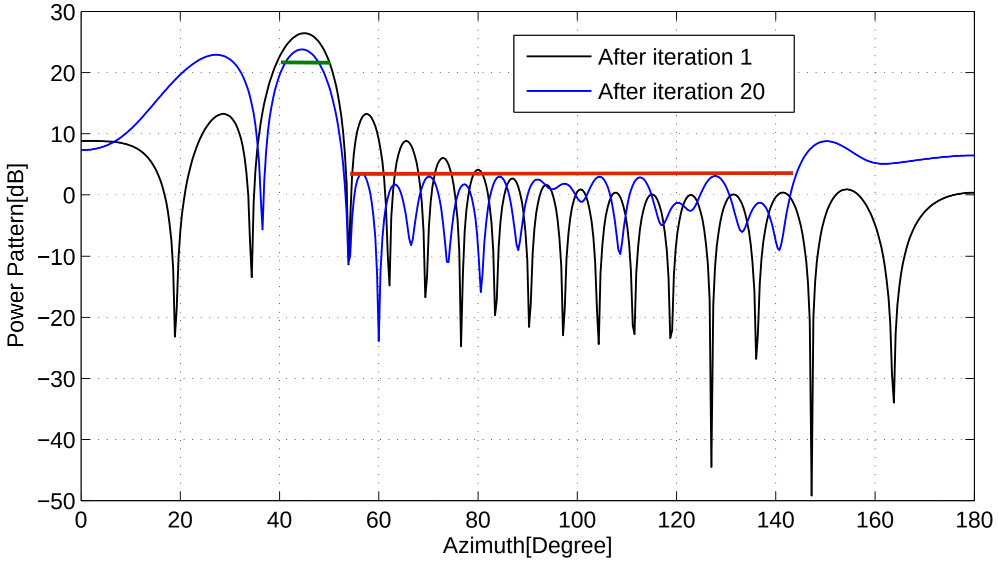

Figure 4.12: Elevation $\theta = 0^o$ cut of the power pattern for steering direction $(\bar{\theta} = 0^o, \bar{\phi} = 45^o)$ computed using the obtained weights after iteration $i = 1$ (black) and $i = 20$ (blue). Red line indicates the sidelobe power level δ_s and green line indicates the main lobe power level δ.

4.4 Phase-Only Sidelobe Suppression Problem

4.4.1 Problem Definition

In phase only sidelobe suppression applications, while maintaining the mainlobe power at a certain level, the total radiated power at desired directions is minimized by varying the element phases. Hence, the following optimization problem formalizes the phase-only sidelobe level suppression:

$$\begin{aligned} \min_{\alpha_n \in \mathbb{C}, n=1,..,N} \quad & \sum_{k=1}^{K} |B(\theta_{s_k}, \phi_{s_k})|^2 \\ \text{s.t.} \quad & B|(\bar{\theta}, \bar{\phi})|^2 = \delta, \\ & |\alpha_1| = |\alpha_2| = ... = |\alpha_N|, \end{aligned} \tag{4.19}$$

where $(\theta_{s_k}, \phi_{s_k}), k = 1, .., K$ are the sidelobe directions, at which the total radiated power is to be minimized; $(\bar{\theta}, \bar{\phi})$ is the steering direction, for which the required power level is restricted to be δ. Defining $\bar{\mathbf{v}} = [v_1(\bar{\theta}, \bar{\phi}), .., v_N(\bar{\theta}, \bar{\phi})]^T$, $\mathbf{v}_{s_k} = [v_1(\theta_{s_k}, \phi_{s_k}), .., v_N(\theta_{s_k}, \phi_{s_k})]^T$, and $\boldsymbol{\beta} = [\alpha_1, \alpha_2, .., \alpha_N]^H$, the optimization problem in (4.19) can be written in the following form:

$$\begin{aligned} \min_{\boldsymbol{\beta} \in \mathbb{C}^N, \gamma \in \mathbb{R}^+} \quad & \boldsymbol{\beta}^H \left(\sum_{k=1}^{K} \mathbf{v}_{s_k} \mathbf{v}_{s_k}^H \right) \boldsymbol{\beta} \\ \text{s.t.} \quad & \boldsymbol{\beta}^H \bar{\mathbf{v}} \bar{\mathbf{v}}^H \boldsymbol{\beta} = \delta, \\ & |\beta_n| = \gamma, \ n = 1, .., N. \end{aligned} \tag{4.20}$$

By further defining $\mathbf{V} = \bar{\mathbf{v}} \bar{\mathbf{v}}^H$, $\mathbf{V}_s = \sum_{k=1}^{K} \mathbf{v}_{s_k} \mathbf{v}_{s_k}^H$, its equivalent SDP formulation can be obtained as:

$$\begin{aligned} \min_{\boldsymbol{\Lambda} \in \mathbb{C}^{N \times N}, \gamma \in \mathbb{R}^+} \quad & Tr(\mathbf{V}_s \boldsymbol{\Lambda}) \\ \text{s.t.} \quad & Tr(\mathbf{V} \boldsymbol{\Lambda}) = \delta, \\ & \boldsymbol{\Lambda}_{i,i} = \gamma, \ i = 1, ..., N, \\ & \boldsymbol{\Lambda} \succeq 0, \\ & \text{rank}(\boldsymbol{\Lambda}) = 1. \end{aligned} \tag{4.21}$$

Although the quadratic constraints are linearised in this formulation, because of the rank constraint the constructed optimization problem in (4.21) is still non-convex. For moderate number of array elements, this problem could be solved by using the proposed method in Section 4.3. However, for large arrays, convex solvers fail to provide results in reasonable computation time. In the next section, an Alternating Direction Method of Multipliers (ADMM) based optimization approach will be proposed for efficient solution of large scale applications.

4.4.2 Proposed ADMM Based Solution

ADMM is an iterative algorithm, which integrates the decomposability property of dual ascent and the superior converge properties of method of multipliers [87]. Specifically, ADMM can be utilized for solving optimization problems in the following form:

$$\begin{aligned} &\min\ f(\mathbf{x}) + g(\mathbf{z}) \\ &\text{s.t. } : \mathbf{A}\mathbf{x} + \mathbf{B}\mathbf{z} = \mathbf{c}, \end{aligned} \tag{4.22}$$

where $\mathbf{x}{\in}\mathbb{R}^{n}$, $\mathbf{z}{\in}\mathbb{R}^{m}$, $\mathbf{A}{\in}\mathbb{R}^{p\times n}$, $\mathbf{B}{\in}\mathbb{R}^{p\times m}$, $\mathbf{c}{\in}\mathbb{R}^{p}$, f and g are convex functions of variables $\mathbf{x}$ and $\mathbf{z}$, respectively. At each ADMM iteration the following three updates are utilized:

$$\begin{aligned} \mathbf{x}^{k+1} &= \arg\min_{\mathbf{x}}\ L_{\rho}(\mathbf{x}, \mathbf{z}^{k}, \mathbf{y}^{k}), \\ \mathbf{z}^{k+1} &= \arg\min_{\mathbf{z}}\ L_{\rho}(\mathbf{x}^{k+1}, \mathbf{z}, \mathbf{y}^{k}), \\ \mathbf{y}^{k+1} &= \mathbf{y}^{k} + \rho(\mathbf{A}\mathbf{x}^{k+1} + \mathbf{B}\mathbf{z}^{k+1} - \mathbf{c}), \end{aligned} \tag{4.23}$$

where k is the iteration number and $L_{\rho}(\mathbf{x}, \mathbf{z}, \mathbf{y})$ is the augmented Lagrangian for (4.22) which is defined as:

$$L_{\rho}(\mathbf{x}, \mathbf{z}, \mathbf{y}) = f(\mathbf{x}) + g(\mathbf{z}) + \mathbf{y}^{T}(\mathbf{A}\mathbf{x} + \mathbf{B}\mathbf{z} - \mathbf{c}) + \frac{\rho}{2}\|\mathbf{A}\mathbf{x} + \mathbf{B}\mathbf{z} - \mathbf{c}\|^{2}. \tag{4.24}$$

Here, $\rho > 0$ is the parameter controlling deviation from the constraints of (4.22). By defining $\mathbf{u}{=}\mathbf{y}/\rho$, the x, z and y-update in (4.22) can be equivalently written as:

$$\begin{aligned}\mathbf{x}^{k+1} &= \arg\min_{\mathbf{x}} \; f(\mathbf{x}) + \frac{\rho}{2}\|\mathbf{A}\mathbf{x} + \mathbf{B}\mathbf{z}^k - \mathbf{c} + \mathbf{u}^k\|^2, \\ \mathbf{z}^{k+1} &= \arg\min_{\mathbf{z}} \; g(\mathbf{z}) + \frac{\rho}{2}\|\mathbf{A}\mathbf{x}^{k+1} + \mathbf{B}\mathbf{z} - \mathbf{c} + \mathbf{u}^k\|^2, \\ \mathbf{u}^{k+1} &= \mathbf{u}^k + \mathbf{A}\mathbf{x}^{k+1} + \mathbf{B}\mathbf{z}^{k+1} - \mathbf{c}. \end{aligned} \tag{4.25}$$

ADMM iterations are terminated when the following conditions are satisfied:

$$\|\mathbf{r}^k\|_2 \leq \epsilon^{pri}, \tag{4.26}$$

$$\|\mathbf{s}^k\|_2 \leq \epsilon^{dual}, \tag{4.27}$$

where primal error $\mathbf{r}^k$, dual error s^k and the corresponding termination thresholds ϵ^{pri} and ϵ^{dual} are given by:

$$\mathbf{r}^k = \mathbf{A}\mathbf{x}^k + \mathbf{B}\mathbf{z}^k - \mathbf{c}, \tag{4.28}$$

$$\mathbf{s}^k = \rho\mathbf{A}^T\mathbf{B}(\mathbf{z}^k - \mathbf{z}^{k-1}), \tag{4.29}$$

$$\epsilon^{pri} = \sqrt{p}\epsilon^{abs} + \epsilon^{rel}\max(\|\mathbf{A}\mathbf{x}^k\|, \|\mathbf{B}\mathbf{x}^k\|, \|\mathbf{c}\|), \tag{4.30}$$

$$\epsilon^{dual} = \sqrt{n}\epsilon^{abs} + \epsilon^{rel}\mathbf{A}^T\mathbf{y}^k. \tag{4.31}$$

The constants ϵ^{abs} and ϵ^{rel} are typically chosen as, 10^{-4} and 10^{-2}, respectively [87]. Derivations of the termination criteria in (4.26) and (4.27) are given in Appendix-C.

To solve (4.21) by using ADMM, x, z and u-update steps of ADMM iterations should be defined according to (4.21). The x-update step for (4.21) can be constructed as:

$$\begin{aligned}\mathbf{X}^{k+1} = \arg\min_{\mathbf{X}\in\mathbb{C}^{N\times N}\gamma\in\mathbb{R}^+} \; & Tr(\mathbf{V}_s\mathbf{X}) + \frac{\rho}{2}\|\mathbf{X} - \mathbf{Z}^k + \mathbf{U}^k\|_F^2 \\ \text{s.t. } & Tr(\mathbf{V}\mathbf{X}) = \delta, \\ & \mathbf{X}_{i,i} = \gamma, \; i = 1, .., N \end{aligned} \tag{4.32}$$

The optimization variable in (4.32) is the matrix $\mathbf{X}$ composed of complex numbers. The equivalent formulation to (4.32) with real optimization variables is:

$$\begin{aligned}\hat{\mathbf{X}}^{k+1} = \underset{\hat{\mathbf{X}}\in\mathbb{R}^{2N\times N},\gamma\in\mathbb{R}^{+}}{\arg\min} \quad & Tr(\hat{\mathbf{V}}_s\hat{\mathbf{X}}) + \frac{\rho}{2}\|\hat{\mathbf{X}} - \hat{\mathbf{Z}}^k + \hat{\mathbf{U}}^k\|_F^2 \\ \text{s.t.} \quad & Tr(\hat{\mathbf{V}}\hat{\mathbf{X}}) = \delta, \\ & \hat{\mathbf{X}}_{i,i} = \gamma,\ i = 1,..,N, \\ & \hat{\mathbf{X}}_{i+N,i} = 0,\ i = 1,..,N,\end{aligned} \tag{4.33}$$

where $\hat{\mathbf{X}} = [\Re\{\mathbf{X}\};\Im\{\mathbf{X}\}]$, $\hat{\mathbf{V}}_s = [\Re\{\mathbf{V}_s\}, -\Im\{\mathbf{V}_s\}]$, $\hat{\mathbf{V}} = [\Re\{\mathbf{V}\}, -\Im\{\mathbf{V}\}]$, $\hat{\mathbf{Z}}^k = [\Re\{\mathbf{Z}^k\};\Im\{\mathbf{Z}^k\}]$ and $\hat{\mathbf{U}}^k = [\Re\{\mathbf{U}^k\};\Im\{\mathbf{U}^k\}]$. To obtain a simpler form of (4.33), we introduce the following definitions:

$$\hat{\mathbf{x}}=\text{Vec}(\hat{\mathbf{X}}), \tag{4.34}$$

$$\hat{\mathbf{v}}_s=\text{Vec}(\hat{\mathbf{V}}_s^T), \tag{4.35}$$

$$\hat{\mathbf{v}}=\text{Vec}(\hat{\mathbf{V}}^T), \tag{4.36}$$

$$\hat{\mathbf{z}}^k=\text{Vec}(\hat{\mathbf{Z}}^k), \tag{4.37}$$

$$\hat{\mathbf{u}}^k=\text{Vec}(\hat{\mathbf{U}}^k), \tag{4.38}$$

where “Vec(.)” is the operator which converts matrices to vectors by column wise concatenation. By using the above vectorized forms, (4.33) can be equivalently written as:

$$\begin{aligned}\hat{\mathbf{x}}^{k+1} = \underset{\hat{\mathbf{x}}\in\mathbb{R}^{2N^2}}{\arg\min} \quad & \|\hat{\mathbf{x}} - \hat{\mathbf{z}}^k + \hat{\mathbf{u}}^k + \frac{1}{\rho}\hat{\mathbf{v}}_s\|_2^2 \\ \text{s.t.} \quad & \mathbf{A}\hat{\mathbf{x}} = \mathbf{a}.\end{aligned} \tag{4.39}$$

where $\mathbf{A}\in\mathbb{R}^{(2N)\times 2N^2}$ and $\mathbf{A}_{i,i+(i-1)2N}=1, i = 1,..,N-1$; $\mathbf{A}_{i,i+1+i2N}=-1, i = 1,..,N-1$; $\mathbf{A}_{i+N-1,i+(i-1)2N+N} = 1, i = 1,..,N$; $\mathbf{A}_{2N,i} = \hat{\mathbf{v}}_i, i = 1,..,2N^2$. All the other elements of $\mathbf{A}$ are zero. $\mathbf{a}\in\mathbb{R}^{2N}$ and $a_i = 0, i = 1,..,2N-1$; $a_{2N} = \delta$. The optimization problem in (4.39) has an analytic solution, which is the projection of $\mathbf{d}^k = \hat{\mathbf{z}}^k - \hat{\mathbf{u}}^k - \hat{\mathbf{v}}_s/\rho$ to the affine subspace $\mathbf{A}\mathbf{d}^k = \mathbf{a}$:

$$\hat{\mathbf{x}}^{k+1} = \mathbf{d}^k - \mathbf{A}^T(\mathbf{A}\mathbf{A}^T)^{-1}(\mathbf{A}\mathbf{d}^k - \mathbf{a}). \tag{4.40}$$

In ADMM iterations, the frequently used product $\mathbf{A}^T(\mathbf{A}\mathbf{A}^T)^{-1}$ can be precomputed and stored for a fast implementation. Once the optimal $\hat{\mathbf{x}}^{k+1}$ is computed by using (4.40), the complex matrices in (4.32), i.e., $\mathbf{X}\in\mathbb{C}^{N\times N}$, $\mathbf{Z}^k\in\mathbb{C}^{N\times N}$ and $\mathbf{U}^k\in\mathbb{C}^{N\times N}$, can be reconstructed.

In the z-update step, positive semidefiniteness and rank-1 constraints of (4.21) are handled by projecting $\mathbf{X}^{k+1}+\mathbf{U}^k$ on to the space of positive-semidefinite, rank-1 matrices. This projection can be computed by utilizing spectral factorization of $\mathbf{X}^{k+1}+\mathbf{U}^k$:

$$\begin{aligned} \mathbf{X}^{k+1}+\mathbf{U}^k &= \mathbf{Q}\boldsymbol{\Sigma}\mathbf{Q}^H, \\ \mathbf{Z}^{k+1} &= \sigma_1\mathbf{q}_1\mathbf{q}_1^H, \end{aligned} \tag{4.41}$$

where $\mathbf{Q}=[\mathbf{q}_1,\mathbf{q}_2,..,\mathbf{q}_N]$ and $\boldsymbol{\Sigma}=\text{diag}(\sigma_1,\sigma_2,..,\sigma_N)$ with σ_1 being the largest eigenvalue.

Finally, the u-update step is performed as

$$\mathbf{U}^{k+1}=\mathbf{U}^k+\mathbf{X}^{k+1}-\mathbf{Z}^{k+1}. \tag{4.42}$$

When the ADMM iterations are terminated, solution to (4.20) is obtained as:

$$\tilde{\boldsymbol{\beta}}=\sqrt{\sigma_1}\mathbf{u}_1. \tag{4.43}$$

where σ_1 is the largest singular value of $\mathbf{X}$ obtained in the final iteration of ADMM and $\mathbf{u}_1$ is the corresponding left singular vector. A final scaling and conjugation is applied to the elements of $\tilde{\boldsymbol{\beta}}$ to the find the estimates of the optimal phase values as:

$$\tilde{\alpha}_n=\tilde{\beta}_n^*/|\tilde{\beta}_n|,\ n=1,..,N. \tag{4.44}$$

In the next section experimental results demonstrating the performance of the proposed ADMM based method will be provided.

4.4.3 Experimental Results

In this section, for different array geometries and pattern constraints, ADMM based proposed technique is compared with the commonly used convex solver

CVX [85]. For the CVX solution, (4.21) is first relaxed to a convex program by removing its rank constraint, then it is solved by using CVX and estimates of the optimal phase values are obtained by applying rank-1 approximation and rescaling to the optimal solution as in (4.43) and (4.44). As a comparison metric, we define the average power in the set of directions at which suppression is desired:

$$\begin{aligned} P_{avr} &= \frac{1}{K}\sum_{k=1}^{K} |B(\theta_{s_k}, \phi_{s_k})|^2, \\ &= \frac{1}{K}\tilde{\boldsymbol{\alpha}}^T \mathbf{V}_s \tilde{\boldsymbol{\alpha}}^*, \end{aligned} \tag{4.45}$$

where $\tilde{\boldsymbol{\alpha}} = [\tilde{\alpha}_1, .., \tilde{\alpha}_N]^T$. In the rest of this section, the performance of the proposed approach will be illustrated over a set of simulations corresponding to practical applications.

In the first experiment, a uniform linear array of 50 elements is used. Array elements are placed along the x-axis. The operating frequency is set to 1GHz. Interelement spacing is chosen as half of wavelength. Steering direction of the beam is $\bar{\phi} = 90^o$ in azimuth and $\bar{\theta} = 90^o$ in elevation. The suppression sectors are defined as $\{\phi_{s_k}, |\phi_{s_k} \in [93^o, 103^o] \cup [120^o, 130^o] \cup [150^o, 160^o]\}$ in azimuth and $\theta_{s_k} = 90^o$ in elevation. These sectors are indicated with green dots in Fig.4.15. The mainlobe power is restricted to be half of the maximum achievable main lobe power, i.e., $\delta = N^2/2$. This level is also shown in Fig.4.15 with a black dot. As observed in Fig.4.13, the convergence rate of the ADMM iterations decrease as the iterations proceed for both primal and dual errors defined in (4.21) and (4.22), respectively. In Fig.(4.23), singular values of the optimal solution matrix for (4.21) provided by ADMM and CVX are shown. ADMM provided a rank-1 solution matrix. In Fig.4.15, the resulting antenna pattern for the phase estimates provided by ADMM(top-red) and CVX (bottom-red) are plotted. When array beam is only steered without any phase optimization, the resulting pattern is shown by blue on both top and bottom figures. P_{avr} values for ADMM and CVX results are -16.1dB and -5.6dB, respectively, showing that proposed ADMM based method provides 10dB additional suppression than CVX.

In the second experiment, a 10×3 planar array, whose elements are placed on the y-z plane is simulated. Operating frequency, interelement spacings and steering direction are chosen as they are in the first experiment. However, in the considered case here, this time the suppression direction is chosen as an angular region defined as $\{\phi_{s_k}, |\phi_{s_k} \in [17^o, 40^o]\}$ in azimuth and $\{\theta_{s_k}, |\theta_{s_k} \in [85^o, 95^o]\}$ in elevation. This region is indicated with a green rectangle on the top figure in Fig.4.18. The mainlobe power is again constrained to be $\delta = N^2/2$. As shown in Fig.4.16, ADMM iterations converge rapidly. In Fig.4.17, singular values of optimal solution matrix provided by ADMM (blue) and CVX (red) are shown. ADMM provides a rank-1 solution in the planar case as well. In Fig.4.18, the resulting antenna patterns are shown. In the top figure, a two dimensional plot of the original pattern without any phase optimization is provided. The resulting patterns for ADMM and CVX solutions are shown in the middle and the bottom figures, respectively. P_{avr} values calculated over the green rectangular region shown on the top plot for ADMM and CVX are -22.8dB and -7.9db, respectively. For this experiment, ADMM shows a 15dB improvement over CVX in terms of sidelobe suppression.

In the final experiment, the performance of ADMM for arrays having large number of elements is investigated. For a 200-element linear array, we repeated the first experiment with steering direction $\bar{\phi} = 45^o$ in azimuth and $\bar{\theta} = 90^o$ in elevation. The suppression directions are $\{\phi_{s_k}, |\phi_{s_k} \in [50^o, 55^o] \cup [80^o, 85^o] \cup [105^o, 110^o]\}$ in azimuth and $\theta_{s_k} = 90^o$ in elevation. The mainlobe power level is $\delta = N^2/2$. Note that, the number of variables in (4.21) for this problem is 40000. ADMM iterations are terminated after 200 iterations, which take about 85 seconds on an ordinary desktop computer. However, CVX can not provide a solution and returns a memory error on the same computer. Primal and dual error computed at each ADMM iteration is given in Fig.4.19, which indicates the convergence of the proposed method. Singular values of the solution matrix provided by ADMM is plotted in Fig.4.20. Even for this size of a sidelobe suppression problem, ADMM provides a rank-1 solution. In Fig.4.21, the resulting beam pattern is given. As observed, obtained phase values provides effective attenuation in the desired directions while satisfying the mainlobe power level.

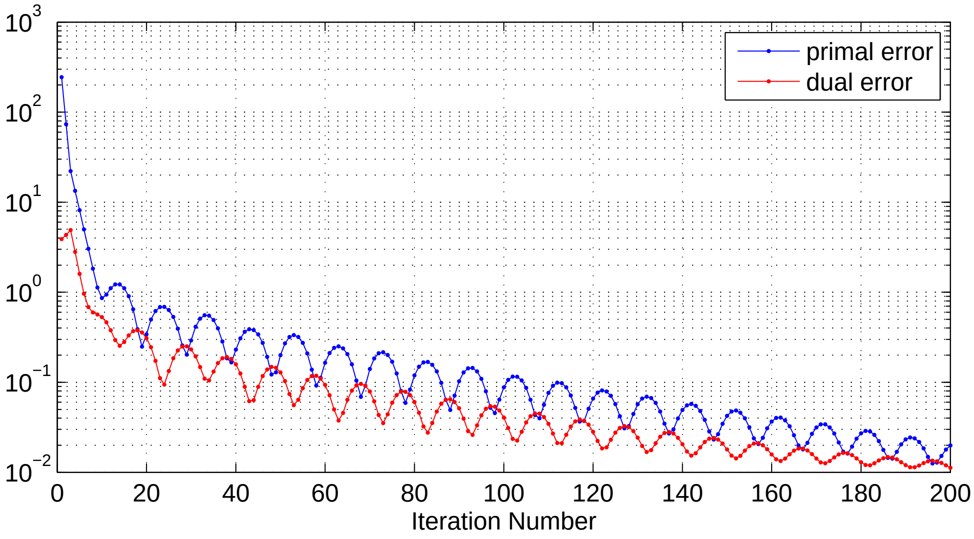

Figure 4.13: Convergence rate of ADMM iterations for the first experiment: Primal (blue) and dual (red) error defined in (4.21) and (4.22), respectively.

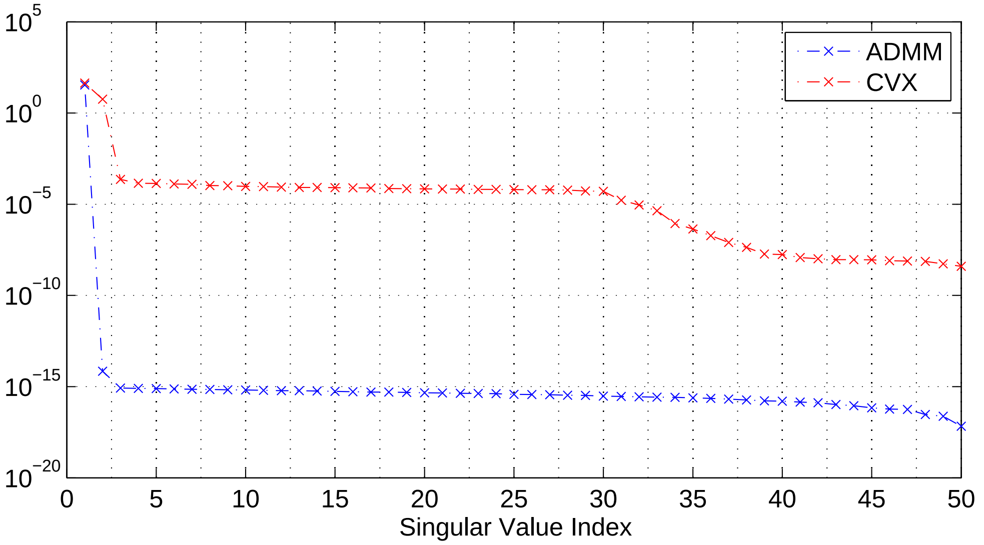

Figure 4.14: Singular values of the optimal solution matrix for (4.21) provided by ADMM (blue) and CVX (red) for the first experiment.

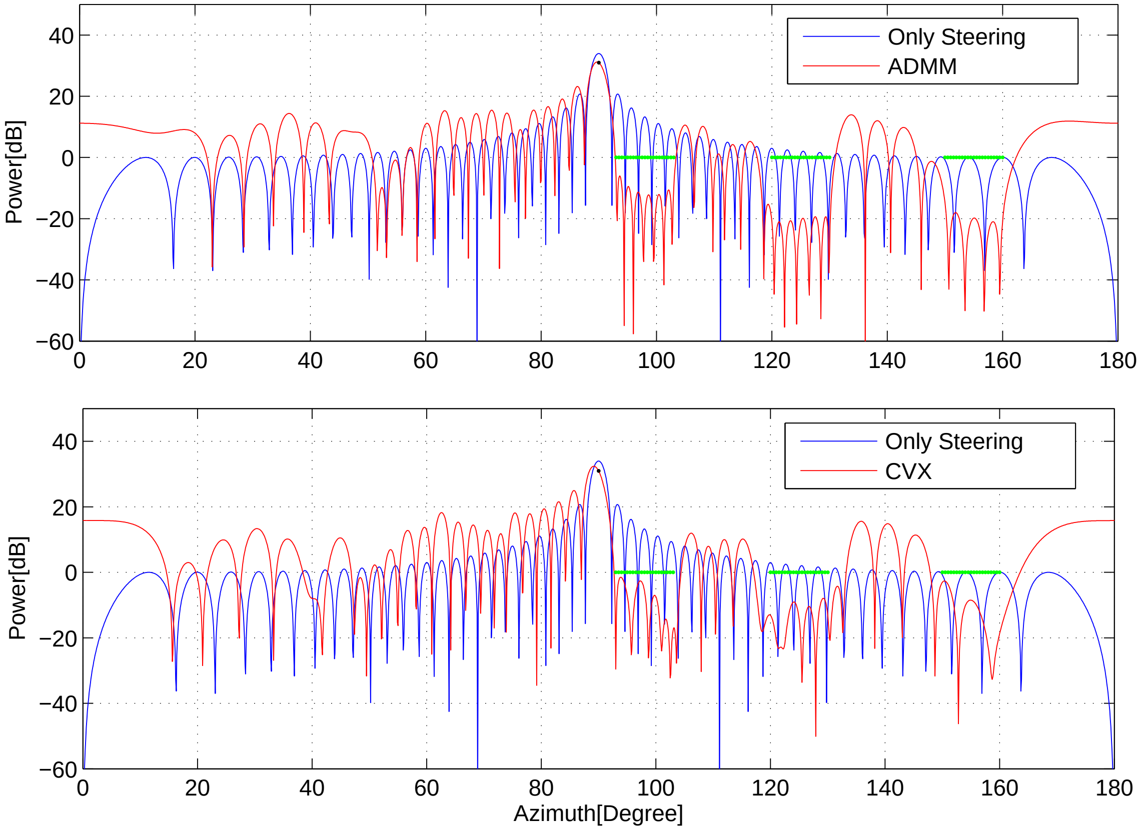

Figure 4.15: Resulting antenna patterns for ADMM (top-red) and CVX (bottom-red) results for the first experiment. When the array beam is only steered without any phase optimization, the resulting pattern is shown in blue on both top and bottom figures. Green dots indicate the suppression directions.

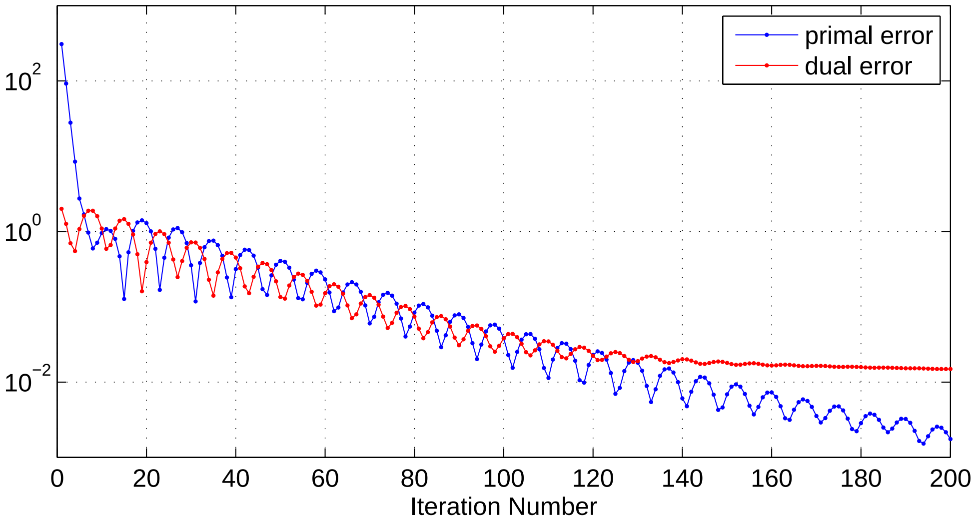

Figure 4.16: Convergence rate of ADMM iterations for the second experiment: Primal (blue) and dual (red) error defined in (4.21) and (4.22), respectively.

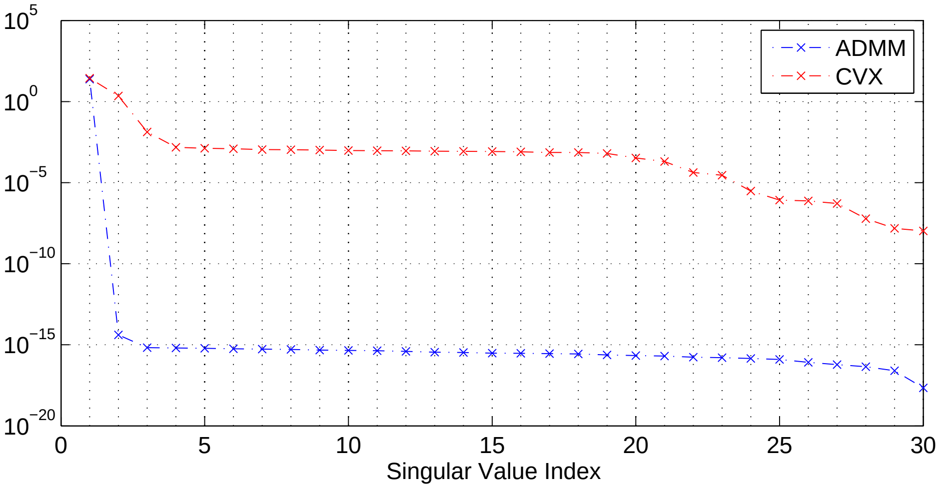

Figure 4.17: Singular values of the optimal solution matrix for (4.21) provided by ADMM (blue) and CVX (red) for the second experiment.

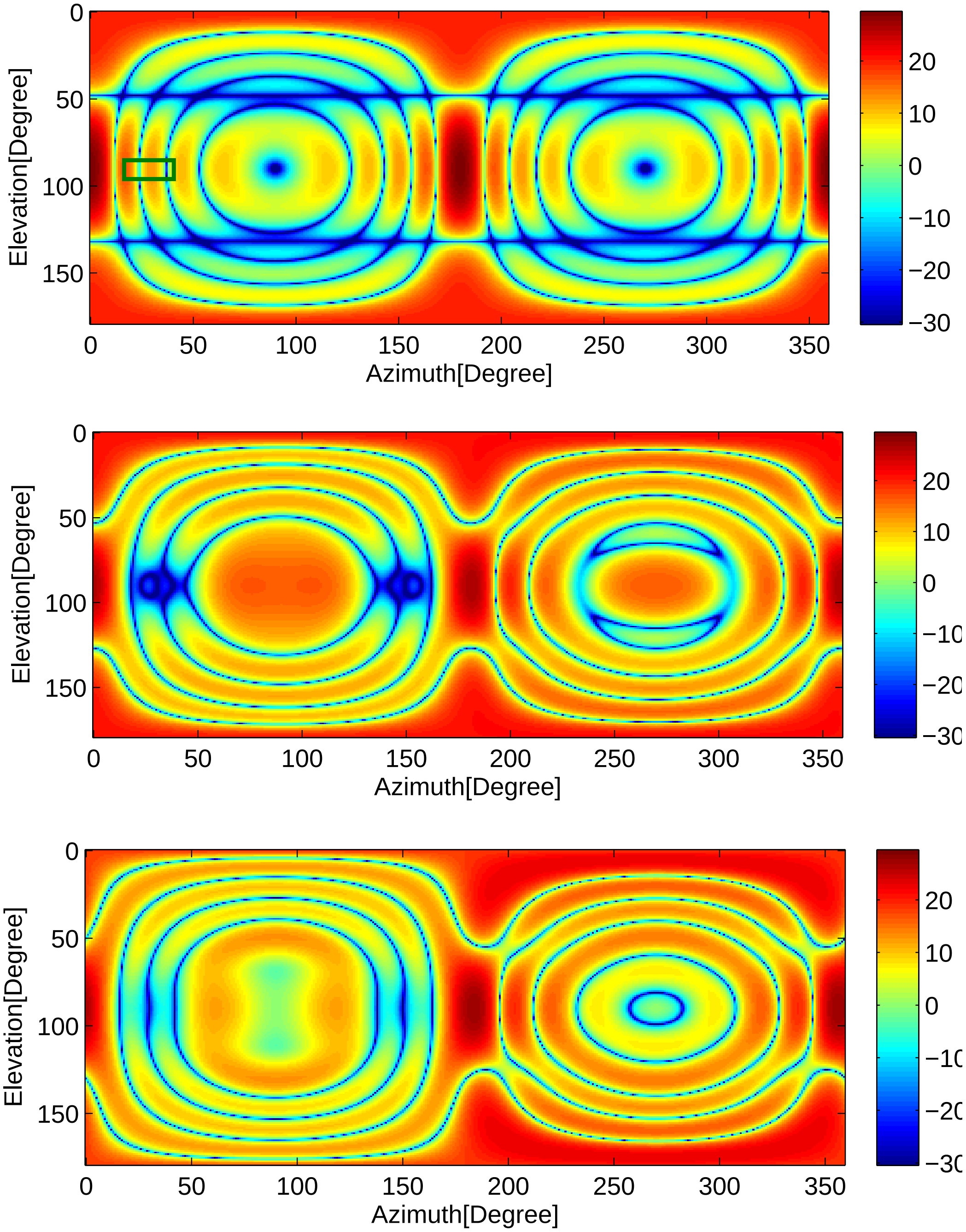

Figure 4.18: The resulting antenna pattern for the second experiment. On the top: original antenna pattern without any phase optimization (on the top). Green rectangle indicates the angular region for suppression. On the middle and on the bottom resulting patterns for the set of phase values provided by ADMM and CVX, respectively.

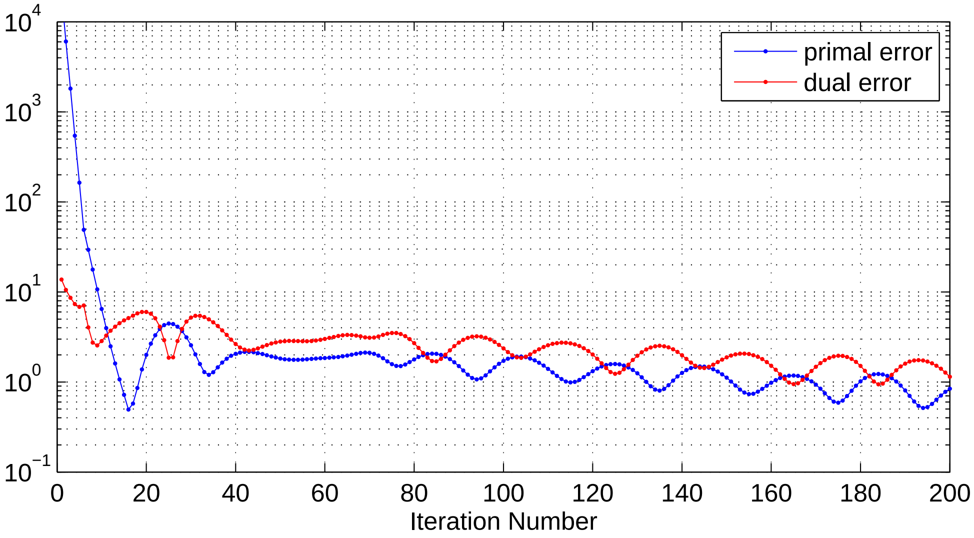

Figure 4.19: Convergence rate of ADMM iterations for the third experiment: Primal (blue) and dual (red) error defined in (4.21) and (4.22), respectively.

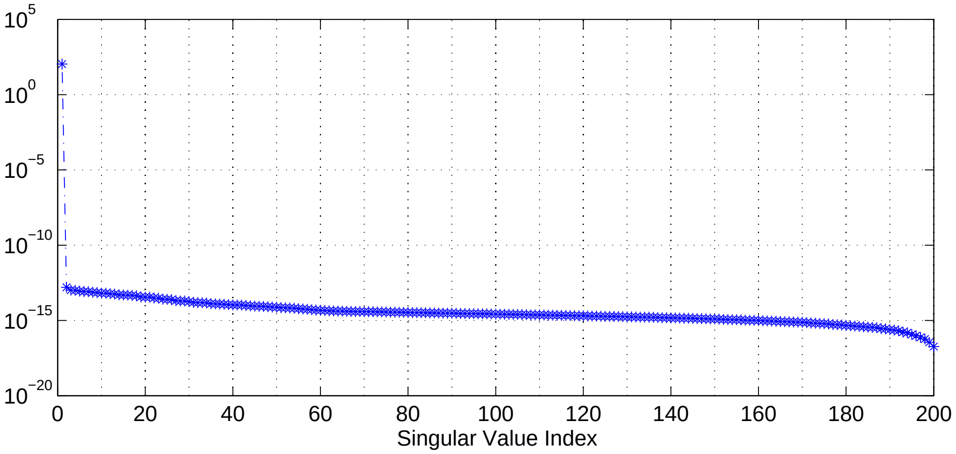

Figure 4.20: Singular values of the optimal solution matrix for (4.21) provided by ADMM.

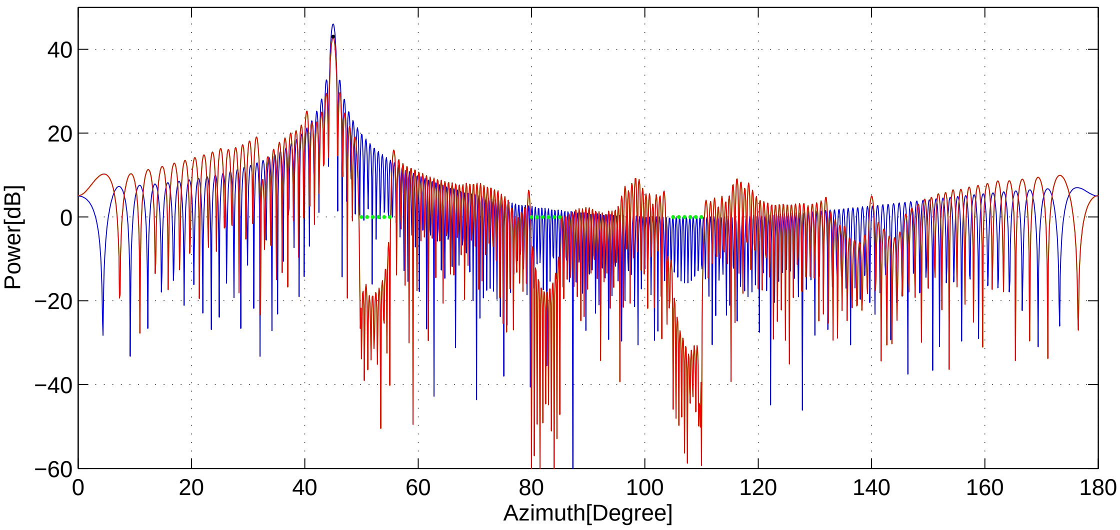

Figure 4.21: Resulting antenna pattern for ADMM (red) for the third experiment. When the array beam is only steered without any phase optimization, the resulting pattern is shown in blue. Green dots indicate the suppression directions. Black dot shows the mainlobe power level.

4.5 Conclusions for Chapter 4

For phase-only control of array antennas, two specific problems with proposed convex optimization based solutions are introduced. In the first problem, a set of phase values, for which the resulting beam pattern should satisfy the given sidelobe and mainlobe constraints are to be obtained. In the second problem, a set of phase values, which minimize the total radiation power of the resulting beam pattern at given directions, while keeping its mainlobe power at a certain level are to be estimated. Both problems are transformed to a convex SDP formulation. For the first problem, an iterative rank refinement algorithm is proposed. Conducted experiments show that proposed method provides a rank-1 solution for the constructed SDP. Hence, obtained phase estimates provides beam patterns with desired characteristics. For the second problem, an ADMM based method is proposed. We show that proposed method can provide rank-1 solutions to problems even for very large dimensions, which result in effective suppression in the desired directions.

Chapter 5

Conclusions and Future Work

In this thesis, to provide further flexibility and improved performance, novel approaches to three classical signal processing problems in optimization framework are developed. In the first part, a new signal analysis tool, which use Hermite-Gaussian (HG) functions, is developed. The key success behind the developed analysis technique is that HG functions provide optimal representations for signals, which are properly transformed in the time-frequency plane. Conducted experiments show that proposed method provides reliable identification and extraction of signal components even under severe noise cases.

In the second part, three alternative optimization based approaches are proposed for the design of orthogonal pulse shapes for ultra-wideband (UWB) communication systems with wideband antennas. We model each pulse shape as a linear combination of time shifted and scaled HG functions. Since the derivatives of HG functions can be represented as a linear combination of HGs, a simpler optimal correlating receiver structure is proposed.

In the final part, two novel methods are developed for phase-only control of array antenna patterns. First, antenna pattern design problem is formulated as a non-convex quadratically constrained quadratic problem (QCQP) is constructed. Then, by relaxing the constructed QCQP, a convex semidefinite problem (SDP) is obtained. For moderate size arrays, to converge iteratively to a rank-1 solution matrix for the SDP, we propose an iterative rank refinement algorithm, which forces sequentially obtained solution matrices towards a rank-1 matrix. Conducted experiments show that, proposed algorithm converges rapidly to a rank-1 solution of the constructed SDP. For large arrays, an alternating direction method of multipliers (ADMM) based method is developed. Since ADMM handles the SDP as a set of smaller subproblems, whose solutions are either analytically known or easy to numerically compute, optimal phase settings with desired beam characteristics for very large arrays can be obtained.

There are many other signal problems that can be reformulated as a SDP for improved performance. Applications such as SAR motion-compensation, phase retrieval in X-ray crystallography and signal design in ambiguity domain are among the many other applications that will benefit from such a reformulation. The main drove back of semidefinite programming is that the commonly encountered rank-1 constraint on the matrix of variables can not be handled and typically removed from the constraint set. Therefore, the obtained solutions to the SDP formulations fail to be rank-1. The iterative rank-refinement technique proposed in this thesis forces the obtained solutions towards a rank-1 matrix and hence, provides the desired solution using the efficient SDP solvers. As a future work, this novel rank-refinement approach will be used to obtain improved performances on the other problems mentioned above. For the ADMM formulation, to increase the converge rate, proximal based methods in [88] will be used.

Bibliography

[1] V. C. Chen and H. Ling, “Joint time-frequency analysis for radar signal and image processing,” *IEEE Signal Processing Magazine*, vol. 16, no. 2, pp. 81–93, 1999.

[2] M. Ning and D. Vray, “Bottom backscattering coefficient estimation from wideband chirp sonar echoes by chirp adapted time-frequency representation,” *Proceedings of the 1998 IEEE International Conference on Acoustics, Speech and Signal Processing*, vol. 4, pp. 2461–2464, 1998.

[3] R. G. Baraniuk, M. Coates, and P. Steeghs, “Hybrid linear/quadratic time-frequency attributes,” *IEEE Transactions on Signal Processing*, vol. 49, no. 4, pp. 760 – 766, 2001.

[4] B. Boashash and P. O’shea, “Time-frequency analysis applied to signaturing of underwater acoustic signals,” *Proceedings of the 1988 IEEE International Conference on Acoustics, Speech and Signal Processing*, vol. 5, pp. 2817–2820, 1998.

[5] O. Yilmaz and S. Rickard, “Blind separation of speech mixtures via time-frequency masking,” *IEEE Transactions on Signal Processing*, vol. 52, no. 7, pp. 1830–1847, 2004.

[6] A. K. Ozdemir, S. Karakas, E. D. Cakmak, D. I. Tufekci, and O. Arikan, “Time-frequency component analzser and its application to brain oscillatory activity,” *Journal of Neuroscience Methods*, vol. 145, no. 1-2, pp. 107–125, 2005.

[7] A. K. Ozdemir, *Time-frequency component analyzer.* PhD thesis, Bilkent University, Ankara, Turkey, September 2003.

[8] Y. K. Alp and O. Arikan, "Time-frequency analysis of signals using support adaptive hermite-gaussian expansions," *Digital Signal Processing*, vol. 22, no. 6, pp. 1010–1023, 2012.

[9] Y. K. Alp and O. Arikan, "Support adaptive hemite-gaussian expansions for analysis of multicomponent signals," *IEEE Signal Processing and Communucation Applications Conference (SIU)*, 2011.

[10] S. Karakas, E. D. Dincer, A. O. Ceylan, Y. K. Alp, and O. Arikan, "Time-frequency responses in adhd to neurocognitive tasks analyzed by time-frequency hermite-gaussian atomizer technique," *International Journal of Pyschophysiology.*

[11] N. Nebedev, *Special functions and their applications.* New York: Dover, 1972.

[12] S. Roy, J. R. Foerster, V. S. Somayazulu, and D. G. Leeper, "Ultra-wideband radio design: the promise of high speed short-range wireless connectivity," *Proceedings of the IEEE*, vol. 92, no. 2, pp. 295–311, 2004.

[13] P. Domenico and W. Hirt, "Ultra-wideband radio technology: potential and challenges ahead," *IEEE Communications Magazine*, vol. 41, no. 7, pp. 66–74, 2003.

[14] R. Qiu, H. Liu, and X. Shen, "Ultra-wideband for multiple access communications," *IEEE Communications Magazine*, vol. 43, no. 2, pp. 80–87, 2005.

[15] S. Gezici, Z. Tian, G. B. Giannakis, H. Kobayashi, A. F. Molisch, and H. V. Poor, "Localization via ultra-wideband radios: a look at positioning aspects for future sensor networks," *IEEE Signal Processing Magazine*, vol. 22, no. 4, pp. 70–84, 2005.

[16] "In the matter of revision of part 15 of the commissions rules regarding ultra-wideband transmission systems," *FCC Rep.*, pp. 2–48, 2002.

[17] B. Parr, B. Cho, K. Wallace, and Z. Ding, "A novel uwb pulse design algorithm," *IEEE Communications Letters*, vol. 7, no. 5, pp. 219–221, 2003.

[18] X. Wu, Z. Tian, T. Davidson, and G. Giannakis, "Optimal waveform design for uwb radios," *IEEE Transactions on Signal Processing*, vol. 54, no. 6, pp. 2009–2021, 2006.

[19] I. Dotlié and R. Kohno, "Design of the family of orthogonal and spectrally efficient uwb waveforms," *IEEE Journal of Selected Topics in Signal Processing*, vol. 1, no. 1, pp. 21–30, 2007.

[20] L. Michael, M. Ghavami, and R. Kohno, "Multiple pulse generator for ultra-wideband communications using hermite polynomial based orthogonal pulses," *IEEE Conference on Ultra Wideband Systems and Technologies*, pp. 47–51, 2002.

[21] J. da Silva and M. de Campos, "Spectrally efficient uwb pulse shaping with application in orthogonal psm," *IEEE Transactions on Communications*, vol. 55, no. 2, pp. 313–322, 2007.

[22] T. Montoya and G. Smith, "A study of pulse radiation from several broadband loaded monopoles," *IEEE Transactions on Antennas and Propagation*, vol. 44, no. 8, pp. 1172–1182, 1996.

[23] Y. Lo and S. Lee, *Antenna Handbook - Theory, Applications and Design.* Van Nostrand Reinhold, 1988.

[24] G. de Abreu, C. Mitchell, and R. Kohno, "On the design of orthogonal pulse shape modulation for uwb systems using hermite pulses," *Journal of Communications and Networks*, vol. 5, no. 4, p. 2003, 2003.

[25] S. Mishra, A. Rajesh, and P. K. Bora, "Performance of pulse shape modulation of uwb signals using composite hermite pulses," *National Conference on Communications*, pp. 1–5, 2012.

[26] Y. Alp, M. Dedeoglu, and O. Arikan, "Uwb orthogonal pulse shape set design by using hermite-gaussian functions," *IEEE Signal Processing and Communication Applications Conference (SIU).*

[27] Y. Alp, M. Dedeoglu, and O. Arikan, "Orthogonal pulse shape set design for uwb comminications," *IEEE Transactions on Signal Processing*, will be submitted.

[28] M. I. Skolnik, *Introduction to radar systems.* New York: McGraw-Hill, 1980.

[29] W. C. Knight, R. G. Pridham, and S. M. Kay, "Digital signal processing for sonar," *Proceedings of IEEE*, vol. 69, no. 11, pp. 1451–1507, 1981.

[30] J. H. Winters, "Smart antennas for wireless systems," *IEEE Personal Communications*, vol. 5, no. 1, pp. 23–27, 1998.

[31] M. Ryle, "The 5 kilometer radio telescope in cambridge," *Nauture*, vol. 293, pp. 435–4358, 1973.

[32] S. Haykin, *Array signal processing.* New Jersey: Prentice-Hall, 1985.

[33] H. Trees, *Optimum Array Processing: Part IV of Detection, Estimation, and Modulation Theory.* New York: John Wiley & Sons, 2002.

[34] C. Baird and G. Rassweiller, "Adaptive sidelobe nulling using digitally controlled phase-shifter," *IEEE Transactions on Antennas and Propagation*, vol. AP-24, no. 5, pp. 638–649, 1976.

[35] R. Giusto and R. Vincenti, "Phase-only optimization for generation of wide deterministic nulls in the radiation pattern of phased arrays," *IEEE Transactions on Antennas and Propagation*, vol. AP-31, no. 5, pp. 814–817, 1983.

[36] H. Steyskal, "Simple method for pattern nulling by phase perturbation," *IEEE Transactions on Antennas and Propagation*, vol. AP-31, no. 1, pp. 163–166, 1983.

[37] D. Boeringer and D. Werner, "Particle swarm optimization versus genetic algorithms for phased array synthesis," *IEEE Transactions on Antennas and Propagation*, vol. 52, no. 3, pp. 771–779, 2004.

[38] G. Mahanti and A. Chakrabarty, "Phase-only and amplitude-phase synthesis of dual-pattern linear antenna arrays using floating-point genetic algorithms," *Progress in Electromagnetic Research*, vol. 68, pp. 247–259, 2007.

[39] R. Haupt, "Phase-only adaptive nulling with a genetic algorithm," *IEEE Transactions on Antennas and Propagation*, vol. 45, no. 6, pp. 1009–1015, 1997.

[40] Y. Alp, O. Arikan, and A. Bayri, "Phase-only beam synthesis by iterative semidefinite relaxations with rank refinement," *European Signal Processing Conference (EUSIPCO)*, 2013.

[41] M. Dedeoglu, Y. K. Alp, and O. Arikan, "Both phase and magnitude constrained fir filter design by iterative convex relaxations with rank refinement," *IEEE Transactions on Signal Processing*, will be submitted.

[42] M. Dedeoglu, Y. K. Alp, and O. Arikan, "Fir filter design by iterative convex relaxations with rank refinement," *IEEE Signal Processing and Communications Applications Conference (SIU)*, 2014.

[43] Y. K. Alp, , and O. Arikan, "Admm based mainlobe power constrained, phase-only sidelobe suppression," *IEEE Signal Processing and Communication Applications Conference (SIU)*, 2014.

[44] Y. K. Alp, , and O. Arikan, "Mainlobe power constrained, phase-only sidelobe suppression by using alternating direction method of multipliers," *IEEE Transactions on Signal Processing*, will be submitted.

[45] J. B. Martens, "The hermite transform: A survey," *EURASIP Journal on Applied Signal Processing*, vol. 2006, pp. 1–20, 2006.

[46] W. Park, G. Leibon, D. N. Rockmore, and G. S.Chirikjian, "Accurate image rotation using hermite expansions," *IEEE Transactions on Image Processing*, vol. 18, no. 9, pp. 1988–2003, 2009.

[47] S. Stanković, I. Orović, and A.Krylov, "Video frames reconstruction based on time-frequency analysis and hermite projection method," *EURASIP Journal on Advances on Signal Processing*, vol. 18, no. 9, pp. 1988–2003, 2009.

[48] J. Silva and M. Campos, "Spectrally efficient uwb pulse shaping with application in orthogonal psm," *IEEE Transactions on Communications*, vol. 55, no. 2, pp. 313–322, 2007.

[49] A. Mahadevan, S. Acharya, D. B. Sheffer, and D. H. Mugler, “Ballistocardiogram artifact removal in eeg-fmri signals using discrete hermite transforms,” *IEEE Journal of Selected Topics in Signal Processing*, vol. 2, no. 6, pp. 839–853, 2008.

[50] W. Jiang and S. G. Kong, “Block-based neural networks for personalized ecg signal classification,” *IEEE Transactions on Neural Networks*, vol. 18, no. 6, pp. 1750–1761, 2007.

[51] I. Orović, S. Stanković, T. Chau, C. M. Steele, and E. Sejdić, “Time-frequency analysis and hermite projection method applied to swallowing accelerometry signals,” *EURASIP Journal on Advances on Signal Processing*, vol. 18, no. 19, pp. 1–7, 2010.

[52] M. M. Rao, T. K. Sarkar, T. Anjali, and R. S. Adve, “Simultaneous extrapolation in time and frequency domains using hermite expansions,” *IEEE Transactions on Antennas and Propagation*, vol. 47, no. 6, pp. 1108–1115, 1999.

[53] P. L. Carro and J. D. Mingo, “Ultrawide-band antenna distortion characterization using hermite-gauss signal subspaces,” *IEEE Antennas and Wireless Propagation Letters*, vol. 7, pp. 267–270, 2008.

[54] I. Orović, S. Stanković, T. Thayaparan, and L. Stanković, “Multiwindow s-method for instantaneous frequency estimation and its application in radar signal analysis,” *IET Signal Processing*, 2010.

[55] J. Xiao and P. Flandrin, “Multitaper time-frequency reassignment for non-stationary spectrum estimation and chirp enhancement,” *IEEE Transactions on Signal Processing*, 2007.

[56] M. Bayram and R. G. Baraniuk, *Multiple window time-varying spectrum estimation in Nonlinear and Nonstationary signal processing.* Cambridge: Cambrigde Univ. Press, 2000.

[57] F. Cakrak and P. J. Loughlin, “Multiple window time-varying spectral analysis,” *IEEE Transactions on Signal Processing*, 2001.

[58] L. Durak and O. Arikan, "Short-time fourier transform: two fundamental properties and an optimal implementation," *IEEE Transactions on Signal Processing*, vol. 51, no. 5, pp. 1231–1242, 2003.

[59] I. Daubechies, "The wavelet transform, time-frequency localization and signal analysis," *IEEE Transactions on Information Theory*, vol. 36, no. 5, pp. 961–1005, 1990.

[60] S. Mann and S. Haykin, "The chirplet transform: physical considerations," *IEEE Transactions on Signal Processing*, vol. 43, no. 11, pp. 2745–2761, 1990.

[61] P. Flandrin, "Maximum signal energy concentration in a time-frequency domain," *Proceedings of the 1988 IEEE International Conference on Acoustics, Speech and Signal Processing*, vol. 4, pp. 2176–2179, 1988.

[62] I. Daubechies, "Time-frequency localization operators: a geometric phase space approach," *IEEE Transactions on Information Theory*, vol. 34, no. 4, pp. 605–612, 1988.

[63] F. Hlawatsch, *Time-Frequency Analysis and Synthesis of Linear Signal Spaces.* Kluwer, 1998.

[64] L. R. Conte, R. Merletti, and G. V. Sandri, "Hermite expansions of compact support waveforms: applications to myoelectric signals," *IEEE Transactions on Biomedical Engineering*, vol. 41, no. 12, pp. 1147–1159, 1994.

[65] M. Abramowitz and I. Stegun, *Handbook of mathematical functions.* New York: Dover, 1965.

[66] G. Cincotti, F. Gori, and M. Santarsiero, "Generalized self fourier functions," *Journal of Physics A: Mathematical and General*, vol. 25, no. 20, pp. 1191–1194, 1992.

[67] H. Ozaktas, B. Barshan, D. Mendlovic, and L. Onural, "Convolution, filtering and multiplexing in fractional fourier domains and relations to chirp and wavelet transforms," *Journal of Optical Society of America A*, vol. 11, no. 2, pp. 547–559, 1994.

[68] L. Cohen, *Time-frequency analysis.* New Jersey: Prentice Hall PTR, 1995.

[69] T. F. Chan and L. A. Vese, "Active contours without edges," *IEEE Transactions on Image Processing*, vol. 10, no. 2, pp. 266–277, 2001.

[70] D. L. Donoho, "De-noising by soft thresholding," *IEEE Transactions on Information Theory*, vol. 41, no. 3, pp. 613–627, 1995.

[71] I. Daubechies, *Ten Lectures on Wavelets.* SIAM, 1992.

[72] D. L. Donoho and M. Johnstone, "Adapting to unknown smoothness via wavelet shrinkage," *Journal of American Statistical Association*, vol. 90, no. 432, pp. 1200–1224, 1995.

[73] L. Shafarenko, M. Petrou, and J. Kittler, "Automatic watershed segmentation of randomly textured color images," *IEEE Transactions on Image Processing*, vol. 6, no. 11, pp. 1530–1544, 1997.

[74] "Bat echolocation signal." http://dsp.rice.edu/software/bat-echolocation-chirp, 2009.

[75] R.Quiroga, "Obtaining single stimulus evoked potentials with wavelet denoising," *Physica D*, vol. 145, no. 3-4, pp. 278–292, 2000.

[76] R. Nobakht and M. Civanlar, "Optimal pulse shape design for digital communication systems by projections onto convex sets," *IEEE Transactions on Communications*, vol. 43, no. 12, pp. 2874–2877, 1995.

[77] S. Nordebo and Z. Zhanga, "A unified approach to digital filter design with time- and frequency-domain specifications," *IEEE Transactions on Circuits and Systems II: Analog and Digital Signal Processing*, vol. 46, no. 6, pp. 765–775, 1999.

[78] M. S. Lobo, L. Vandenberghe, S. Boyd, and H. Lebret, "Applications of second order cone programming," *Linear Algebra and its Applications*, vol. 284, no. 1-3, pp. 193–228, 1998.

[79] J. F. Sturm, “Using sedumi 1.02, a matlab toolbox for optimization over symmetric cones,” *Optimization Methods and Software*, vol. 11, no. 1-4, pp. 625–653, 1999.

[80] M. A. Branch and A. Grace, “Matlab optimization toolbox user’s guide,” *The MathWorks, Inc*, pp. 17–111.

[81] R. J. Mailloux, *Phased Array Antenna Handbook.* London: Artech House, 2005.

[82] O. Bucci and G. M. andG. Panariello, “Reconfigurable arrays by phase-only control,” *IEEE Transactions on Antennas and Propagation*, vol. 39, no. 7, pp. 919–925, 1991.

[83] S. Boyd and L. Vandenberghe, *Convex Optimization.* Cambridge: Cambridge University Press, 2004.

[84] Z. Luo, W. Ma, A. So, Y. Ye, and S. Zhang, “Semidefinite relaxation of quadratic optimization problems,” *Special Issue on Convex Opt. for SP*, pp. 1–14, 2010.

[85] I. CVX Research, “CVX: Matlab software for disciplined convex programming, version 2.0.” http://cvxr.com/cvx, 2012.

[86] R. Tutuncu, K. Toh, and M. Todd, “Solving semidefinite-quadratic-linear programs using sdpt3,” *Mathematical Programming, Series B,*, vol. 95, no. 2, pp. 189–217, 2003.

[87] S. Boyd, N. Parikh, E. Chu, B. Peleato, and J. Eckstein, “Distributed optimization and statistical learning via the alternating direction method of multipliers,” *Foundations and Trends in Machine Learning*, vol. 3, no. 1, pp. 1–122, 2011.

[88] S. S. J.Bolte and M. Teboulle, “Proximal alternating linearized minimization for nonconvex and nonsmooth problems,” *Mathematical Programming A*, 2013.

[89] L. Cohen, “Generalized phase-space distribution functions,” *Journal of Mathematical Physics*, vol. 7, no. 5, pp. 781–786, 1966.

[90] L. Cohen, "Time-frequency distributions-a review," *Proceedings of IEEE*, vol. 77, no. 7, pp. 941–981, 1989.

[91] H. Ozaktas, Z. Zalevsky, and M. Kutay, *The Fractional Fourier Transform with Applications in Optics and Signal Processings*. New York: Wiley, 2001.

Appendix A

A.1 Time-Frequency Distributions: A Short Review

The basic idea behind the time-frequency transforms is to device a distribution that represents the energy of a signal simultaneously in time and frequency. An infinite number of time-frequency distributions with different properties of a signal $s(t)$ can be generated from the following generalized formula [89]:

$$TF_s(t, f) = \int \int \int \kappa(\nu, \tau) s(u + \tau/2) s^*(u - \tau/2) e^{j2\pi(\nu u - \nu t - \tau f)} du d\nu d\tau, \quad \text{(A.1)}$$

where $\kappa(\nu, \tau)$ is the kernel of the distribution. Different choices of the kernel function leads to different time-frequency distributions [90]. By choosing $\kappa(\nu, \tau) = 1$, the Wigner-Ville distribution (WVD) is obtained:

$$WVD_s(t, f) = \int s(t + \tau/2) s^*(t - \tau/2) e^{-j2\pi\tau f} d\tau. \quad \text{(A.2)}$$

The spectrogram of $s(t)$ is obtained by choosing the kernel function as:

$$\kappa(\nu, \tau) = 2\pi \int h(u + \tau/2) h^*(u - \tau/2) e^{-j2\pi\nu u} du, \quad \text{(A.3)}$$

where $h(t)$ is a window function. Hence, the spectrogram of $s(t)$ is given by:

$$SPEC_s(t, f) = \left| \int s(\tau) h(\tau - t) e^{-j2\pi\tau f} du \right|^2. \quad \text{(A.4)}$$

Here, the integral term is also called as the short time Fourier transform (STFT) of the signal:

$$STFT_s(t,f) = \int s(\tau)h(\tau - t)e^{-j2\pi\tau f}du, \tag{A.5}$$

where the signal is first multiplied by a time-shifted window function and then its Fourier transform is computed. Interesting properties of WVD, STFT and other time-frequency distributions can found in [90].

A.2 Fractional Fourier Transform

The a^{th} order, $a \in \mathbb{R}, 0 < |a| < 2$, fractional Fourier Transform (FrFT) of a signal $s(t)$ is defined as [91]:

$$\mathcal{F}_s^a(t) = \int K_a(t,\tau)s(\tau)d\tau, \tag{A.6}$$

where the kernel of the transformation $K_a(t,\tau)$ is

$$K_a(t,\tau) = A_\phi e^{j\pi(t^2\cot\phi - 2t\tau\csc\phi + \tau^2\cot\phi)}, \tag{A.7}$$

$$A_\phi = \frac{e^{-j\pi \mathrm{sgn}(\sin\phi)/4 + j\phi/2}}{\sqrt{|\sin\phi|}}, \tag{A.8}$$

$$\phi = \frac{a\pi}{2}. \tag{A.9}$$

The 1^{th} order transform ($a = 1$) is the ordinary Fourier transform:

$$\mathcal{F}_a s(t) = S(f) = \int s(t)e^{-j2\pi ft}dt. \tag{A.10}$$

The 0^{th} order transform ($a = 0$) is the function itself. Other interesting properties of FrFT can be found in [91].

Appendix B

B.1 Derrivatives of Hermite-Gaussian Functions

In this appendix, it will be shown that successive derivatives of HG (Hermite-Gaussian) functions can be expressed as linear combinations of HG functions. The n^th HG function is given by

$$h_n(t) = \alpha_n H_n(c_1 t) e^{c_2 t^2} \ , \tag{B.1}$$

where $\alpha_n = \frac{2^{1/4}}{\sqrt{2^n n!}}$, $c1 = \sqrt{2\pi}$, $c_2 = -\pi$ and $H_n(t)$ is the n^{th} order Hermite polynomial. Hermite polynomials satisfy the following two relations [65]:

$$2tH_n(t) = H_{n+1}(t) + 2nH_{n-1}(t) \ , \tag{B.2}$$

$$\frac{d}{dt}H_n(t) = 2nH_{n-1}(t) \ . \tag{B.3}$$

The first derivative of $h_n(t)$ is given by:

$$\begin{aligned} \frac{d}{dt}h_n(t) &= 2\alpha_n c_2 e^{c_2 t^2} t H_n(c_1 t) + \alpha_n e^{c_2 t^2} \frac{d}{dt} H_n(c_1 t) \\ &= 2\alpha_n c_2 e^{c_2 t^2} t \left(\frac{H_{n+1}(c_1 t) + 2nH_{n-1}(c_1 t)}{2c_1 t} \right) + c_1 \alpha_n e^{c_2 t^2} 2nH_{n-1}(c_1 t) \\ &= \left(\frac{c_2}{c_1} + c_1 \right) 2n\alpha_n e^{c_2 t^2} H_{n-1}(c_1 t) + \frac{c_2}{c_1} \alpha_n e^{c_2 t^2} H_{n+1}(c_1 t) \end{aligned} \tag{B.4}$$

$$\begin{aligned}
&= \frac{c_2}{c_1}\frac{\alpha_n}{\alpha_{n+1}}h_{n+1}(t) + 2n\left(\frac{c_2}{c_1}+c_1\right)\frac{\alpha_n}{\alpha_{n-1}}h_{n-1}(t) \\
&= \frac{c_2}{c_1}\sqrt{2(n+1)}h_{n+1}(t) + \sqrt{2n}\left(\frac{c_2}{c_1}+c_1\right)h_{n-1}(t)\ .
\end{aligned} \tag{B.5}$$

By using (B.5), second derivative of $h_n(t)$ can be computed as:

$$\begin{aligned}
\frac{d^2}{dt^2}h_n(t) &= \frac{c_2}{c_1}\sqrt{2(n+1)}\frac{d}{dt}h_{n+1}(t) + \sqrt{2n}\left(\frac{c_2}{c_1}+c_1\right)\frac{d}{dt}h_{n-1}(t) \\
&= \frac{c_2}{c_1}\sqrt{2(n+1)}\left[\sqrt{2(n+1)}\left(\frac{c_2}{c_1}+c_1\right)h_n(t)\frac{c_2}{c_1}\sqrt{2(n+2)}h_{n+2}(t)\right] + \\
&\quad + \sqrt{2n}\left(\frac{c_2}{c_1}+c_1\right)\left[\sqrt{2(n-1)}\left(\frac{c_2}{c_1}+c_1\right)h_{n-2}(t) + \frac{c_2}{c_1}\sqrt{2n}h_n(t)\right] \\
&= 2\sqrt{n(n-1)}\left(\frac{c_2}{c_1}+c_1\right)^2 h_{n-2}(t) \\
&\quad + (4n+2)\frac{c_2}{c_1}\left(\frac{c_2}{c_1}+c_1\right)h_n(t) \\
&\quad + 2\sqrt{(n+1)(n+2)}\left(\frac{c_2}{c_1}\right)^2 h_{n+2}(t).
\end{aligned} \tag{B.6}$$

Successive derivatives of higher order can be computed similarly.

Appendix C

C.1 Termination Criteria of ADMM Iterations

In this appendix, termination criteria of ADMM iterations will be derived. Consider the following optimization problem:

$$\begin{aligned} \min\ & f(x) + g(z) \\ \text{s.t. } & Ax + Bz = c, \end{aligned} \tag{C.1}$$

where $x \in \mathbb{R}^n$, $z \in \mathbb{R}^m$, $A \in \mathbb{R}^{p\times n}$, $B \in \mathbb{R}^{p\times m}$ and $c \in \mathbb{R}^p$. f and g are convex and functions. The necessary and sufficient condition for (x^*, z^*, y^*) to be the optimal solution of (C.1) is primal feasibility

$$Ax^* + Bz^* - c = 0, \tag{C.2}$$

and dual feasibility

$$0 \in \partial f(x^*) + A^T y^*, \tag{C.3}$$

$$0 \in \partial g(z^*) + B^T y^*, \tag{C.4}$$

$$\tag{C.5}$$

where ∂ is the subdifferential operator.

In the z-update step of ADMM iterations, the following optimization problem is solved:

$$z^{k+1} = \arg\min_z\ L_\rho(x^{k+1}, z, y^k). \tag{C.6}$$

Hence, z^{k+1} satisfies the following condition:

$$\begin{aligned} 0 &\in \partial g(z^{k+1}) + B^T y^k + \rho B^T(Ax^{k+1} + Bz^{k+1} - c) \\ &= \partial g(z^{k+1}) + B^T(y^k + \rho(Ax^{k+1} + Bz^{k+1} - c)) \\ &= \partial g(z^{k+1}) + B^T y^{k+1}. \end{aligned} \tag{C.7}$$

This shows that, dual feasibility condition in (C.4) is automatically satisfied in the z-update step. As a result, optimality of the point (x^*, z^*, y^*) depends on (C.2) and (C.3).

In the x-update step of ADMM iterations, the following optimization problem is solved:

$$x^{k+1} = \arg\min_x \; L_\rho(x, z^k, y^k). \tag{C.8}$$

Hence, x^{k+1} satisfies the following condition:

$$\begin{aligned} 0 &\in \partial f(x^{k+1}) + A^T y^k + \rho A^T(Ax^{k+1} + Bz^k - c) \\ &= \partial f(x^{k+1}) + A^T(y^k + \rho(Ax^{k+1} + Bz^{k+1} - c) + \rho B(z^k - z^{k+1})) \\ &= \partial f(x^{k+1}) + A^T y^{k+1} + A^T B(z^k - z^{k+1}), \end{aligned} \tag{C.9}$$

which can be equivalently written as

$$A^T B(z^k - z^{k+1}) \in \partial f(x^{k+1}) + A^T y^{k+1}. \tag{C.10}$$

Here, $s^{k+1} = A^T B(z^k - z^{k+1})$ can be viewed as residual for the dual feasibility condition at iteration $k+1$. Similarly, $r^{k+1} = Ax^{k+1} - Bz^{k+1} - c$ can be defined as the residual for primal feasibility at iteration $k+1$.

A reasonable termination criteria for ADMM iterations is that both primal and dual residuals should be smaller than certain thresholds:

$$r^{k+1} \leq \epsilon^{pri}, \tag{C.11}$$

$$s^{k+1} \leq \epsilon^{dual}. \tag{C.12}$$

These thresholds can be chosen as[1]:

$$\epsilon^{pri} = \sqrt{p}\epsilon^{abs} + \epsilon^{rel} \max(\|Ax^{k+1}\|, \|Bx^{k+1}\|, \|c\|), \tag{C.13}$$

$$\epsilon^{dual} = \sqrt{n}\epsilon^{abs} + \epsilon^{rel}\|A^T y^{k+1}\|, \tag{C.14}$$

---

[1] All the norms are l_2 norms.

where $\epsilon^{abs} > 0$ is an absolute tolerance and $\epsilon^{rel} > 0$ is a relative tolerance, which can be typically chosen as $\epsilon^{abs} = 10^{-4}$ and $\epsilon^{rel} = 10^{-2}$, depending on the application [87].